UCAM

UNIVERSIDAD CATÓLICA DE MURCIA

ESCUELA INTERNACIONAL DE DOCTORADO

Programa de Doctorado en Ciencias de la Salud

Silicofosfatos cálcicos para ingeniería de tejidos.

Autor:
Patricia Ros Tárraga

Directores:
Dr. D. Luis Meseguer Olmo
Dr. D. Ángel Murciano Cases

Murcia, Mayo de 2018

UCAM

UNIVERSIDAD CATÓLICA DE MURCIA

ESCUELA INTERNACIONAL DE DOCTORADO

Programa de Doctorado en Ciencias de la Salud

Silicofosfatos cálcicos para ingeniería de tejidos.

Autor:
Patricia Ros Tárraga

Directores:
Dr. D. Luis Meseguer Olmo
Dr. D. Ángel Murciano Cases

Murcia, Mayo de 2018

UCAM

UNIVERSIDAD CATÓLICA
DE MURCIA

AUTORIZACIÓN DEL DIRECTOR DE LA TESIS PARA SU PRESENTACIÓN

El Dr. D. Luis Ramón Meseguer Olmo y el Dr. D. Ángel Murciano Cases como Directores[1] de la Tesis Doctoral titulada "Silicofosfatos cálcicos para ingeniería de tejidos" realizada por Dña. Patricia Ros Tárraga en el Departamento de Ciencias de la Salud, **autorizan su presentación a trámite** dado que reúne las condiciones necesarias para su defensa.

Lo que firmamos, para dar cumplimiento a los Reales Decretos 99/2011, 1393/2007, 56/2005 y 778/98, en Murcia a de Mayo de 2018.

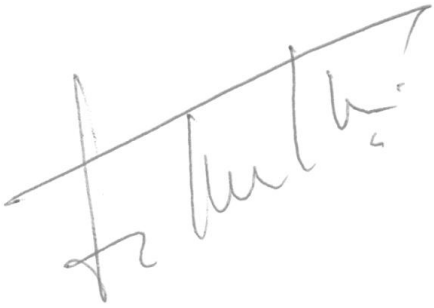

Fdo.: Luis Meseguer Olmo

Fdo.: Ángel Murciano Cases

[1] Si la Tesis está dirigida por más de un Director tienen que constar y firmar ambos.

ESTRUCTURA DE LA TESIS DOCTORAL

La presente Tesis Doctoral se presenta bajo el formato de compendio de publicaciones, el cual está incluido en la normativa vigente de la Escuela Internacional de Doctorado de la Universidad Católica San Antonio de Murcia. A continuación se citan las referencias completas de dichos artículos:

ARTÍCULO 1:

Patricia Ros-Tárraga, Angel Murciano, Patricia Mazon, Sergio A. Gehrke, Piedad N. De Aza. **New 3D stratified Si-Ca-P porous scaffolds obtained by sol-gel and polymer replica method: Microstructural, mineralogical and chemical characterization**. *Ceramics International*, 2017, 43(8), 6548-6553.

Fecha de publicación: 2017 DOI: 10.1016/j.ceramint.2017.02.081

FACTOR DE IMPACTO (JCR)	CATEGORÍA	CLASIFICACIÓN
2,986	Materials Science, Ceramics	2/26 (Q1)

ARTÍCULO 2:

Patricia Ros-Tárraga, Ángel Murciano, Patricia Mazón, Sergio A. Gehrke, Piedad N. De Aza. **In vitro behaviour of sol-gel interconnected porous scaffolds of doped wollastonite**. *Ceramics International*, 2017, 43(14), 11034-11038.

Fecha de publicación: 2017 DOI: 10.1016/j.ceramint.2017.05.146

FACTOR DE IMPACTO (JCR)	CATEGORÍA	CLASIFICACIÓN
2,986	Materials Science, Ceramics	2/26 (Q1)

ARTÍCULO 3:

Patricia Ros-Tárraga, Patricia Mazón, Luis Meseguer-Olmo, Piedad N. De Aza. **Revising the Subsystem Nurse's A-Phase-Silicocarnotite within the System $Ca_3(PO_4)_2$-Ca_2SiO_4**. *Materials*, 2016, 9(5), 322.

Fecha de publicación: 2016 DOI: 10.3390/ma9050322

FACTOR DE IMPACTO (JCR)	CATEGORÍA	CLASIFICACIÓN
2,654	Materials Science, Multidisciplinary	82/275 (Q2)

ARTÍCULO 4:

Patricia Ros-Tárraga, Rubén Rabadan-Ros, Angel Murciano, Luis Meseguer-Olmo, Piedad N. De Aza. **Assessment of Effects of Si-Ca-P Biphasic Ceramic on the Osteogenic Differentiation of a Population of Multipotent Adult Human Stem Cells**. *Materials*, 2016, 9(12), 969.

Fecha de publicación: 2016 DOI: 10.3390/ma9120969

FACTOR DE IMPACTO (JCR)	CATEGORÍA	CLASIFICACIÓN
2,654	Materials Science, Multidisciplinary	82/275 (Q2)

ARTÍCULO 5:

Patricia Ros-Tárraga, Patricia Mazón, Miguel A. Rodríguez, Luis Meseguer-Olmo, Piedad N. De Aza. **Novel Resorbable and Osteoconductive Calcium Silicophosphate Scaffold Induced Bone Formation**. *Materials*, 2016, 9(9), 785.

Fecha de publicación: 2016 DOI: 10.3390/ma9090785

FACTOR DE IMPACTO (JCR)	CATEGORÍA	CLASIFICACIÓN
2,654	Materials Science, Multidisciplinary	82/275 (Q2)

AGRADECIMIENTOS

En primer lugar, quiero agradecer a mi familia, en concreto a mis padres, Nani y Paco, y a mi hermana, Eloisa, todo el apoyo que me han dado desde el día en que nací. Siempre me han apoyado, en los momentos buenos y en los malos, en cada uno de los obstáculos que me he ido encontrando en la vida, que no han sido pocos. Siempre han estado ahí y eso me ha permitido llegar a ser la persona que soy hoy en día, gracias por todo. Además, quiero destacar la llegada del pequeño Óscar, que ha hecho que algunas de estas páginas se hayan escrito mientras mecía con el pie la hamaquita donde dormía.

Cuando comencé la carrera de Biotecnología no tenía pensado iniciar una carrera investigadora. Sin embargo, fueron apareciendo determinadas personas en mi vida que despertaron en mí una gran curiosidad por el mundo de la investigación. Estas personas fueron Piedad N. De Aza, Ángel Murciano, Patricia Mazón y, por supuesto, Tamara Muñoz Nortes. Piedad y Ángel, gracias por dirigir mis trabajos fin de Grado y de Máster, abrirme las puertas desde el primer día, confiar en mí, trabajar conmigo codo con codo y apoyarme siempre. Patricia, a pesar de no haber trabajado tan directamente contigo, siempre me has ayudado en todo lo que he necesitado, así que, muchas gracias.

Tamara, apareciste en mi vida hace algo más de 5 años, momento en el que te encontrabas realizando tu Tesis Doctoral. También tú me transmitiste tu curiosidad y amor por la investigación, y me apoyaste durante todo mi periodo universitario y durante los 3 años que ha durado mi periodo pre-doctoral. Quería darte las gracias por convertirte en mi compañera de vida y por apoyarme siempre de manera incondicional. Gracias por todo lo que hemos vivido y lo que nos queda por vivir.

Una vez finalizado mi Máster conocí a Luis Meseguer Olmo, quien sería mi director de Tesis Doctoral, junto con Ángel Murciano, codirigiendo mi Tesis, en la Universidad Católica San Antonio de Murcia. He de reconocer que nunca me imaginé que sería el tipo de persona que es. Siempre con una sonrisa, positivo y animándonos, tanto a mi compañero Rubén Rabadán Ros como a mí. Cada error que hemos cometido se convirtió en un nuevo reto a superar, siempre contando con su ayuda, su motivación y su ilusión por la investigación. Siempre nos ha hecho sentir como uno más, como compañeros de trabajo.

En cuanto a Rubén, qué peligro tienes cuando te juntas con Luis, pero cuántas risas nos hemos echado. Gracias por abrirme los brazos desde el primer día que pisé tierras murcianas, por ayudarme siempre y por compartir las penas en los errores que hemos cometido. Gracias a ti y a Luis he logrado superar (o al menos eso creo) mis mareos en quirófano y mis inseguridades en las cirugías.

Durante mi primer día de trabajo en IMIDA, además de conocer a Rubén, conocí a Ana Pagán, Salvador Cervantes y Abel Lozano. Todos ellos me han ayudado de manera incondicional desde el primer día, ofreciéndome su ayuda siempre que la he necesitado, e incluso en alguna ocasión, sus casas. Gracias por todas las risas, comidas y malos días que hemos compartido. Espero que queden muchos más por vivir. También quería darle las gracias a José Luis Cenis por abrirnos las puertas del IMIDA y acogernos.

Además, me gustaría agradecer la contribución realizada por muchos expertos de las diferentes materias que engloban la ingeniería de tejidos y Ciencia de Materiales, y a los integrantes del Vicerrectorado de Investigación de la UCAM, como María Josefa Yánez Gascón, más conocida como Pepa, jefa del servicio de microscopía de la UCAM; Antonia Bernabeu Esclapez, jefa de sección de cultivo de tejidos en el SACE; Beatriz Revilla Nuin, experta en Biología Molecular del Hospital Virgen de la Arrixaca; Carlos Martínez, experto en Histopatología Animal del Hospital virgen de la Arrixaca; y Mª Carmen Hernández Iniesta, administrativa de la UCAM. A todos ellos, gracias por vuestra paciencia y por compartir vuestro conocimiento conmigo. Pepa, a ti agradecerte las largas charlas y cafés que hemos compartido en cada una de mis visitas a tus aposentos y por enseñarme algo nuevo cada día.

Finalmente, me gustaría mencionar a las personas que fueron apareciendo en mi vida y se han quedado, mis amigos.

Marina García, nos conocemos desde hace relativamente poco tiempo, pero te has convertido en una persona muy importante para mí. Gracias por las charlas que hemos tenido, por los cafés compartidos y por llevarme a la Universidad de Murcia para realizar el curso de Cultivo de Células Animales aquel día, hace ya unos 4 años. Así comenzamos nuestra amistad, a la que aún le quedan, por lo menos, 4 años más.

Gyomar González, eres la alegría personificada. Siempre con una sonrisa en la cara y con una carcajada sonora. Gracias por esos momentos de risas, esas

partidas a las cartas o a cualquier juego de mesa y, sobre todo, por estrechar lazos con Tamara y conmigo el año que compartiste piso con ella. Ese hecho permitió que hayamos seguido conociéndonos y pasando buenos momentos.

Marina Sánchez, nos conocimos en la carrera y, teniendo en cuenta la primera impresión que tuve de ti, nunca pensé que llegaríamos a ser amigas. Somos totalmente diferentes, pero durante los 4 años de carrera hemos compartido horas y horas de sufrimiento y de diversión que, junto con Alex Pardines, hemos continuado teniendo. Nunca olvidaré vuestros "cambiando de tema" o "su base de datos de virus ha sido actualizada", que tantas risas produjeron.

Melissa Bello, también nos conocimos en la carrera, aunque nuestra relación se estrechó mucho más en el Máster. Gracias por mantener nuestra amistad, por sacar siempre algo de tiempo para hablar y tomar algo. Quería darte muchos ánimos para terminar tu Tesis Doctoral. Seguro que consigues obtener tu título de doctora muy pronto, y será bien merecido.

Por último, Cristian Ruiz. ¿Cuántos años nos conocemos? Este año hacen 23 añazos. Has sido la única persona que siempre he tenido a mi lado. Eres quien hace que todavía confíe en las personas, que me hace ver que todavía existen personas buenas, humildes, leales, honestas y todos aquellos adjetivos positivos que se le puedan dar a una persona. Siempre me has apoyado, siempre me has escuchado y siempre has estado ahí, incluso cuando empezamos a estar separados por 330 km de distancia. Que sepas que nunca olvidaré nuestros días en Charlie, en las Chimeneas, en la playa y en la piscina (con nuestra sensibilidad al cloro), nuestros viajes a Fallas ni tu reciclaje de leche para hacer crepes o nuestras partidas al Crash Team Racing y al Mario Bros. Has tenido la suerte de encontrarte con Víctor Ramos en tu aventura por Granada. Darte a ti también las gracias, Víctor, por cuidar siempre de Cristian y por esas visitas guiadas por Granada, que no las cambiaría por nada. Ambos sois lo mejor de allí, sin dudarlo. Seguid así y seguro que todo os irá genial.

"Todo el mundo ve lo que aparentas ser,
pocos experimentan lo que realmente eres"

Nicolás Maquiavelo (1469-1527)

"El secreto de la felicidad no es hacer
siempre lo que se quiere, sino querer siempre
lo que se hace"

León Tolstói (1828-1910)

ÍNDICE GENERAL

SIGLAS Y ABREVIATURAS

Las abreviaturas se muestran por orden alfabético

ah-MSCs	Células madre mesenquimales humanas adultas
AR-s	Disolución Alizarín Red
BIC	Hueso en contacto con un implante
C_2S – TCP	Silicato dicálcico – fosfato tricálcico
Ca^{2+}	Ión calcio
CaP	Fosfato cálcico
CDs	Marcadores de superficie específicos
CO_3^{2-}	Grupo carbonato
DRX	Difracción de Rayos X
EDX	Energía Dispersiva de Rayos X
F^-	Ión flúor
FA	Fosfatasa alcalina
H^+-ATPasa	Bomba de protones
IR-TF	Espectrometría Infrarroja por Transformada de Fourier
ISCT	Sociedad Internacional para la Terapia Celular
K^+	Ión potasio
MEB	Microscopio Electrónico de Barrido
Mg^{2+}	Ión magnesio
Na^+	Ión sodio
OH^-	Grupo hidroxilo
PO_4^{3-}	Grupo fosfato

psW	Pseudowollastonita
SFA	Suero Fisiológico Artificial
SiO_4^{4-}	Ión silicato
TEOS	Tetraetil ortosilicato – $Si(OC_2H_5)$
W-2M	Wollastonita-2M

ÍNDICE DE FIGURAS

ÍNDICE DE TABLAS

1. INTRODUCCIÓN

1. INTRODUCCIÓN

1.1. PROBLEMAS ÓSEOS DE NUESTRA SOCIEDAD

Nuestra sociedad ha experimentado un gran aumento en la esperanza de vida gracias a las mejoras sanitarias que se han desarrollado en los últimos años. Sin embargo, este aumento va ligado a un incremento en la incidencia de problemas relacionados con la degeneración músculo-esquelética, siendo los más frecuentes las fracturas, artropatías degenerativas, osteoporosis, tumores malignos y metástasis ósea. Además, también se ha producido un aumento en el número de traumatismos de elevada energía cinética, como son los ocasionados por los accidentes de tráfico, en los que se producen múltiples y complejas fracturas esqueléticas asociadas a pérdidas de tejido, suponiendo una pérdida significativa en la calidad de vida de las personas que las sufren. Como consecuencia de todo esto, son muchos los tratamientos médicos necesarios para reparar el tejido óseo, ocasionando elevados costes económicos. Sólo en los Estados Unidos, se llevan a cabo cerca de 1 millón de sustituciones de rodilla y cadera por implantes protésicos anualmente, con un coste asociado de unos 25 billones de dólares y, a nivel mundial, se realizan unos 2 millones de injertos óseos para tratar daños causados por cáncer y lesiones traumáticas (1-3).

Con objeto de poder desarrollar materiales adecuados para ser empleados en la regeneración del tejido óseo dañado, como consecuencia de este tipo de lesiones, es necesario comprender la fisiología del tejido óseo, considerando su estructura macroscópica, composición, organización celular y disposición de la matriz extracelular. A continuación se tratarán brevemente los conceptos anteriormente citados.

1.2. FISIOLOGÍA ÓSEA

El tejido óseo es un tejido conectivo especializado que se caracteriza por su rigidez, dureza, poder de regeneración y reparación. A pesar de su apariencia inerte, se trata de un tejido muy dinámico que se encuentra en continua

remodelación, adaptándose así a los cambios en las fuerzas biomecánicas necesarias para llevar a cabo sus funciones, permitiendo la sustitución del tejido óseo viejo y microdañado por tejido óseo neoformado. Durante este proceso, es muy importante que exista un equilibrio entre la resorción y la formación de tejido óseo. Un exceso de resorción genera una disminución en la densidad ósea, provocando enfermedades como la osteoporosis. En cambio, una excesiva formación de tejido, asociada a la reducción de la actividad osteoclástica, provoca un aumento de la densidad ósea, favoreciendo la aparición de un cuadro de osteopetrosis. Además, el tejido óseo tiene funciones tan importantes como la locomoción y soporte del cuerpo humano, protección de tejidos blandos y órganos vitales (cerebro, corazón, pulmón, etc.), almacenamiento de iones inorgánicos, como el calcio y fósforo, y factores de crecimiento, además de alojar la médula ósea hematopoyética.

1.2.1. El hueso: aspectos macro-microscópicos

El tejido óseo se compone de matriz ósea y células, pudiendo diferenciar dos tipos de hueso diferentes, en función de la densidad de su matriz: hueso cortical o compacto y hueso trabecular o esponjoso, que constituyen el 80 y 20% del tejido óseo, respectivamente (4-7) (figura 1).

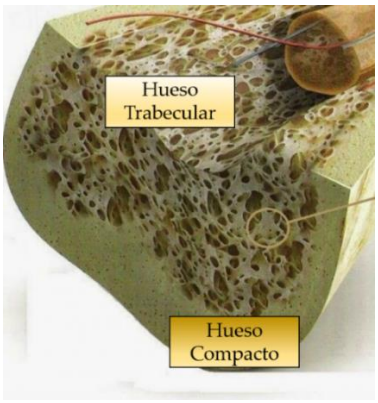

Figura 1. a) Representación macroscópica de una sección ósea, donde se puede observar la diferente morfología estructural entre el hueso trabecular y el hueso compacto (8, 9).

Hueso cortical o compacto: constituye la zona más externa de todos los huesos y se encarga de llevar a cabo funciones mecánicas y de protección. Presenta una densidad muy elevada debido a que el 90% de su superficie se encuentra

calcificada, y tiene una actividad metabólica bastante baja. Por este motivo, su tasa de recambio es mucho más lenta que la del hueso trabecular o esponjoso (un 2,5% anualmente, frente a un 25% del hueso trabecular). Su matriz calcificada se ordena en laminillas óseas, formando hueso compacto de tipo laminar u osteónico, según su disposición paralela o concéntrica alrededor de un canal, respectivamente. Estas estructuras laminares concéntricas, junto con los canales de Havers, por donde discurren nervios, vasos sanguíneos y vasos linfáticos, forman lo que se denominan osteonas, comunicadas entre sí por una serie de canales transversales denominados canales de Volkmann. Además, entre las laminillas podemos encontrar unas estructuras elípticas llamadas lagunas u osteoplastos, que se encuentran ocupadas por osteocitos (célula fundamental del tejido óseo), interconectados mediante una red tridimensional de conductos denominados canalículos, que facilitan la nutrición del osteocito.

Hueso trabecular o esponjoso: está constituido por trabéculas óseas dispuestas y ordenadas en la dirección de la carga que soportan. Se encuentra tanto en la zona interna de los huesos, como en la epífisis (extremos de los huesos largos), y su principal función es alojar la médula ósea hematopoyética (encargada de la producción de células sanguíneas), además de llevar a cabo funciones metabólicas. Esto es debido a su elevada porosidad interconectada, que permite el paso de vasos sanguíneos y elementos hematopoyéticos. Podemos diferenciar dos tipos de hueso trabecular, el no laminar y el laminar, en función de la disposición de las fibras de colágeno, ya sea de manera entrecruzada u ordenadas en laminillas óseas, respectivamente (9, 10).

En la figura 2 se pueden observar, a nivel microscópico, las diferencias estructurales del tejido óseo compacto (2a) y trabecular (2b).

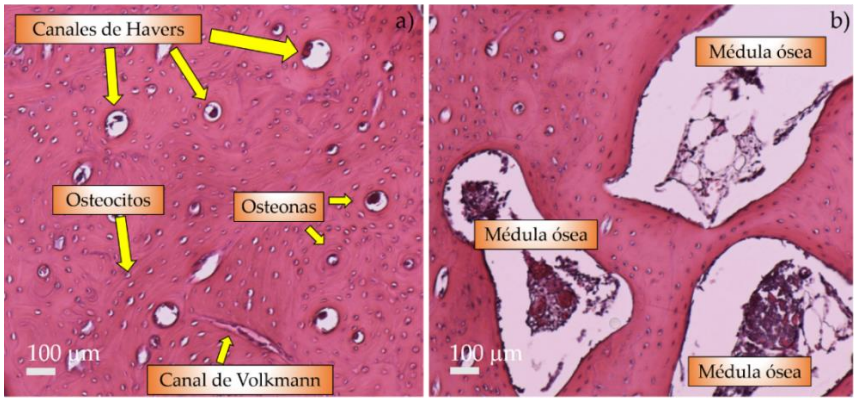

Figura 2. Detalles representativos de secciones óseas teñidas con hematoxilina – eosina de a) tejido óseo compacto donde se observan osteonas, canales de Havers y canales de Volkmann; b) tejido óseo trabecular, donde están presentes trabéculas óseas y médula ósea hematopoyética.

1.2.2. Fases de la matriz ósea extracelular

La matriz ósea está constituida por una fase inorgánica mayoritaria (70%), una fase orgánica (25%) y agua (5%).

Fase inorgánica: su componente mayoritario (99%) son los cristales de hidroxiapatito [$Ca_{10}(PO_4)_6(OH)_2$], formados por iones calcio (Ca^{2+}) y grupos fosfato (PO_4^{3-}). Además, presenta pequeñas cantidades de iones sodio (Na^+), magnesio (Mg^{2+}), potasio (K^+) y grupos carbonato (CO_3^{2-}). El calcio y los grupos fosfato, procedentes del plasma sanguíneo, se depositan sobre las fibras de colágeno del tejido óseo, formando un conglomerado organizado de proteínas y minerales (colágeno e hidroxiapatito, principalmente), alcanzando la integridad estructural necesaria para llevar a cabo las funciones mecánicas del esqueleto (4, 6).

Fase orgánica: constituida por colágeno (90-95%), sobre todo de tipo I, y proteínas estructurales no colagénicas que incluyen glucosaminoglucanos (como el ácido hialurónico y el condroitín sulfato), sialoproteínas, proteoglucanos y glucoproteínas, como la osteocalcina y la osteopontina (4, 6).

1.2.3. Estructura celular del hueso

En cuanto a la estructura celular del hueso y sus funciones, el tejido óseo está constituido por diferentes tipos de células: osteoblastos, células de revestimiento óseo y osteoclastos en las zonas más superficiales, además de osteocitos en el interior de la matriz ósea mineralizada.

Osteoblastos: son células cuboides diferenciadas que se encuentran presentes en un 4-6%, respecto al total de la población celular del tejido óseo, originadas a partir de células mesenquimales multipotentes. Se localizan sobre la superficie del hueso y se encargan tanto de la producción de la matriz ósea como de la osteoclastogénesis (inducción y maduración de osteoclastos). En la síntesis de matriz ósea, se pueden diferenciar 2 etapas: en la primera se deposita matriz orgánica no mineralizada (osteoide), y en la segunda se produce la mineralización de este osteoide. Durante la deposición de matriz orgánica, los osteoblastos secretan proteínas de colágeno, principalmente de tipo I, y proteínas no colagénicas, como las glucoproteínas y proteoglucanos, cuya carga negativa les permite inmovilizar iones Ca^{2+}. Una vez depositada la matriz orgánica, los osteoblastos liberan vesículas de matriz y una serie de enzimas que degradan los proteoglucanos, previamente unidos a las vesículas de matriz. Como consecuencia de esta degradación, se obtienen iones Ca^{2+} y otros productos con grupos PO_4^{3-}, permitiendo su entrada en el interior de las vesículas de matriz. Estos iones Ca^{2+} y grupos PO_4^{3-} son capaces de nuclear y comenzar la formación de cristales de hidroxiapatito en el interior de las vesículas, hasta que alcanzan una sobresaturación y son liberados al exterior, mineralizando la fase orgánica. Una vez formada la matriz ósea, los osteoblastos pueden seguir tres caminos diferentes: pueden entrar en apoptosis (muerte celular programada), convertirse en osteocitos al quedar atrapados por la matriz extracelular, o bien, permanecer como células de revestimiento óseo (5, 11).

Células de recubrimiento óseo: son células quiescentes cuya función no está del todo clara. Cubren las superficies óseas y se piensa que previenen la interacción directa entre los osteoclastos y la matriz ósea. Sin embargo, cabe destacar que su actividad de síntesis puede reactivarse en función del estado fisiológico del hueso, aumentando su tamaño y adoptando de nuevo la apariencia y función de los osteoblastos (5).

Osteocitos: son células óseas que provienen, como se ha indicado anteriormente, de los osteoblastos. Comprenden la mayor parte de la población celular total de los huesos y presentan una morfología dendrítica. Al final de cada ciclo de formación de tejido óseo, una subpoblación de osteoblastos se incorpora a la matriz ósea y entra en un estado de latencia, pasando a ser osteocitos. Estas células son las responsables del mantenimiento de una extensión limitada de matriz, puesto que son capaces de reabsorber y sintetizar sus componentes. Se sitúan en los osteoplastos de la matriz ósea, y se encuentran rodeados por una zona más próxima formada por matriz orgánica (osteoide) y una zona más alejada constituida por matriz ósea mineralizada. Los osteocitos son capaces de establecer conexiones tanto entre sí, como con el resto de células del tejido, además de con vasos sanguíneos, mediante la emisión de prolongaciones citoplasmáticas que pasan a través de los canalículos, permitiendo el paso y transferencia de iones inorgánicos, nutrientes y oxígeno. Esta conexión permite a los osteocitos actuar como mecanosensores, puesto que su red interconectada tiene la capacidad de detectar presiones y cargas mecánicas, ayudando al tejido óseo a adaptarse a las diferentes fuerzas mecánicas diarias. Por este motivo se piensa que los osteocitos se encargan de dirigir el remodelado óseo, regulando la actividad de los osteoblastos y osteoclastos (4-6).

En la figura 3a se puede observar la presencia de osteocitos ocupando sus lagunas, y un ribete de osteoblastos llevando a cabo la síntesis de nuevo tejido óseo.

Osteoclastos: son células óseas multinucleadas, encargadas de la resorción del tejido óseo, localizadas en depresiones someras llamadas lagunas de Howship (figura 3b). Provienen de células madre hematopoyéticas y son las células principales dentro del proceso de remodelación ósea, que se explicará a continuación (5, 6).

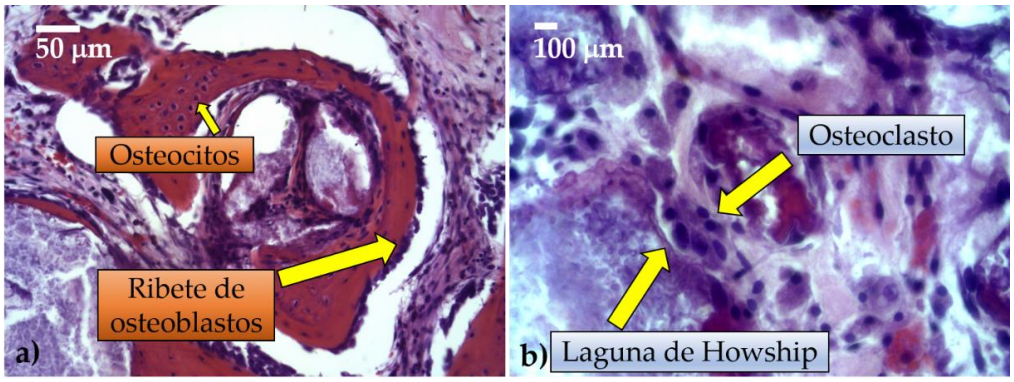

Figura 3. Imágenes de cortes histológicos teñidos con hematoxilina – eosina en los que se puede observar: a) tejido trabecular con presencia de osteocitos y de un ribete de osteoblastos sobre la superficie de una trabécula ósea; b) detalle donde se puede observar la presencia de osteoclastos situados en lagunas de Howship.

1.2.4. Remodelación ósea:

La principal función del remodelado óseo es sustituir el tejido óseo dañado y viejo por tejido nuevo. Este proceso permite mantener sus propiedades mecánicas, además de la homeostasis de los iones Ca^{2+} y grupos PO_4^{3-} (metabolismo mineral). Este proceso es llevado a cabo, principalmente, por los osteoclastos y los osteoblastos.

Cuando un osteoclasto se encuentra activo y resorbiendo hueso, se pueden diferenciar 4 dominios de membrana diferentes, tal y como se puede observar en la figura 4a:

1. **Zona basal**: aquella que se encarga de alojar la mayoría de orgánulos celulares.
2. **Borde en cepillo**: zona del osteoclasto que actúa de manera directa en la resorción del tejido óseo.
3. **Zona clara**: región del osteoclasto que se encuentra en la periferia del borde en cepillo. En ella se encuentran una gran cantidad de microfilamentos de actina que contribuyen a mantener el contacto entre la laguna de Howship y la periferia ósea.
4. **Zona vesicular**: donde se halla un gran número de vesículas que permiten la salida de enzimas lisosómicas hacia la zona de resorción por exocitosis, y

otras que introducen los productos obtenidos tras la degradación ósea por endocitosis. Se localiza entre la zona basal y el borde en cepillo.

En el borde en cepillo se encuentra una bomba de protones (H^+-ATPasa) que ayuda a acidificar la laguna de Howship o laguna de resorción, permitiendo que los cristales de hidroxiapatito se disuelvan y se produzca la desmineralización del hueso. A continuación, el osteoclasto activo lleva a cabo la liberación de enzimas lisosomales y metaloproteinasas, que se encargan de degradar la fase orgánica del hueso ya desmineralizado. Los productos de degradación son endocitados y conducidos hacia los capilares sanguíneos (5, 6). En la figura 4b se puede observar, de modo esquemático, la dirección que lleva el proceso de remodelado óseo: en primer lugar, los osteoclastos van resorbiendo el tejido óseo y, seguidamente, los osteoblastos se encargan de formar tejido nuevo.

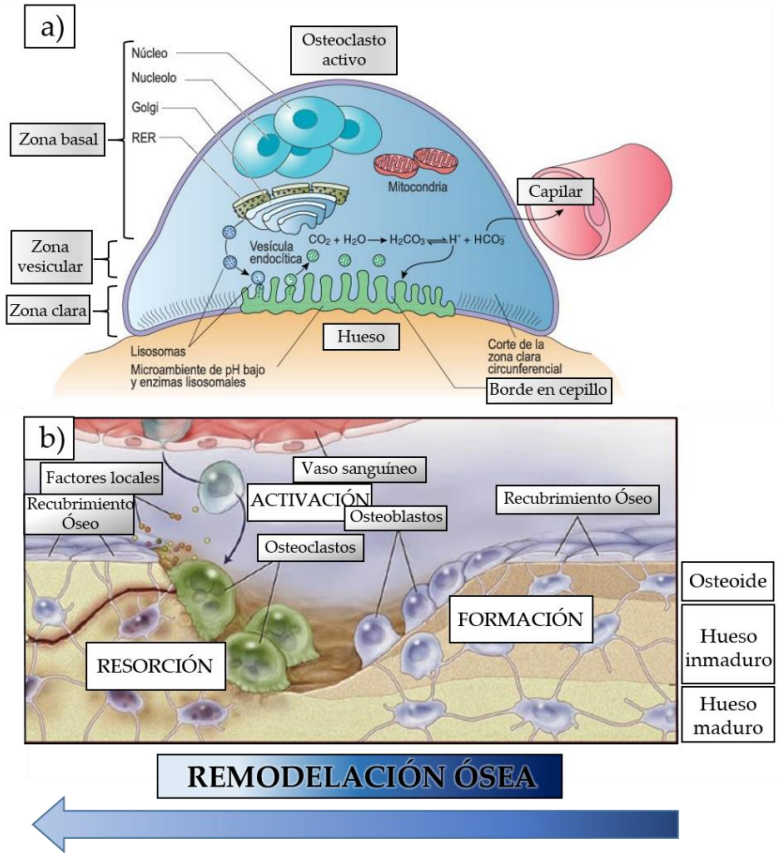

Figura 4. a) Diferentes dominios de membrana de un osteoclasto activo; b) proceso de remodelación ósea (12, 13).

1.3. CIENCIA DE MATERIALES

Una vez revisados los conceptos más relevantes de la fisiología y remodelación ósea, es necesario dirigir la atención hacia el campo encargado de desarrollar los materiales empleados en la regeneración del tejido dañado. En este sentido, se realizará una breve introducción de la Ciencia de Materiales, continuando con la descripción del injerto óseo autólogo, considerando actualmente como el material ideal o "gold standard", y terminando con la ingeniería de tejidos.

Los materiales, la evolución y la calidad de vida de una sociedad siempre han estado estrechamente relacionados, y es por ello que se hace referencia a las diferentes etapas históricas en función de sus materiales, como por ejemplo, la Edad de Piedra, Edad del Hierro y Edad del Bronce.

A pesar de que el ser humano siempre ha estado familiarizado con todo tipo de materiales (cerámicas, metales, polímeros, etc.), la Ciencia de Materiales como tal, no se reconoció como verdadera disciplina científica y académica hasta el año 1958, por lo que se trata de una rama relativamente nueva. Es una ciencia multidisciplinar y, para su descubrimiento y avance, fue necesaria una mayor comprensión de diferentes ciencias, como la física, la química y otras ciencias básicas del siglo XIX y primer tercio del siglo XX (14).

Dentro de la Ciencia de Materiales se encuentra la rama de los Biomateriales, que experimentó un gran desarrollo durante la 2ª Guerra Mundial, debido a la necesidad de utilizar materiales eficientes para sustituir o regenerar tejidos dañados. En este sentido, para ser definido como biomaterial, debían de ser compatibles con el cuerpo humano, pudiendo ser implantados en un organismo vivo con el fin de reparar, reemplazar o regenerar un tejido dañado sin que se produzca ningún tipo de rechazo por parte del mismo (15). Los primeros biomateriales utilizados para reparar zonas dañadas y fijar fracturas, fueron los metales (16), ya que se observó que los soldados con restos de metralla en su organismo vivían sin problemas.

A pesar de considerar la 2ª Guerra Mundial como el origen de los biomateriales, existen casos prehistóricos en los que se usaron. Los neandertales ya

elaboraban implantes dentales de madera, y se han encontrado cráneos Mayas con piezas de nácar (madreperla) como sustitutivo dental, datados de hace más de 4000 años. Por otra parte, a finales del siglo XVIII se empezaron a utilizar implantes dentales controlados, como las coronas de porcelana, y a finales del siglo XIX se utilizó un sulfato cálcico hemihidratado, o "Yeso de París", como material de relleno de defectos óseos (3, 17).

1.4. INJERTO ÓSEO AUTÓLOGO

Una vez conocido el proceso de remodelación ósea, es posible establecer las características y propiedades ideales que deben reunir aquellos materiales que serán utilizados en el campo de la regeneración del tejido óseo.

Hasta ahora, el biomaterial considerado como ideal o "gold standard" para la regeneración del tejido óseo es el injerto óseo esponjoso autólogo, debido a que cumple con los 3 requisitos indicados por la "*triada de la regeneración ósea"*: **osteoconducción, osteoinducción y osteogénesis**. El injerto óseo autólogo es osteoconductor, porque posee una estructura porosa abierta tridimensional, que permite la formación y distribución del tejido óseo neoformado por todo su interior; es osteoinductor porque los osteoblastos que posee son capaces de sintetizar factores de crecimiento sobre la matriz ósea, induciendo la diferenciación de las células madre mesenquimales multipotentes indiferenciadas a osteoblastos; finalmente, es osteogénico debido a que posee células osteo-precursoras, capaces de diferenciarse en osteoblastos. Además, al tratarse de tejido óseo, cumple con el resto de requerimientos biológicos y características estructurales necesarias para obtener una óptima regeneración del tejido: es biocompatible, bioactivo, biodegradable y tener propiedades mecánicas similares a las del hueso sano. Sin embargo, este tipo de injertos implican grandes restricciones, como pueden ser la necesidad de llevar a cabo 2 intervenciones, implicando dolor y hemorragias, además de la falta de disponibilidad de tejido, principalmente, en zonas donde se requiera regenerar una gran cantidad de tejido dañado.

Por lo tanto, las soluciones que se están aplicando hoy en día no son del todo eficaces y, además, suponen un gasto muy elevado para el Sistema Nacional de Salud. Por este motivo, ha sido necesario el desarrollo de una nueva ciencia denominada ingeniería de tejidos (3, 18, 19).

1.5. INGENIERÍA DE TEJIDOS

La ingeniería de tejidos ha surgido en las últimas décadas como una disciplina con potencial aplicación en la reconstitución ósea, con el objetivo de superar las complicaciones asociadas a los procedimientos tradicionales que hacen uso de injertos óseos. Recientemente, su papel se ha vuelto más estratégico debido a una demanda cada vez mayor de trasplantes, prótesis o regeneración del tejido óseo.

Según la ingeniería de tejidos, un biomaterial puede ser definido como una matriz tridimensional temporal que proporciona un ambiente específico y una estructura adecuada para el crecimiento y desarrollo del hueso. Estas matrices pueden utilizarse como sistemas acelulares, que permiten la colonización celular una vez implantadas, además de poder usarse como vehículos para células y/o factores de crecimiento (figura 5). Esta última combinación promueve la formación de hueso *in vivo* favoreciendo la diferenciación de las células osteoprecursoras mediante la liberación de determinadas sustancias solubles. Las células más utilizadas son las células mesenquimales multipotentes humanas adultas (adult human mesenchymal stem cells, ah-MSCs), que se describirán a continuación (1).

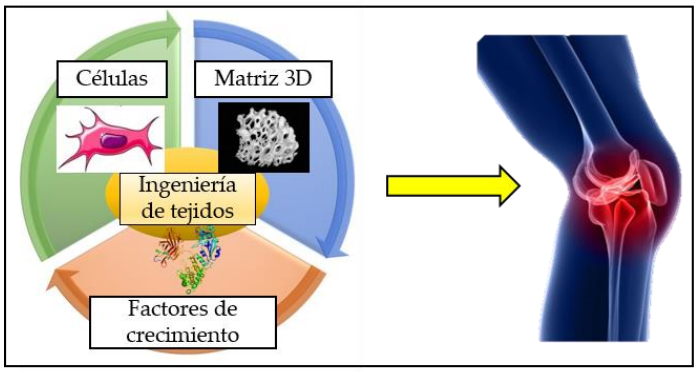

Figura 5. Esquema representativo de los elementos que conforman la ingeniería de tejidos: una matriz tridimensional, células y factores de crecimiento, que serán implantados en la zona dañada para permitir y acelerar la regeneración de la zona dañada.

1.5.1. Células madre mesenquimales multipotentes

Las células madre mesenquimales multipotentes son un tipo de células indiferenciadas capaces de diferenciarse en otros tipos celulares del tejido conectivo. Este potencial de diferenciación permite utilizarlas, asociadas a biomateriales, dentro del ámbito de la medicina regenerativa y la ingeniería tisular, con el fin de reparar y regenerar tejidos dañados.

Según la Sociedad Internacional de Terapia Celular (International Society for Cellular Therapy – ISCT), los tres requisitos mínimos que se deben cumplir para que una población de células procedentes de cualquier tejido adulto sea tipificada como células madre mesenquimales multipotentes (figura 6) son:

1. Ser adherentes al plástico, donde serán capaces de crecer bajo unas condiciones estándar de cultivo.

2. Mostrar ~ 90% de expresión de los marcadores específicos de superficie de células madre mesenquimales CD105, CD73 y CD90, y menos de un 5% de otros marcadores específicos hematopoyéticos, como CD45 y CD34.

3. Las células tienen que ser capaces de diferenciarse *in vitro* en osteoblastos, condroblastos y adipocitos en condiciones de diferenciación específica para cada linaje celular.

Este tipo de células son muy interesantes desde el punto de vista de la ingeniería de tejidos, principalmente, porque presentan una inmunogenicidad baja o nula, y son capaces de secretar citoquinas que les permiten modificar el microambiente inmune del huésped, permitiendo modular su respuesta inmunitaria y favoreciendo la reparación del tejido dañado (inmunomoduladoras) (20, 21).

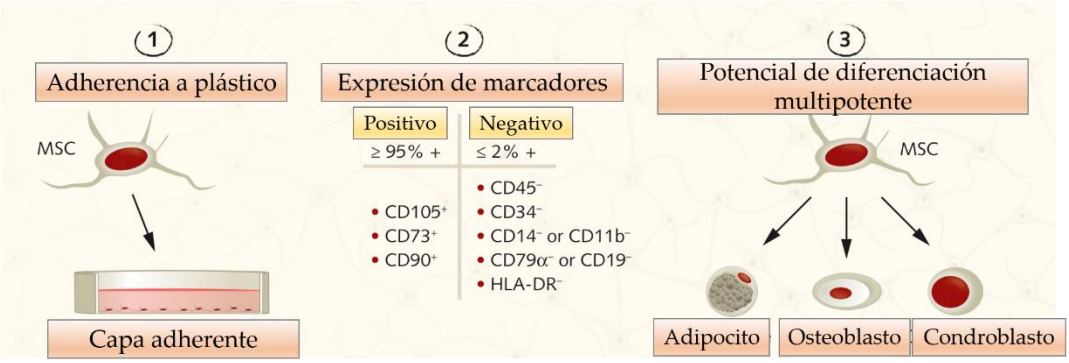

Figura 6. Requisitos mínimos que deben cumplir las células para que sean consideradas como células madre mesenquimales multipotentes adultas (22).

1.5.2. Evolución de los biomateriales

Desde su origen en la 2ª Guerra Mundial, los biomateriales han ido evolucionando, siendo:

- De 1ª generación o biomateriales inertes, que surgieron a partir del año 1950. Son materiales biocompatibles que generan tejido fibroso a su alrededor. El organismo reconoce el material como un cuerpo extraño y lo encapsula. Dentro de este tipo de biomateriales, se encuentran los metales, las aleaciones y las cerámicas inertes, como la alúmina y la circona.

- De 2ª generación o biomateriales bioactivos o biodegradables, que surgieron a partir del año 1970. Son materiales biocompatibles que, o bien son capaces de generar una capa de hidroxiapatito a su alrededor, permitiendo una unión química entre el implante y el tejido vivo (bioactivos), o bien son reemplazados por el tejido óseo circundante (biodegradables). La hidroxiapatita, diferentes biovidrios y algunos polímeros son ejemplos de este tipo de biomateriales.

- De 3ª generación o biomateriales bioactivos y biodegradables, que surgieron a partir del año 1990. Son materiales capaces de generar una capa de hidroxiapatito a su alrededor y, además, se van reabsorbiendo,

> permitiendo una unión química inicial entre el implante y el tejido óseo, seguida de una sustitución completa del material implantado por tejido sano. Finalmente, se tendría el tejido óseo totalmente regenerado y no quedaría rastro del implante. El β-fosfato tricálcico y diversos compuestos orgánico/inorgánicos se encuentran dentro de este grupo de materiales (23).

Hoy en día, la mayoría de prótesis óseas se obtienen a partir de metales y aleaciones, es decir, biomateriales de primera generación o bioinertes. Sin embargo, este tipo de biomateriales tienen una serie de inconvenientes, como la posible liberación de iones metálicos tóxicos para el organismo, su baja biodegradabilidad y, por lo tanto, su baja o nula reabsorción, y la no-correspondencia entre la rigidez del tejido óseo natural con el implante. La diferencia entre la rigidez del material y la del tejido óseo, provoca que las cargas que soporta el hueso y el implante sean diferentes, siendo mayor la soportada por el material, provocando la resorción ósea en zonas próximas al implante. Este proceso se denomina osteopenia asociada al uso de implantes protésicos o "stress shielding".

Para permitir una mejor unión entre el implante metálico y el tejido circundante, se han recubierto con biocerámicas, como el hidroxiapatito, material profundamente estudiado y que posee una buena bioactividad (19, 24-26). Sin embargo, continúan existiendo los problemas de la liberación de iones metálicos tóxicos y el "stress shielding".

1.5.3. Biocerámicas

Por el motivo anteriormente citado, es necesario estudiar otros biomateriales, como las biocerámicas. Éstas se definen como "materiales cerámicos diseñados para lograr un comportamiento fisiológico específico al ser usados en la construcción de prótesis u órganos artificiales internos", según la norma ISO/TR 10993-9 de 1994. Las biocerámicas requieren de temperaturas muy elevadas para su obtención, por lo que son difíciles de producir. Sin embargo, tienen una serie de características ventajosas que promueven su uso como biomateriales, como su inercia química, su excelente resistencia al desgaste, su alta resistencia a compresión y su excelente apariencia estética. Además, pueden utilizarse en forma

de polvo, gránulos o como matriz tridimensional o "scaffold" (27, 28), con porosidad y tamaño de poros variables.

Las cerámicas basadas en fosfatos cálcicos han sido utilizadas en los últimos 30 años en diferentes áreas médico-quirúrgicas, como la traumatología, odontología y cirugía maxilofacial para la regeneración de pérdidas de tejido óseo por diferentes causas, obteniéndose resultados satisfactorios gracias a su biocompatiblidad, bioactividad y osteoconductividad (29).

Muchos estudios han demostrado que los iones calcio y silicio son dos reguladores clave en la adhesión, proliferación y diferenciación de las ah-MSCs (29-32). Además, los iones calcio y fósforo son necesarios para el intercambio iónico entre los fluidos biológicos y la biocerámica (bioactividad). Por otra parte, el silicio juega un papel esencial en los eventos metabólicos relacionados con la formación ósea endocondral e intramembranosa y, junto con el calcio y el fósforo, favorecen la expresión de ciertos genes responsables de controlar el ciclo celular de osteoblastos animales y humanos, estimulando la producción de componentes de la matriz ósea (29, 33).

1.5.3.1. Mecanismo de bioactividad de las biocerámicas

Al sumergir las cerámicas bioactivas en disoluciones fisiológicas con una composición inorgánica similar al plasma humano, éstas son capaces de formar una capa de hidroxiapatito sobre su superficie. Este apatito es el componente mineral mayoritario del tejido óseo, como se ha mencionado anteriormente (34).

Hench (35) fue quien propuso, por primera vez, el mecanismo por el cual se forma esta capa de hidroxiapatito sobre la superficie de las cerámicas bioactivas expuestas a medios fisiológicos. Este proceso fue modificado por Kokubo (36), estableciendo las siguientes etapas:

- **Reacciones de intercambio iónico.**

- **Disolución de la sílice en forma de ácido silícico.**

- **Polimerización de la capa rica en SiO_2.**

- **Cristalización del apatito.**

Una vez se ha introducido la cerámica bioactiva en suero fisiológico artificial (SFA), comienza a producirse la lixiviación con intercambio iónico entre protones del medio fisiológico e iones modificadores de red de la biocerámica, como los iones Ca^{2+}, provocando la hidrólisis de los grupos de sílice y dando lugar a la formación de grupos silanol (figura 7a). Esta reacción provoca un incremento en la concentración de los grupos hidroxilo en la interfaz cerámica/disolución, dando lugar a un aumento del pH hasta niveles del orden de 10,5. Esta basificación del medio promueve la disolución de la red y formación de grupos silanol adicionales, según la reacción mostrada en la figura 7b. Además, se produce la disolución de la sílice en forma de ácido silícico [$Si(OH)_4$]. Los grupos vecinos de Si-OH condensan y polimerizan, dando lugar a una capa rica en sílice amorfa (figura 7c) (37).

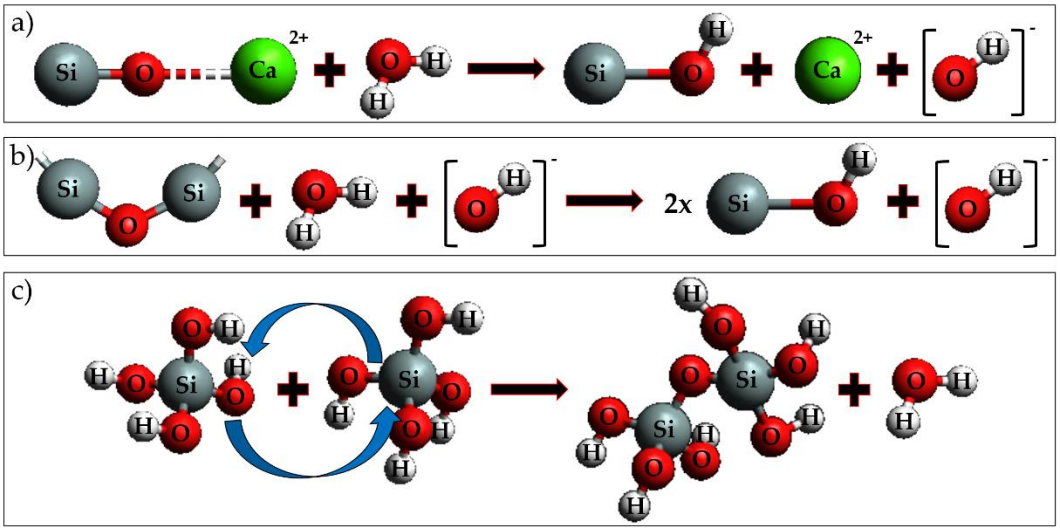

Figura 7. a) Intercambio entre protones del medio e iones modificadores de red con la formación de grupos silanol; b) Formación de grupos silanol adicionales; c) Polimerización de los grupos Si-OH y formación de sílice amorfa.

Finalmente, se produce la incorporación de aniones OH^-, CO_3^{2-}, o F^- sobre la superficie de sílice amorfa desde la disolución, provocando su cristalización y formación de carbohidroxiapatito o un fluorcarbohidroxiapatito. Inicialmente, los núcleos de hidroxiapatito aparecen dispersos sobre la superficie de la cerámica, figura 8a, pero a medida que estos núcleos aumentan tanto en número como en tamaño, se forman placas de hidroxiapatito por coalescencia de los núcleos, figura 8b.

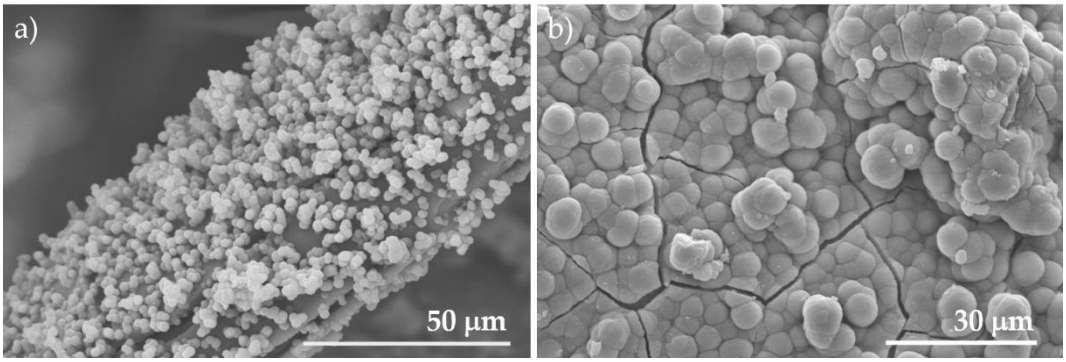

Figura 8. Micrografías SEM donde se observan: a) núcleos de mineralización dispersos sobre la superficie de una biocerámica; b) núcleos de mineralización formando capas de hidroxiapatito.

1.5.4. Diagramas de fases

Los diagramas de fases resumen gráficamente los intervalos de temperatura o presión en los que una, o varias fases, coexisten en condiciones de equilibrio termodinámico, permitiendo saber cómo se desarrollará su microestructura según la composición química y la temperatura, o presión, que se utilicen para su obtención (27, 35, 38). Por este motivo, los diagramas de fases son de vital importancia en la obtención de biomateriales. Sin embargo, no fue hasta finales de los años 60 cuando se comenzaron a utilizar estos diagramas para obtener materiales cerámicos, puesto que se pensaba que no se podía alcanzar el equilibrio a menos que existiera una fusión completa de los materiales de partida o una gran cantidad de fase líquida presente (39).

1.5.4.1. Diagrama de fases silicato dicálcico – fosfato tricálcico (C_2S-TCP).

Hace más de 100 años que se estudió el sistema Silicato Dicálcico – Fosfato Tricálcico (C_2S – TCP), conocido como el diagrama de fases del sistema Larnita-Whitlockita, por su importancia en metalurgia. Nurse y cols. estudiaron el diagrama en el año 1959 (40) y Fix y cols. en 1969 (41), (figura 9), añadiendo una serie de modificaciones, como la extensión de los campos de S.S (disolución sólida), donde la fase A funde congruentemente y la silicocarnotita presenta un campo mucho más estrecho, además de modificar el punto eutectoide Silicocarnotita-TCP.

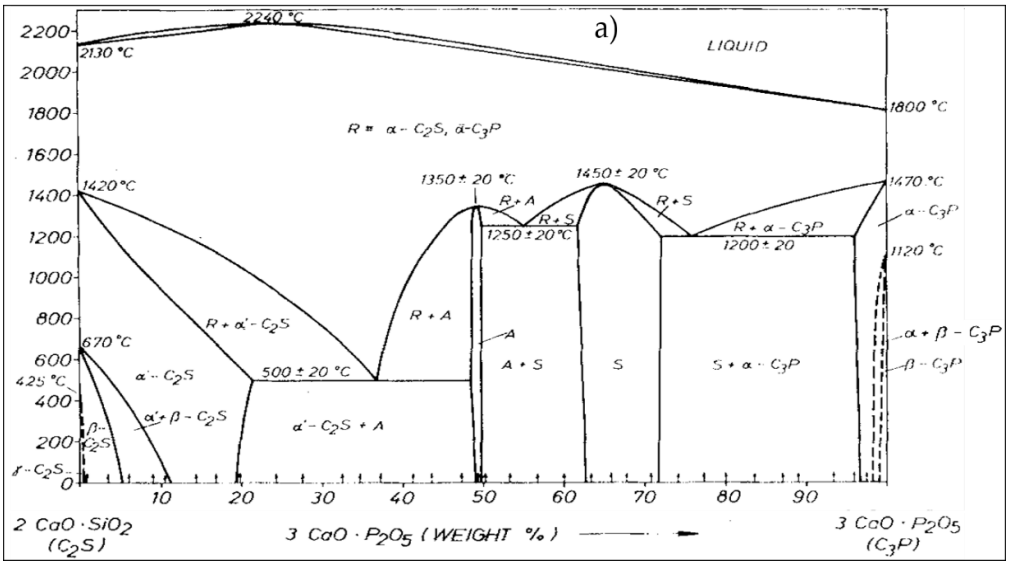

Figura. 9. Diagrama de fases C_2S-TCP propuesto por Fix y cols., en el año 1969.

1.5.5. Métodos de obtención de biocerámicas

Existe una gran variedad de métodos de obtención de biocerámicas porosas tridimensionales, como el prototipado rápido, procesado por electrospinning, espumado de gas, secado por congelación, reacción en estado sólido, replicación polimérica con barbotina y sol-gel, entre otros. Esta gran diversidad pone de manifiesto la dificultad existente para producir estructuras cerámicas con un tamaño de poro, porosidad e integridad mecánica controlados, características esenciales para un biomaterial que será utilizado en el área de la medicina regenerativa (42).

El método más simple y común para sinterizar materiales sólidos es la reacción en estado sólido. Su mayor desventaja es la necesidad de utilizar temperaturas muy elevadas y, en caso de querer obtener un material poroso, es necesario el uso de porógenos, como los surfactantes (43). Para evitar el uso de este tipo de sustancias, se puede utilizar el método de replicación polimérica, en el que una esponja es recubierta con una barbotina. Este método es uno de los más utilizados para obtener cerámicas con gran porosidad abierta interconectada. Sin embargo, todavía son necesarias temperaturas elevadas y surge un nuevo inconveniente: los materiales obtenidos a través de esta metodología suelen ser frágiles y tener bajas propiedades mecánicas, como consecuencia de su elevada porosidad. Por este motivo, una de las técnicas más empleadas a la hora de obtener estructuras porosas, es la combinación de la técnica sol-gel con la replicación polimérica, ya que requieren temperaturas de sinterización menos elevadas, y permiten ajustar el tamaño de poro de manera precisa.

1.5.5.1. Reacción en estado sólido

El método de reacción en estado sólido consiste en calentar dos sólidos no volátiles juntos para provocar su reacción y obtener un producto final. El procedimiento consiste en tomar cantidades estequiométricas de óxidos binarios, molerlos hasta obtener un tamaño de partícula adecuado y calentarlos en un horno durante varias horas en un crisol de alúmina o platino.

Las reacciones tienen lugar en la zona más superficial de las partículas y, una vez que las capas más externas han reaccionado, los reactivos difunden hacia la superficie, continuando con la reacción. Aumentar la temperatura permite acelerar la reacción sobre la interfaz y la difusión de los reactivos, por ello, esta técnica necesita de temperaturas elevadas para conseguir resultados homogéneos. Es muy importante que los materiales de partida se muelan hasta conseguir un tamaño de partícula muy pequeño, permitiendo una mejor mezcla, maximizando el área de contacto superficial y minimizando la distancia que los reactivos deben difundir. El contacto entre la superficie de las partículas también puede mejorarse prensando el polvo.

Además, es conveniente moler de nuevo el primer producto obtenido para llegar a obtener un producto final de fase pura. Por lo general, se llevan a cabo ensayos de prueba y error para conocer las mejores condiciones de reacción, analizando cada uno de los productos obtenidos por difracción de rayos X y determinando la pureza de las fases obtenidas (43).

1.5.5.2. Método de replicación polimérica

El método de replicación polimérica es una técnica que implica la impregnación de una estructura tridimensional con porosidad abierta con una barbortina, que consiste en una suspensión de partículas cerámicas junto con un aglutinante (44). Normalmente se utiliza una esponja de poliuretano (45) o una esponja marina natural (46), que actuarán como molde para obtener la estructura cerámica porosa final. Una vez recubierta, la esponja se seca lentamente y se calcina, dando lugar a una cerámica de porosidad abierta. Los pasos clave a tener en cuenta para este procedimiento son: la optimización de la barbotina, el proceso de secado tras la impregnación de la esponja con la barbotina y el tratamiento térmico de sinterización. Por este motivo hay que ser cuidadoso con la elección del polímero y con la velocidad de calentamiento utilizada, puesto que debe ser calcinado con una cantidad mínima de residuos y con rampas de calentamiento muy lentas, para así evitar el colapso de la estructura cerámica (47).

1.5.5.3. Sol-gel

El proceso sol-gel está basado en la hidrólisis de precursores alcóxidos, que forman un fluido inicial denominado sol. La posterior poli-condensación *in situ* de los alcóxidos forma un fluido de mayor densidad denominado gel. Se trata de un método interesante para obtener biocerámicas debido a que permite conseguir productos con una elevada pureza, homogéneos y, además, disminuye las temperaturas necesarias para obtenerlos respecto a otras técnicas, como la reacción en estado sólido (48).

Un precursor típico en este método es el tetraetil ortosilicato (TEOS), $Si(OC_2H_5)$, que se hidroliza en presencia de agua bajo condiciones ácidas o básicas, dando ácido silícico y formando una disolución (sol) que contiene nanopartículas

(18). La disolución en estado sol es una suspensión coloidal de partículas, formada como consecuencia de la unión y condensación (polimerización) de los ácidos silícicos, formando enlaces Si-O-Si y liberando agua o alcohol. Este sol es un líquido de baja viscosidad, por lo que podemos introducirlo en cualquier molde y obtener la forma final deseada.

Con el tiempo se produce la coalescencia de las partículas, formando una red tridimensional y provocándose la gelificación del conjunto. Este gel es una red inorgánica húmeda de sílice, unida covalentemente, con una viscosidad mayor que la del sol del que procede. El líquido remanente es eliminado sometiendo las muestras a un proceso de secado, que provoca la deshidratación de la muestra y su estabilización química al eliminar parcialmente los enlaces silanol (Si-OH) de la superficie de los poros de la red, obteniendo un sólido poroso muy estable químicamente.

Finalmente, se aplican temperaturas más elevadas con el fin de eliminar la esponja de poliuretano, así como un gran número de grupos silanol, formando enlaces Si-O-Si, que proporcionan mayor resistencia mecánica a la estructura. Además, se eliminan los restos de disolvente y se descomponen en forma de aniones (grupos CO_3^{2-}), permitiendo la reorganización y cristalización de la estructura (18, 37, 43).

2. HIPÓTESIS

2. HIPÓTESIS

En la sociedad actual existen términos como esperanza de vida, longevidad, calidad de vida, envejecimiento activo y saludable que indican la creciente inquietud por mejorar la salud de la población, en concreto, la del sistema músculo-esquelético. La necesidad de regenerar el tejido óseo dañado, evitando las limitaciones e inconvenientes del uso del injerto óseo autólogo, implica el desarrollo y caracterización de nuevos biomateriales cerámicos que cumplan con los criterios establecidos por la triada de la regeneración ósea: osteoconducción, osteoinducción y osteogénesis.

La hipótesis de la presente Tesis Doctoral es que diferentes cerámicas, obtenidas a partir de los diagramas de fases C_2S – TCP, CaO – P_2O_5 – SiO_2, CaO – SiO_2 – K_2O – MgO y CaO – SiO_2 – K_2O – Na_2O, son capaces de interaccionar con el medio que les rodea, al mismo tiempo que facilitan la proliferación y diferenciación de ah-MSCs en células de estirpe osteoblástica capaces de formar tejido óseo, favoreciendo la interacción del implante con el tejido óseo circundante. Esto es así gracias a su estructura porosa (osteoconducción) y composición iónica (osteoinducción), puesto que iones como el silicio, calcio, fósforo, sodio, potasio y magnesio permiten la colonización celular y estimulan la producción de determinados componentes de la matriz extracelular del tejido óseo.

3. OBJETIVOS

3. OBJETIVO GENERAL

El objetivo general planteado en la presente Tesis Doctoral es el diseño, preparación, caracterización y estudio *in vitro* e *in vivo* de estructuras soporte con elevada micro y macroporosidad abierta. La composición química de estas estructuras se hará en base al diagrama bifásico C_2S – TCP, trifásico CaO – P_2O_5 – SiO_2 y cuaternarios CaO – SiO_2 – K_2O – MgO y CaO – SiO_2 – K_2O – Na_2O, obteniendo materiales cerámicos con cristalinidad monofásica y multifásica. La modificación del tipo de ión, así como de su concentración, permitirá el ajuste de la tasa de reabsorción de los distintos materiales, con objeto de optimizar su capacidad osteoinductiva sobre las ah-MSCs.

3.1. OBJETIVOS ESPECÍFICOS

1. Diseñar una nueva metodología para el desarrollo de matrices cerámicas porosas tridimensionales mediante los métodos sol-gel y replicación polimérica, según los siguientes diagramas de fases:
    a. SiO_2 – CaO – P_2O_5
    b. MgO – K_2O – CaO – SiO_2
    c. Na_2O – K_2O – CaO – SiO_2

2. Caracterizar estas matrices porosas desde el punto de vista microestructural y mineralógico, además de verificar su composición química.

3. Estudiar su bioactividad *in vitro*, sumergiendo las muestras en suero fisiológico artificial.

4. Revisar el subsistema fase A de Nurse – Silicocarnotita, dentro del diagrama de fases binario C_2S-TCP, propuesto por Fix, y cols., para comprobar las temperaturas y concentraciones de reactivos necesarias para obtener cada una de las fases y microestructuras indicadas en el diagrama.

5. Obtener nuevos biomateriales con microestructura controlada mediante la técnica de reacción en estado sólido, siguiendo el subsistema fase A de Nurse – Silicocarnotita, y su posterior caracterización.

6. Realizar estudios de citotoxicidad de las cerámicas con microestructura eutectoide utilizando ah-MSCs.

7. Evaluar el efecto inicial de la liberación iónica de las cerámicas eutectoides, sobre la diferenciación osteogénica de una población de ah-MSCs, en presencia y ausencia de suplemento osteogénico en el medio de cultivo celular.

8. Obtener y caracterizar una biocerámica bifásica, compuesta por fase A y Silicocarnotita, con micro y macroporosidad interconectada utilizando el método de replicación polimérica con una barbotina.

9. Determinar la influencia de la topografía de los micro y macroporos, en términos de resorción ósea y osteoconductividad *in vivo*, utilizando un modelo animal (conejos de Nueva Zelanda).

4. ARTÍCULO 1

Ceramics International 43 (2017) 6548–6553

Contents lists available at ScienceDirect

Ceramics International

journal homepage: www.elsevier.com/locate/ceramint

New 3D stratified Si-Ca-P porous scaffolds obtained by sol-gel and polymer replica method: Microstructural, mineralogical and chemical characterization

Patricia Ros-Tárraga[a,*], Angel Murciano[b], Patricia Mazón[b], Sergio A. Gehrke[c], Piedad N. De Aza[a]

[a] Instituto de Bioingenieria, Universidad Miguel Hernandez, Avda. Ferrocarril s/n. Elche, Alicante 03202, Spain
[b] Departamento de Materiales, Óptica y Tecnologia Electrónica, Universidad Miguel Hernández, Avda. Universidad s/n, Elche, Alicante 03202, Spain
[c] Biotecnos Research Center, Rua Dr. Bonazo n° 57 Santa Maria, RS 97015-001, Brazil

ARTICLE INFO

Keywords:
Sol-gel
Tissue engineering
Polymer sponge replica

ABSTRACT

The aim of this research was to develop and characterize a novel stratified porous scaffold for future uses in bone tissue engineering. In this study, a calcium silicophosphate porous scaffold, with nominal composition 29.32 wt % SiO_2 – 67.8 wt% CaO – 2.88 wt% P_2O_5, was produced using the sol-gel and polymer replication methods. Polyurethane sponges were used as templates which were impregnated with a homogeneous sol solution and sintered at 950 °C and 1400 °C during 8 h. The characteristics of the 3D stratified porous scaffolds were investigated by Scanning Electron Microscopy, X-Ray Diffraction, Fourier Transform Infrared Spectrometry, Diametric Compression of Discs Test and Hg porosimetry techniques. The result showed highly porous stratified calcium silicophosphate scaffolds with micro and macropores interconnected. Also, the material has a diametrical strength dependent on the number of layers of the stratified scaffolds and the sintering temperature.

1. Introduction

In the last few decades, health improvements have allowed a significant increase of the life expectancy of the population, increasing the incidence of problems related to bone and joint degeneration, such as fractures, osteoporosis and bone metastasis too. In this sense, it is estimated that 50% of chronic patients in developed countries with more than 50 years will suffer bone problems, doubling it by 2020 [1–3].

Traditionally, these bone lesions are treated by reconstructive surgery, using autologous, allogeneic or xenogeneic implants [1], which involve major restrictions as availability of tissue or immunological responses. Given these restrictions, it has been necessary to develop a scientific discipline such as tissue engineering, able to develop viable tissue for implantation in the human body and to maintain or restore lost functionality.

Tissue engineering is a science which studies different ways to achieve the regeneration of diseased tissues. To get it, this field uses scaffolds or porous extracellular 3D matrices, which allow cell migration, vascularization and nutrient diffusion [4,5]. These matrices need to have the appropriate physical and biological properties such as pore size and structure, surface topography, chemical composition, mechanical strength and degradation rate [6,7]. These characteristics are capable to induce optimal osteogenesis throughout the scaffolds. For this reason, and because they exhibit an appropriate bioactivity, ceramics are excellent candidates for developing these 3D scaffolds, avoiding the process of stress shielding [8–14].

There are a lot of ways to develop 3D porous scaffold: rapid prototyping, electrospinning processing, gas foaming, freezing-drying, polymer sponge replica, salt leaching, dual phase mixing and gel casting [15]. This variety of production methods shows the difficulty of producing ceramic scaffolds with controlled pore size, porosity and mechanical integrity [16]. Of the above methodologies, the polymer sponge replica is one of the most extensively used to obtain ceramic foams with large-size interconnected pores (200 μm to 3 mm).

The technique essentially consists in the impregnation of a polymer sponge with a ceramic slurry. After that, the sponge coating is drying by thermal treatment at low temperature, and finally, the sponge is removed and the ceramic is sintered at high temperature. The porous scaffolds obtained by this technique, or by means the methodologies above cited, usually are fragile with low mechanical properties derived of a highly porous structure, with high compression strength and very lower tensile strength. In order to obtain bioactive ceramics as well as suitable surface chemistry for cell attachment, an additional sacrifice in mechanical strength is performed, since a ceramic composition with this properties is used and not the ceramic composition with the higher

* Corresponding author.
E-mail address: p.ros.tarraga@gmail.com (P. Ros-Tárraga).

http://dx.doi.org/10.1016/j.ceramint.2017.02.081
Received 11 January 2017; Received in revised form 13 February 2017; Accepted 17 February 2017
Available online 20 February 2017

mechanical properties. In order to can use different compositions in the same sample, supplying the properties of an ideal porous scaffold, it would be interesting to get a method which allows to generate layered materials in a short period of time [17,18]. A set of layers can be dedicated to enhance the mechanical properties, generating the core of the porous material, and other set of layers can be dedicated to provide bioactivity, with a controllable degradation and resorption rate to match new bone tissue growth. Therefore, the most external ceramic layers are reserved to stimulate the cellular response. Furthermore, additional control of the porous size is possible thanks to the number of layers: a higher number of them imply a diminution of initial pore of polymeric sponge, obtaining porous structures with adjustable pore dimension, extending the versatility of ceramics.

In this sense, this work presents an experimental methodology to obtain stratified porous ceramics. In order to obtain the coating solution of polymeric sponge, the sol-gel process was used, method based on the hydrolysis and condensation reaction of organometallic compounds. It represents an advance from the conventional melting technique, making possible the obtention of materials of controlled shape at lower temperatures with a really high purity.

2. Material and methods

2.1. Material preparation

Stratified porous scaffolds were prepared using 29.32 wt% SiO_2 – 67.8 wt% CaO – 2.88 wt% P_2O_5 as sol-gel composition, after performing a serie of tests and selecting the most optimal, with $Si(OC_2H_5)$, $(C_2H_5)_3PO_4$ (TEOS, Aldrich-Tetraethyl Orthosilicate 98%; and TEP, Aldrich-Triethy Phosphate > 99.8%, respectively) and calcium carbonate ($CaCO_3$ Sigma, > 99 wt%) as reactants. In order to obtain the cited composition, it was necessary to dissolve 4.33 g of $CaCO_3$ in 2 mL of distilled water and to get a homogeneous solution adding HCl (HCl 37%, Applichem Panreac) drop by drop. This allowed achieving a transparent solution with a pH between 2 and 3.

Simultaneously, sol-gel method started with the hydrolysis of the mixture of 10.9 mL of TEOS, 1.63 mL of TEP and 5 mL of ethanol 97° using 10 mL of HCl. After that, it was added 10 mL of distilled water, and after 30 s, 7 g of $CaCO_3$. This allowed neutralize the medium to reach a value of pH between 2 and 3, like the first solution. Once this done, both solutions were mixed, obtaining a final transparent solution with a pH between 2 and 3.

In the resultant sol solution, a polyurethane sponge of 0.31 cm^3 (1 cm diameter and 0.4 cm height), which will act as a template of the porous bioceramic, was immersed into the previous solution, removing the excess of it by squeezing the sponge. Finally, the template covered with the sol solution was dried during 20 min at 160–180 °C.

In order to supply higher mechanical strength to the final ceramics, additional immersions were realized, obtaining a new layer for each immersion. To remove the excessive solution and not to break the ceramic structures, the samples were centrifuged at a rate sufficient to permit removal the excess of the sol solution. In function of needs, the composition of the sol and the number of immersions can be modified in order to improve the mechanical properties, bioactivity or change the response of cell adhesion with surface of porous scaffold, as well as to modify the pore size.

After each immersion, it was carried out the drying of the remaining solution within the sponge in order to evaporate the ethanol and water present at the 3D network. This allowed a better condensation of the structure, obtaining higher mechanical properties.

In this work the composition of sol solution was always the same and the sponges were immersed in the solution a total of 8, 10 and 12 times.

Once the green 3D structure has been obtained, they were sintered using two different heat treatments: on one hand, samples were sintered using a heating rate of 17.3 °C/h, reaching a final temperature of 950 °C. On the other hand, it was used a heating rate of 25.4 °C/h, reaching a final temperature of 1400 °C. These temperatures were selected in order to getting appropriate mechanical properties and removing the organic component of the sample (polyurethane sponge). Once it has reached the desired temperature, the samples were maintained during 8 h at that temperature. Finally, the samples were subjected to a slow cooling, which lasts about 24 h.

2.2. Characterization of the 3D ceramics

The apparent density measurement of the sintered ceramics was performed using the Archimedes' method by immersion in Hg, using an electric balance to determine the mass of the samples. Strength was determined by the Brazilian test or the Diametric Compression of Discs Test (DCDT) following the procedure described elsewhere [19,20]. The test was conducted on discs with a diameter of ~20 mm (D) and a thickness (t) of ~6 mm, (t/D ~0.3). The disk were placed between two stainless steel loading plates with their faces perpendicular to the loading plates in a universal testing machine (model AME-5 kN, Técnica Industrial Oswaldo Filizola Ltda, Guarulhos, Brazil). Load was applied at a displacing rate of 1 mm/min of the machine frame. Results of 10 valid test were used to calculate the diametrical strength.

Macroscopic morphology structure has been realized using a Nikon SMZ1500 stereomicroscope equipped with a Nikon DXM1200F digital camera.

The microstructure of the material was characterized by Scanning Electron Microscopy fitted with Energy-Dispersive X-Ray Spectroscopy (SEM-EDX, SEM-Hitachi S-3500N and INCA system, by Oxford Instruments Analytical, UK, respectively) covering the samples with palladium, as described in previous literature [14].

To evaluate the material's composition, X-Ray Diffraction (XRD) patterns have been obtained in order to determine crystalline phases. For this, it has been used a Bruker-AXS D8Advance automated diffractometer using $CuK_\alpha 1.2$ radiation (1.54056 Å). Data were collected in the Bragg-Brentano (θ/2θ) vertical geometry (flat reflection mode) between 20° and 37° (2θ) at 0.05° steps, counting 6 s per step and the X-ray tube was operated at 40 kV at 30 mA, as described in previous literature [14]. The difractograms of samples were compared with the database provide by Joint Committee on Powered Diffraction Standards (JCPDS) database.

Finally, to get chemical composition of the samples, it has used a Fourier Transform Infrared Spectrometry (FTIR) spectrometer IF66s, Bruker. For this, it was necessary to generate a potassium bromide (KBr) tablet using 1 mg of KBr for each 130–140 mg of sample and press them at 10,000 t. Data were collected between 4000 and 400 cm^{-1} at 20 °C and 300 scans of resolution.

3. Results and discussion

Cylindrical scaffolds were fabricated using a modified polymer replication method and displayed in Fig. 1, showing well-controlled open pores and uniform dimensions. Fig. 1 shows the macroscopy morphology of the stratified 3D porous ceramic as a representative of all immersion times.

Microstructural parameters were stablished to comprehensively characterize the 3D microstructure of the material (Table 1).

The thermal treatments generated shrinkage in all ceramics, as shown in Table 1. The tendency of the density was to increase with the increasing amounts of shrinkage and the number of immersions in sol solution. In this way, it was possible to observe that the sample which shows the highest shrinkage is 3D-1400/12, showing also the highest density, although there are no great differences between them.

Results of 10 valid tests were used to calculate the diametrical strength using the procedure of ISO 14801. Failure occurs through the diametrical plane and the specimens are broken in two similar pieces which correspond to a load drop in the load-displacement curve

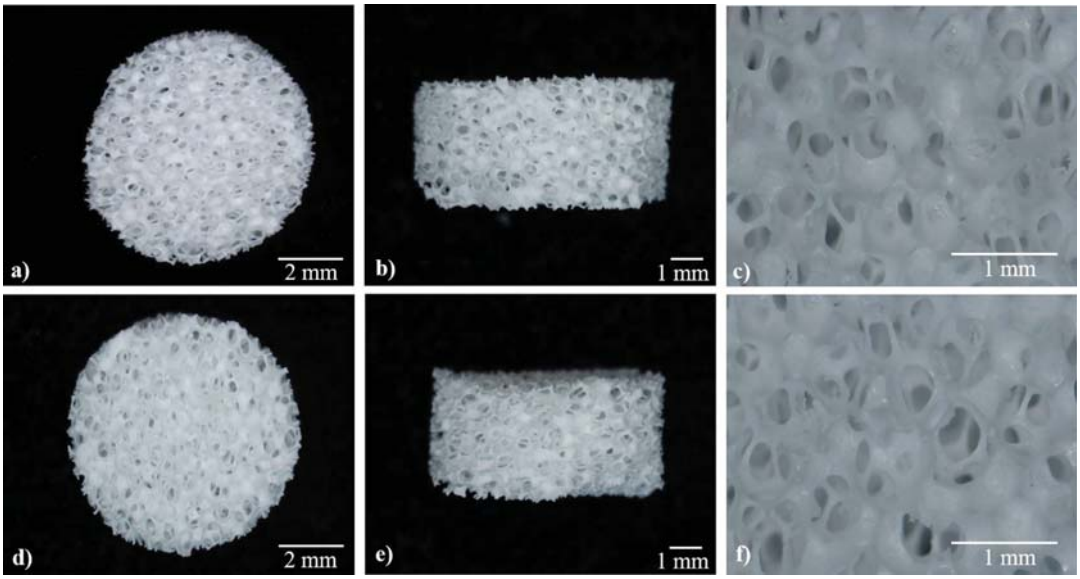

Fig. 1. Optical micrographs of the stratified 3D porous scaffolds and macroporous structure (a-c) after sintering at 950 °C and (d-f) after sintering at 1400 °C with 8 immersions.

registered during the test (Table 1 and Fig. 2). The obtained strength values for the material were relatively low due to the porosity of the ceramic. The low strength values, as usually found for highly porous materials, are due to the fracture occurring through the collaborative action of the pores. The results were directly related to the density of the material. This finding agrees well with other data reported in the literature [21,22].

We have employed a new sol-gel method to produce multi-layer structures, consisting of immersing the material into a sol solution as many times as needed. Figs. 3 and 4 demonstrate the importance of the number of dives.

Figs. 3 and 4 show the open porosity microstructure of the two ceramics obtained (3D-950 Fig. 3 and 3D-1400 Fig. 4). Fig. 3a shows the initial polyurethane sponge for comparative purpose. This structure remains intact after 8 immersions in the sol solution, maintaining the shape and size of the pores of the polyurethane foam. Instead, when the

Table 1
Microstructural parameters of the 3D ceramics.

	Density (g/cm^3)	Shrinkages (%)	Open porosity (%)	Pore size (μm)	Diametrical Strength (MPa)
3D–950/8	0.258 ± 0.031	51.68 ± 0.05	95.0 ± 2	400×280	0.18 ± 0.02
3D–950/10	0.259 ± 0.026	51.70 ± 0.06	94.8 ± 3	397×279	0.19 ± 0.02
3D–950/12	0.260 ± 0.051	51.71 ± 0.05	94.7 ± 1	394×277	0.19 ± 0.02
3D–1400/8	0.262 ± 0.033	62.01 ± 0.04	90.0 ± 2	380×250	0.39 ± 0.02
3D–1400/10	0.262 ± 0.034	62.03 ± 0.06	89.9 ± 2	376×250	0.40 ± 0.02
3D–1400/12	0.263 ± 0.022	62.12 ± 0.06	89.7 ± 3	375×248	0.40 ± 0.02

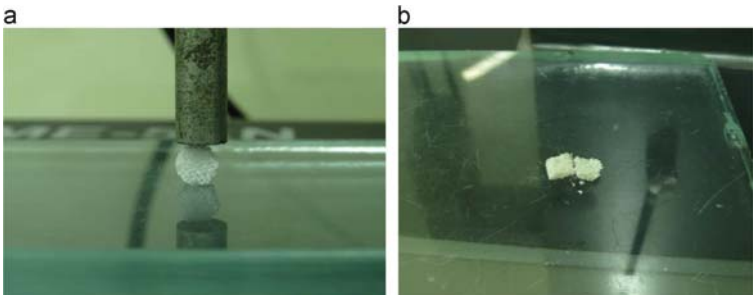

Fig. 2. Mechanical test used in this work: (a) the Diametric Compression of Discs Test (DCDT); (b) aspect of a valid specimen after testing showing the straight fracture through the diametral plane.

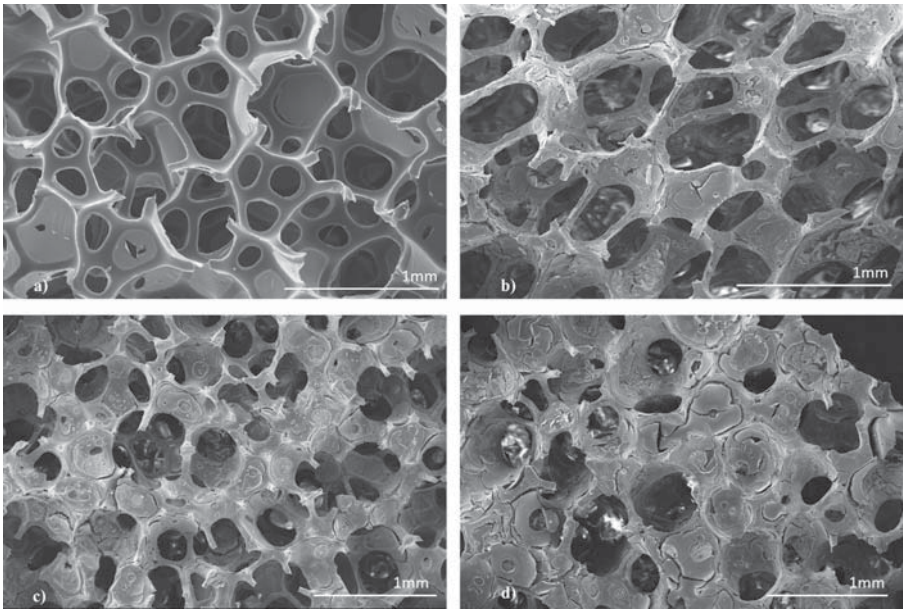

Fig. 3. a) SEM micrograph of the polyurethane sponge, b) SEM micrograph of the 3D-950 biomaterial with 8, c) 10 and d) 12 immersions in sol solution.

number of dives is increased to 10 and 12 immersions, it can be seen the plugging of the pores (Figs. 3c, d and 4b, c and Table 1).

The pore channels in both ceramics were completely interconnected and distributed throughout the whole scaffold, which were necessary for new tissue ingrowth and vascularization construct (Table 1) [6,7]. A detail of the different layers is shown in Fig. 4c where it is possible to distinguish the latest five layers.

The composition of the sample determined by quantitative analysis by EDX (Fig. 4d) in different points of the 3D-1400/8 ceramic surface (as a representative date of all the ceramics) was 30.24 wt% of SiO_2,

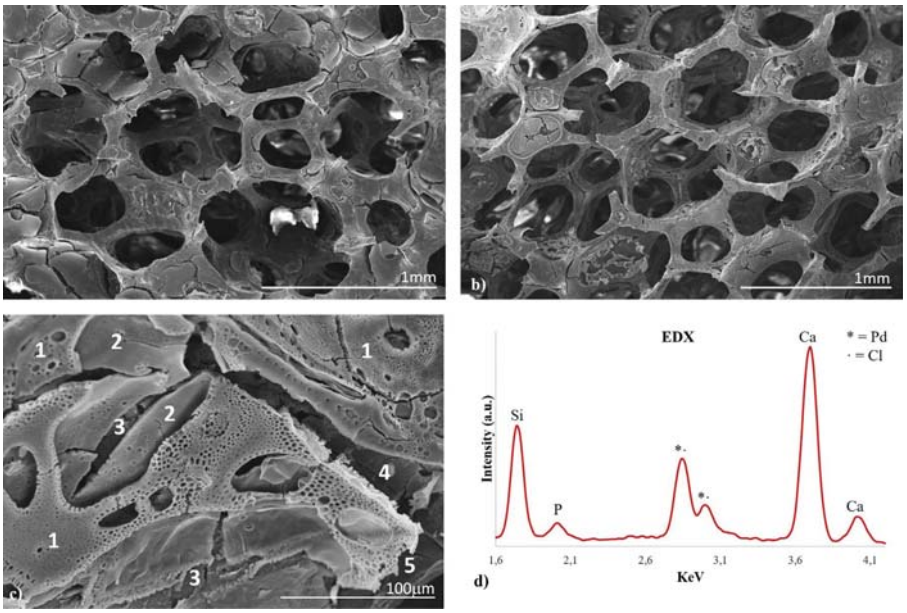

Fig. 4. SEM micrographs of the 3D-1400 ceramics with a) 8, b) 10 and c) 12 immersions in sol-solution (numbers are the latest five layers) d) EDX analysis.

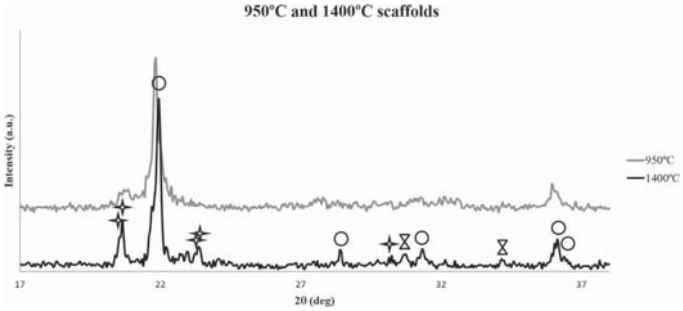

Fig. 5. XRD diffraction patterns of bioceramics 3D-950/8 and 3D-1400/8. ○=cristobalite; ✦= tridymite; ⧖=β-Tricalcium phosphate (TCP).

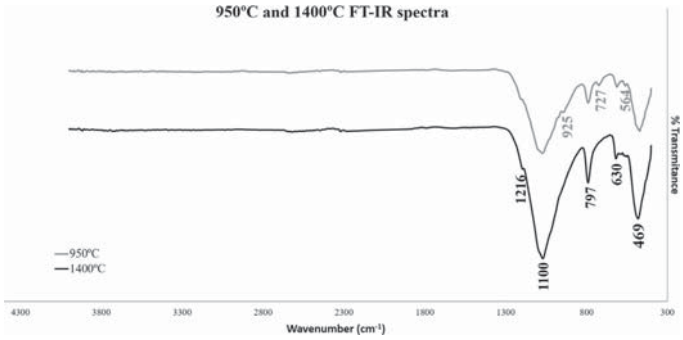

Fig. 6. FT-IR spectra of 3D-950/8 and 3D-1400/8 bioceramics.

64.07 wt% of CaO and 2.84 wt% of P_2O_5, closed to the composition of the synthesized material (29.32 wt% SiO_2/67.8w%t CaO/2.88w%t P_2O_5).

Phase composition of the 3D-950/8 and 3D-1400/8 ceramic scaffolds as a representative of all the scaffolds obtained is shown in Fig. 5. It could be found in the patterns of both sintered sponges that are composed fundamentally by a major amorphous calcium silicate phase with small amounts of silica (cristobalite and tridymite – JCPDS 82–1403 and JCPDS 70–8142, respectively), in the case of the ceramic sintered at 950 °C, or small amounts of tricalcium phosphate (β-TCP – JCPDS 86–1585), in ceramics sintered at 1400 °C.

When temperature is increased to 1400 °C, the SiO_2 phases acquire crystallinity and appears a new TCP phase, β-TCP (JCPDS 86-1585), which correspond with the low temperature form of TCP [23–25]. There were no other phases generated during sintering process.

The presence of polymorphous phases of SiO_2 (cristobalite and tridymite) is due to the sol-gel process used in the porous structure elaboration. In this method, Si-O-Si bonds are established, contributing to their stabilization.

The presence of cristobalite should not appear at temperatures below 1470 °C. However, it is demonstrated that traces of phosphorus in this kind of samples contributes the SiO_2 phases crystallization at low temperatures [26]. For this reason, phosphorus traces are responsible to the appearance of cristobalite at just 950 °C.

Finally Fig. 6 shows the FT-IR spectra of samples 3D-950/8 and 3D-1400/8 as a representative of all the 3D ceramics obtained. The spectras of crystalline silicates and phosphates are dominated by the internal modes of $SiO4^{-4}$ and $PO4^{-3}$ tetrahedral units. The interpretation of the spectra is not obvious because of the overlapping and combination of bands corresponding to SiO_4 and PO_4 groups which are forming the structure. In fact, due to similarities of SiO_4^{4-} and PO_4^{3-} tetrahedral molecular units, crystalline phases as silica, calcium silicates as well as tricalcium phosphates and hydroxiapatite, share an important number of similarly spaced vibrational modes [27–29].

The presence of the three main vibrational modes of the Si-O-Si groups appears in the region between 400 and 1300 cm^{-1}. Close of the 460 cm^{-1} Si-O-Si vibration can be observed and it is followed by bands between 700 and 800 cm^{-1}, which are identified as a flexion type vibration of Si-O-Si group, in which oxygens move at right angles to the Si-Si lines and in the Si-O-Si planes. And finally, the wide band between 1000 and 1300 cm^{-1} is associated with the asymmetrical stretching Si-O-Si mode, where the bridging oxygen atoms move in the direction opposite to their Si neighbors and roughly parallel to the Si-Si lines. However, when this kind of structures are modified with alkali-earth elements, like calcium, appears a new band between 890 and 975 cm^{-1}, corresponding with the stretching mode Si-O with one non-bridging oxygen per SiO_4 (Si-O-NBO) [30,31]. The addition of this kind of alkali-earth elements into the silicon promotes the appearance of partial breakages in the 3D network, weakening its cohesion and decreasing its stability and, therefore, causing a reduction in its softening temperature. For each additional molecule modifier added, Si-O-Si bonds are broken, permitting the incorporation of them into the network. Thus, the two neighboring silicon bond to two different oxygens, appearing two non-bridging oxygen, which attach to a single silicon atom instead of two of them, constituting points of reticular discontinuity. Note that this damage caused by this type of molecules is partly compensated thanks to its double positive charge, so such cations act as a bridge between two oxygen ions.

Furthermore, considering the presence of OH groups in the formation of silicon-based ceramics, it can be observed a band around 630 cm^{-1} and another one located between 900 and 980 cm^{-1}. The first one is associated with vibrational movements of OH groups and the

Table 2
Infrared vibrational modes of bioceramics stabilized at 950 °C.

IR frequency (cm^{-1})	Vibrational mode/group	Reference
440–475	PO_4^{3-}	[34]
450–490	Si-O-Si rocking	[30,31]
500–600	PO_4^{3-} bending	[30]
632	OH	[32,33]
760–850	Si-O-Si bending	[30]
890–975	Si-O-NBO stretching	[30]
900–970	PO_4^{3-} symmetrical stretching	[30]
900–980	Si-OH symmetrical stretching	[30]
1000–1100	PO_4^{3-} asymetrical stretching	[30]
1000–1300	Si-O-Si asymmetrical stretching	[30]

second one with an asymmetric stretching of Si-OH groups [30–33].

Moreover, PO_4^{3-} groups are present in the samples. Its presence is demonstrated by numerous bands located at 440–475 cm^{-1}, 500–600 cm^{-1}, 900–970 cm^{-1} and 1000–1100 cm^{-1}. The second one corresponds with a stretching movement, and the rest until the last one, correspond with a symmetric and asymmetric stretching of phosphate groups [30,32].

Nor was the interpretation of the FTIR spectra of the scaffolds obvious because the bands that correspond to SiO4 and PO4 groups overlapped. For a better understanding of these results observed in the FTIR spectra, each vibrational mode has been associated with the different vibrational modes in the following table (Table 2).

4. Conclusions

A new methodology has been developed to obtain a stratified porous 3D ceramic at different temperatures, whose microstructural study has shown a highly interconnected porosity, with an average pore size between 375–400 μm and a Ca/P ratio of 13.09. The mineralogical study shows two sintered sponges composed fundamentally by a major amorphous calcium silicate phase with small amounts of silica (950 °C) silica or small amounts of silica and tricalcium phosphate (1400 °C). Also, the presence of Si, Ca and P is demonstrated with the FT-IR study, in which we can see the presence of Si-O-Si, Si-OH, PO_4^{3-} groups. The diametrical strength goes from values 0.18 ± 0.02 for eight layers and 950 °C to reach 0.40 ± 0.02 for 12 layers and 1400 °C, so the mechanical properties are highly dependent on the number of layers of the stratified scaffolds and the sintering temperature.

For this reason, this methodology will allow us to create new customized materials according to the needs of each situation. We will be able to create materials with a high resistant core and high bioactivity coverings or vice versa, depending on the place where you would place the bone implant.

Acknowledgments

Part of this work has been supported by a Ministry of Economy and Competitiveness (MINECO) contract grant number: MAT2013-48426-C2-2-R.

References

[1] R. Agarwal, A.J. Garcia, Biomaterial strategies for engineering implants for enhanced osseointegration and bone repair, Adv. Drug Deliv. Rev. 94 (2015) 53–62.
[2] M. Navarro, A. Michiardi, O. Castano, J.A. Planell, Biomaterials in orthopaedics, J. R. Soc., Interface / R. Soc. 5 (2008) 1137–1158.
[3] J.R. Jones, P.D. Lee, L.L. Hench, Hierarchical porous materials for tissue engineering, Philosophical transactions, Ser. A, Math. Phys., Eng. Sci. 364 (2006) 263–281.
[4] P.N. De Aza, J.E. Mate-Sanchez de Val, C. Baudin, C. Perez Albacete-Martinez, A. Armijo Salto, J.L. Calvo-Guirado, Bone neoformation of a novel porous resorbable Si-Ca-P-based ceramic with osteoconductive properties: physical and mechanical characterization, histological and histomorphometric study, Clin. Oral. Implants Res. 27 (2016) 1368–1375.
[5] P. Ros-Tárraga, R. Rabadan-Ros, A. Murciano, L. Meseguer-Olmo, P. De Aza, Assessment of effects of Si-Ca-P biphasic ceramic on the osteogenic differentiation of a population of Multipotent adult human stem cells, Materials 9 (2016) 969.
[6] R. Rabadan-Ros, P. Velásquez, L. Meseguer-Olmo, P. De Aza, Morphological and structural study of a novel porous nurse's a ceramic with osteoconductive properties for tissue engineering, Materials 9 (2016) 474.
[7] P. Ros-Tárraga, P. Mazón, M. Rodríguez, L. Meseguer-Olmo, P. De Aza, Novel resorbable and osteoconductive calcium silicophosphate scaffold induced bone formation, Materials 9 (2016) 785.
[8] C. Gao, Y. Deng, P. Feng, Z. Mao, P. Li, B. Yang, J. Deng, Y. Cao, C. Shuai, S. Peng, Current progress in bioactive ceramic scaffolds for bone repair and regeneration, Int. J. Mol. Sci. 15 (2014) 4714–4732.
[9] S.K. Padmanabhan, F. Gervaso, M. Carrozzo, F. Scalera, A. Sannino, A. Licciulli, Wollastonite/hydroxyapatite scaffolds with improved mechanical, bioactive and biodegradable properties for bone tissue engineering, Ceram. Int 39 (2013) 619–627.
[10] V. Karageorgiou, D. Kaplan, Porosity of 3D biomaterial scaffolds and osteogenesis, Biomaterials 26 (2005) 5474–5491.
[11] D.W. Hutmacher, Scaffolds in tissue engineering bone and cartilage, Biomaterials 21 (2000) 2529–2543.
[12] S.M. Naga, H.F. El-Maghraby, E.M. Mahmoud, M.S. Talaat, A.M. Ibrhim, Preparation and characterization of highly porous ceramic scaffolds based on thermally treated fish bone, Ceram. Int 41 (2015) 15010–15016.
[13] G.J. Lugo, P. Mazón, C. Baudin, P.N. De Aza, Nurse' s A-Phase: Synthesis and characterization in the binary System Ca2SiO4–Ca3 (PO4) 2, J. Am. Ceram. Soc. 98 (2015) 3042–3046.
[14] G.J. Lugo, P. Mazón, P.N. De Aza, Material processing of a new calcium silicophosphate ceramic, Ceram. Int 42 (2016) 673–680.
[15] M. Vallet-Regi, D. Arcos, A.J. Salinas, M. Colilla, J. Peña Lope, M. Mila, O. Castaño, J.A. Planell, M.V. Cabañas, I. Izquierdo-Barba, S. Pérez-Amodio, E. Engel, M. Manzano, B. González, A. Baeza, Bioceram. Clin. Appl. (2014).
[16] I. Denry, L.T. Kuhn, Design and characterization of calcium phosphate ceramic scaffolds for bone tissue engineering, Dent. Mater.: Off. Publ. Acad. Dent. Mater. 32 (2016) 43–53.
[17] I.K. Jun, J.H. Song, W.Y. Choi, Y.H. Koh, H.E. Kim, Porous hydroxyapatite scaffolds coated with bioactive apatite-wollastonite glass-ceramics, J. Am. Ceram. Soc. 90 (2007) 2703–2708.
[18] T.Y. Yang, W.Y. Kim, S.Y. Yoon, H.C. Park, Macroporous silicate ceramics prepared by freeze casting combined with polymer sponge method, J. Phys. Chem. Solids 71 (2010) 436–439.
[19] I.H. García-Páez, R.G. Carrodeguas, H. Antonio, C. Baudín, P. Pena, Effect of Mg and Si co-substitution on microstructure and strength of tricalcium phosphate ceramics, J. Mech. Behav. Biomed. Mater. 30 (2014) 1–15.
[20] Advanced technical ceramics – Mechanical properties of monolithic ceramics at room temperature – Part 5: Statistical analysis (Endorsed by AENOR in January of 2007).
[21] Q.Z. Chen, I.D. Thompson, A.R. Boccaccini, 45S5 Bioglass®-derived glass–ceramic scaffolds for bone tissue engineering, Biomaterials 27 (2006) 2414–2425.
[22] S. Teixeira, M. Rodriguez, P. Pena, A. De Aza, S. De Aza, M. Ferraz, F. Monteiro, Physical characterization of hydroxyapatite porous scaffolds for tissue engineering, Mater. Sci. Eng.: C. 29 (2009) 1510–1514.
[23] N. Jinlong, Z. Zhenxi, J. Dazong, Investigation of phase evolution during the thermochemical synthesis of tricalcium phosphate, J. Mater. Synth. Process. 9 (2001) 235–240.
[24] R.G. Carrodeguas, A.H. De Aza, X. Turrillas, P. Pena, S. De Aza, New approach to the β→ α polymorphic transformation in magnesium-substituted tricalcium phosphate and its practical implications, J. Am. Ceram. Soc. 91 (2008) 1281–1286.
[25] R.G. Carrodeguas, S. De Aza, α-Tricalcium phosphate: synthesis, properties and biomedical applications, Acta Biomater. 7 (2011) 3536–3546.
[26] S. Padilla, J. Roman, A. Carenas, M. Vallet-Regi, The influence of the phosphorus content on the bioactivity of sol-gel glass ceramics, Biomaterials 26 (2005) 475–483.
[27] M. Handke, M. Sitarz, M. Rokita, E. Galuskin, Vibrational spectra of phosphate–silicate biomaterials, J. Mol. Struct. 651 (2003) 39–54.
[28] A. Jillavenkatesa, R. Condrate Sr, The infrared and Raman spectra of β-and α-tricalcium phosphate (Ca3 (PO4) 2), Spectrosc. Lett. 31 (1998) 1619–1634.
[29] A. Ślósarczyk, C. Paluszkiewicz, M. Gawlicki, Z. Paszkiewicz, The FTIR spectroscopy and QXRD studies of calcium phosphate based materials produced from the powder precursors with different CaP ratios, Ceram. Int. 23 (1997) 297–304.
[30] H. Aguiar, J. Serra, P. González, B. León, Structural study of sol-gel silicate glasses by IR and Raman spectroscopies, J. Non-Cryst. Solids 355 (2009) 475–480.
[31] A. Meiszterics, L. Rosta, H. Peterlik, J. Rohonczy, S. Kubuki, P. Henits, K. Sinko, Structural characterization of gel-derived calcium silicate systems, J. Phys. Chem. A 114 (2010) 10403–10411.
[32] F. Ren, Y. Ding, Y. Leng, Infrared spectroscopic characterization of carbonated apatite: a combined experimental and computational study, J. Biomed. Mater. Res. Part A 102 (2014) 496–505.
[33] A. Gozalian, A. Behnamghader, M. Daliri, A. Moshkforoush, Synthesis and thermal behavior of Mg-doped calcium phosphate nanopowders via the sol gel method, Sci. Iran. 18 (2011) 1614–1622.
[34] P. Innocenzi, Infrared spectroscopy of sol-gel derived silica-based films: a spectra-microstructure overview, J. Non-Cryst. Solids 316 (2003) 309–319.

5. ARTÍCULO 2

Ceramics International 43 (2017) 11034–11038

Contents lists available at ScienceDirect

Ceramics International

journal homepage: www.elsevier.com/locate/ceramint

In vitro behaviour of sol-gel interconnected porous scaffolds of doped wollastonite

Patricia Ros-Tárraga[a], Ángel Murciano[b,*], Patricia Mazón[b], Sergio A. Gehrke[c], Piedad N. De Aza[a]

[a] Instituto de Bioingeniería, Universidad Miguel Hernández, Avda. Universidad s/n, 03202 Elche, Alicante, Spain
[b] Universidad Miguel Hernández, Dpto. de Ciencia de Materiales, Óptica y Tec. Electrónica, Avda. Universidad, 3202 Elche, Alicante, Spain
[c] Biotecnos Research Center, Rua Dr. Bonazo nº 57, 1 Santa Maria (RS), 97015-001, Brazil

ARTICLE INFO

Keywords:
Sol-Gel
Hierarchical hydroxyapatite-like
Mechanical Properties
Wollastonite

ABSTRACT

Using the sol-gel method, two different three-dimensional (3D) porous interconnected scaffolds were prepared, whose compositions were MgO-K_2O-CaO-SiO_2 (MgO-K_2O-wollastonite) and Na_2O-K_2O-CaO-SiO_2 (Na_2O-K_2O-wollastonite). Scaffold sintering was performed at 950 °C for 8 h. The scaffolds were obtained and soaked in simulated body fluid for different times (6 h, 3 d, 7 d and 14 d) to study their in vitro behaviour. Scanning electron microscopy and energy-dispersive X-ray spectroscopy revealed the presence of both a hydroxyapatite-like microstructure and a nanostructure on the surface of 3D scaffolds. The presence of Na and K in the scaffolds resulted in the precipitation of a hierarchical hydroxyapatite-like layer composed of nanorods, approximately 200–400 nm in size. The presence of Mg and K ions in the composition caused the precipitation of particles with a nanorod morphology, approximately 50–100 nm in size. The addition of Na, K and Mg, K to the wollastonite resulted in scaffolds with mechanical strengths of 0.03 and 0.02 MPa, respectively.

1. Introduction

Three-dimensional (3D) porous scaffolds have attracted considerable research interest in recent years because of the potential application of these materials in bone-tissue engineering [1–3]. These materials have interconnected pores that satisfy general requirements; e.g., they allow cell migration, as well as nutrient metabolic and waste diffusion. Furthermore, depending on the chemical composition of the scaffold, it is possible to obtain excellent in vitro bioactivity and biocompatibility. Another essential aspect to consider is the cellular response to the surface morphology of the scaffold. The possibility of promoting the adhesion and proliferation of osteoblastic cells by tailoring the surface nanomorphology is well known. The topographic characteristics of scaffolds can modify the cell-migration velocity and enhance the protein adsorption [4]. The influence of the superficial morphology is extended to surface characteristics as small as 10 nm [5]. Thus, it is essential to develop new materials with a controllable nanomorphology whereby the cell and protein behaviour can be modulated.

To develop the 3D scaffold, we used wollastonite ($CaSiO_3$) because considerable research efforts have focused on two-dimensional system in recent decades, and it exhibits excellent in vitro bioactivity, is degradable, and offers good biocompatibility. Therefore, it has the potential to be applied as 3D scaffolds for bone tissue engineering [6–14]. However, $CaSiO_3$ scaffolds have drawbacks that limit their biological applications, including their insufficient strength, brittleness, and high ionic dissolution [15].

To obtain 3D porous scaffolds, different methods are used, including rapid prototyping, electrospinning, gas foaming, freezing-drying polymer sponge replicas, salt leaching, dual-phase mixing, and gel casting [16]. Among these, the polymer sponge replica is one of the most extensively methods used for obtaining ceramic foams. A variation of this method was recently proposed for obtaining 3D porous scaffolds [17].

In this study, we applied the aforementioned method to develop a stratified porous scaffold with wollastonite. The strong point of this method is its capacity to modify the properties of materials by introducing layers of ceramics with different compositions. To explore the behaviour of several materials, the method was applied to wollastonite doped with ions such as K, Mg, and Na; the final developed two-scaffold compositions were MgO-K_2O-CaO-SiO_2 and Na_2O-K_2O-CaO-SiO_2.

2. Experimental section

The composition of the 3D porous scaffolds is given in Table 1. To

* Corresponding author.
E-mail address: angel@dite.umh.es (Á. Murciano).

http://dx.doi.org/10.1016/j.ceramint.2017.05.146
Received 10 February 2017; Received in revised form 15 May 2017; Accepted 20 May 2017
Available online 20 May 2017

Table 1
Compositions (mol%) of the 3D scaffold.

	MgO	Na_2O	K_2O	CaO	SiO_2
MgO-K_2O-CaO-SiO_2	2	0	1	47	50
Na_2O-K_2O-CaO-SiO_2	0	2	1	47	50

obtain the specific composition, $Si(OC_2H_2)$ (tetraethyl orthosilicate TEOS), $CaCO_3$, $MgCO_3$, $K2CO_3$, and $NaHCO_3$ were used as reactants. The sol-gel method started with the hydrolysis of TEOS using HCl (37%). This solution was neutralised with a fraction of $CaCO_3$ to obtain a pH between 2 and 3. A solution with a pH between 2 and 3 was conducted for the other carbonates using HCl (37%) for this purpose. To obtain the specific compositions, the solutions were mixed to obtain a final transparent solution with a pH between 2 and 3. A polyurethane sponge was immersed in the mixture solution and any excess solution was removed by squeezing the sponge. The template covered with the gel was dried for 20 min at 160–180 °C. To increase the mechanical strength of the final ceramic foam, further immersions were performed by depositing a new sol-gel film on the template surface for each immersion. The sample was centrifuged to remove the excess solution. In this study, 10 immersions were performed, but the number of immersions depended on the desired final pore size and the initial pore size of the template. The sol solution composition was always the same; however, depending on the requirements, it can be modified during each immersion to improve the mechanical properties or bioactivity, or to change the cell response to contact with the porous scaffold surface, or to modify the pore size. After the structure was obtained, it was sintered via linear heat treatment up to 950 °C for 55 h and was maintained at that temperature for 8 h. After the thermal treatment, the sample was cooled to room temperature (22 °C) in a furnace.

The porous ceramics were characterised via X-ray diffraction (XRD), by using a Bruker-AXS D8Advance instrument to determine the crystal phases. The microstructural composition was determined via scanning electron microscopy together with energy-dispersive X-ray spectroscopy (SEM-EDX) using a Hitachi S-3500N instrument. The samples were palladium-coated for the EDX analysis.

The mechanical properties of the scaffolds were measured via the Brazilian test, i.e., the Diametrical Compression of Discs Test (DCDT). The Brazilian test is the official method of the International Society for Rock Mechanics for determining the tensile strength of rock materials and is standardised by the American Society for Testing Materials for obtaining the tensile strength of concrete materials. Circular discs with a diameter (D) of 7 mm and thickness (t) of 3 mm were placed between two stainless-steel loading plates with their faces perpendicular to the loading plates in a universal testing machine (model AME-5 kN, Técnica Industrial Oswaldo Filizola Ltda, Guarulhos, Brazil). The load was applied at a 0.5-mm/min displacement rate of the machine until the scaffolds cracked. A pycnometer was used to measure the density of the scaffolds.

Bioactivity tests were performed by immersing the samples with aforementioned dimensions in simulated body fluid (SBF), which was prepared according to the guidelines established by Kokubo [18].

3. Results and discussion

3.1. Sample characterisation

The XRD patterns of both compositions are shown in Fig. 1. The Na_2O-K_2O-CaO-SiO_2 scaffolds were composed of three phases: cristobalite, pseudowollastonite and wollastonite-2M. The MgO-K_2O-CaO-SiO_2 scaffolds were composed of the phases pseudowollastonite and wollastonite-2M. The phases wollastonite-2M and pseudowollastonite were formed by $[SiO_4]$ tetrahedra, yielding simple linear chains with two bridging oxygen atoms per tetrahedron, where the chains were

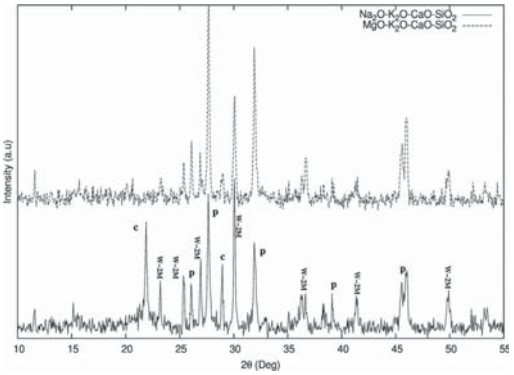

Fig. 1. XRD patterns of scaffolds with compositions of Na_2O-K_2O-CaO-SiO_2 and MgO-K_2O-CaO-SiO_2 (c = cristobalite, p = pseudowollastonite and W-2M = wollastonite 2M).

linked by cations. The cristobalite structure was also formed by $[SiO_4]$ tetrahedra but comprised layers with hexagonal rings. The stability of the cristobalite layer was greater than that of the linear chain of wollastonite polymorphs, as there was less non-bridging oxygen present. Thus, regarding the relationship between the bioactivity and the presence of Si-OH groups, greater bioactivity of the MgO-K_2O-CaO-SiO_2 composition was expected owing the presence of only wollastonite polymorphs, which tended to form more Si-OH groups per atom of non-bridging oxygen.

The geometric characteristics of the scaffold pores are shown in Fig. 2. The samples had well-interconnected porosity, with a pore diameter in the range of 200–400 μm. According to the aforementioned pore size, the sample density was calculated to be 0.25 g/cm^3. These parameters conferred the 3D scaffold with excellent permeation to cells, nutrients, and waste; these requirements should be satisfied by all scaffolds employed in tissular engineering.

A mechanical test was performed, as shown in Fig. 3a. For the disc specimens subjected to diametrical compression, the greatest tensile strength was uniform across the central part of the diametrical plane of the specimens, which were the zones closest to the loading supports in compression. The proportion of compression was smaller for specimens with greater stiffness. Failure occurred along the diametrical plane, and the specimens broke into two similar pieces, corresponding to a load drop in the load–displacement curve recorded during the test. The maximum load before the drop was used to calculate the diametrical strength. Fig. 3b shows the aspect of the specimens which had a valid strength value, after the test. The strength σf was calculated using Eq. (1):

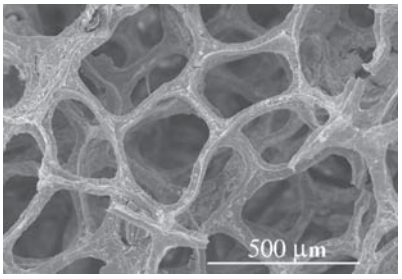

Fig. 2. Low-magnification SEM micrograph of a scaffold with highly interconnected pores.

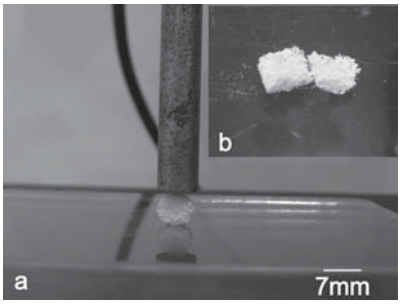

Fig. 3. Mechanical test: (a) the DCDT; (b) aspect of a valid specimen after testing, indicating a straight fracture along the diametral plane.

$$\sigma_f = \frac{2F}{\pi Dt} \quad (1)$$

where F is the compression force, and D and t are the diameter and thickness of the sample, respectively. The results of three valid tests were used to calculate the diametrical strength according to the ISO 14801 procedure. The mechanical-strength values obtained for the scaffolds with compositions of Na_2O-K_2O-CaO-SiO_2 and MgO-K_2O-CaO-SiO_2 were 0.03 and 0.02 MPa, respectively. These values agree with the great mechanical strength of highly porous materials [19].

3.2. In vitro assay test

Fig. 4 shows SEM micrographs of the 3D scaffold with the composition MgO-K_2O-CaO-SiO_2 after it was soaked in SBF for 6 h, 3 d, 7 d and 14 d. For this composition, the first apatite-like precipitate was observed at 6 h and comprised spherical smooth-surface particles approximately 1 μm in size (Fig. 4a). The coalescence of these spherical particles created a hydroxyapatite-like layer after 3 d of soaking in SBF (Fig. 4b). When the soaking time was between 7 and 14 d, the surface of the scaffold was covered by a thicker layer, as shown in Fig. 4b and c. A magnified view of the particles that constituted the layer is shown in Fig. 5a, which reveals that the particle surface was rough and composed of many other particles that had a nanorod morphology and were 50–100 nm in size. The SEM image in Fig. 5b shows how the growth and coalescence of these particles formed a hierarchical microspherical layer. Further precipitation of spherical particles on top of the previous layer resulted in stratified, interconnected apatite-like layers.

The response of the scaffolds with the composition of Na_2O-K_2O-CaO-SiO_2 after being immersed in SBF is shown in Fig. 6. The first hydroxyapatite-like precipitate was obtained after the scaffold had been soaked in SBF for 3 d. Thus, the bioactivity of this composition drastically decreased compared with the previous composition, where the first precipitate was obtained after 6 h of immersion. Furthermore, given the precipitation kinetics, clear differences were observed in the geometries of the obtained particles. As shown in Fig. 6a, the first particles obtained were not smooth spheres as indicated by the above formulation but were clearly composed of a few nanorods (Fig. 6b), which led to particles with a roughly spherical shape. The nanorod size for this composition was approximately 200–400 nm. This larger nanorod size meant that the hole in the spherical microparticles was significantly larger than that in the previous composition. As with the aforementioned formulation, the surface of the scaffold was covered by a hydroxyapatite-like layer through the coalescence of microparticles. In this case, as shown in Fig. 6c, the hydroxyapatite-like layer contained many holes owing to the geometrical characteristics of the microparticles. Further microsphere precipitation on the previous layer made the layer thicker after a long soaking time of 14 d (Fig. 6c).

Fig. 7 shows the SEM – EDX analysis results for Si, P, and Ca in the aforementioned scaffold with respect to the amount of time for which they were immersed in SBF. The elements Si, P, and Ca exhibited the same behaviour for the two compositions: a reduced Si concentration, while the amount of P and Ca increased on the surface of the scaffold. As previously described, the superficial modification process was delayed for the composition Na_2O-K_2O-CaO-SiO_2, where the first hydroxyapatite-like precipitate was obtained at 72 h; it was obtained at 6 h for MgO-K_2O-CaO-SiO_2. Furthermore, the slope of the change was greater for the scaffold whose composition contained Mg. Therefore, the principal difference between the compositions was presence of Na or Mg. The presence of Na in the composition delayed the hydroxyapatite-like precipitation process and, more importantly, changed the microstructure and nanostructure of the precipitate by

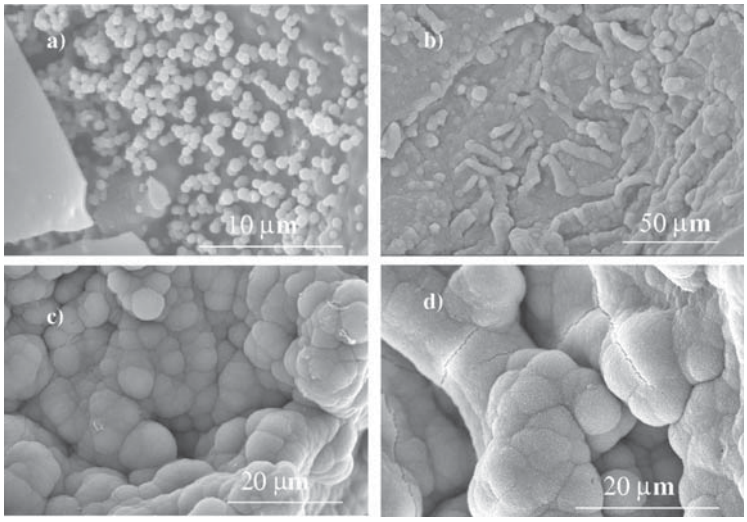

Fig. 4. SEM micrographs of the scaffold with the composition MgO-K_2O-CaO-SiO_2 soaked in SBF for a) 6 h, b) 3 d, c) 7 d, and d) 14 d.

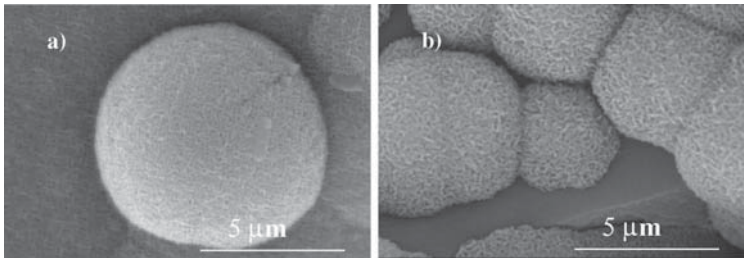

Fig. 5. SEM images of the hierarchical microspheres of the scaffold with the composition of $MgO\text{-}K_2O\text{-}CaO\text{-}SiO_2$: a) microspheres constituted by nanorods; b) coalescence of microspheres and formation of a layer that covered the surface of the scaffold.

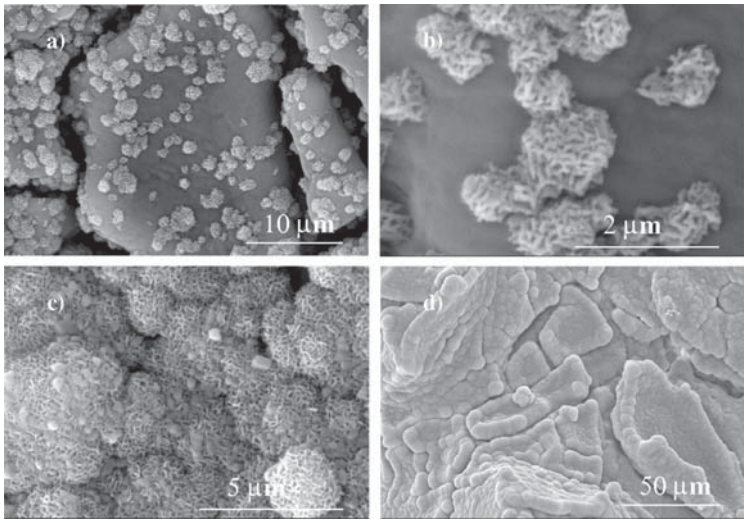

Fig. 6. SEM micrographs of the scaffold with the composition $Na_2O\text{-}K_2O\text{-}CaO\text{-}SiO_2$ soaked in SBF for a) 3 d, b) 7 d, and c) 14 d.

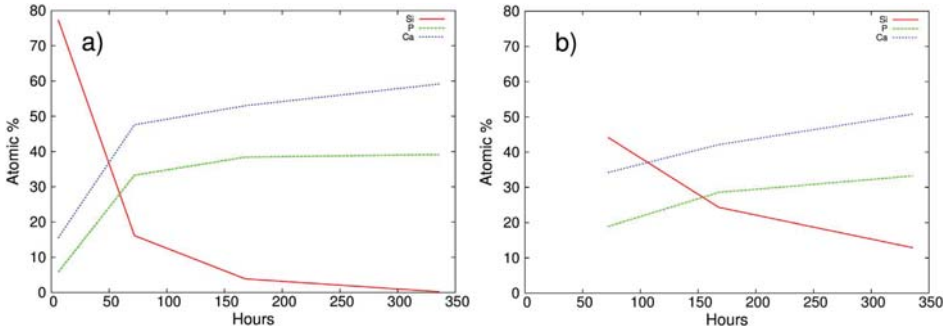

Fig. 7. EDX results showing the evolution of the scaffold components with respect to the amount of time for which they were soaked in SBF: a) $MgO\text{-}K_2O\text{-}CaO\text{-}SiO_2$ and b) $Na_2O\text{-}K_2O\text{-}CaO\text{-}SiO_2$.

modifying the superficial properties of the scaffold and thus altered the interaction of the material with biological systems.

4. Conclusion

We developed two 3D porous interconnected scaffolds with compositions of Na_2O-K_2O-CaO-SiO_2 and MgO-K_2O-CaO-SiO_2. The pore diameter was in the range of 200–400 μm, and the density was 0.25 g/cm3. The scaffold with the composition of MgO-K_2O-CaO-SiO_2 demonstrated high bioactivity, with a response to SBF at 6 h, and formed a microstructure composed of particles with a nanorod morphology, approximately 50–100 nm in size at 3 d. The scaffold with the composition of Na_2O-K_2O-CaO-SiO_2 also exhibited good bioactivity; however, in this case, the first hydroxyapatite-like particles appeared at 3 d. The spherical microparticles were formed by nanorods, where the size for this composition was approximately 200–400 nm. The mechanical strength of the MgO-K_2O-wollastonite was 0.02 MPa and that of the Na_2O-K_2O-wollastonite was 0.03 MPa. These values agree with the high mechanical strength values reported for highly porous materials.

Acknowledgements

The authors acknowledge support from Project MAT2013-48426-C2-2-R of Ministerio De Economía y Competividad of Spain.

References

[1] K. Lin, J. Chang, Y. Zeng, W. Qian, Preparation of macroporous calcium silicate ceramics, Mater. Lett. 58 (2004) 2109–2113.
[2] V. Karageorgiou, D. Kaplan, Porosity of 3D biomaterial scaffolds and osteogenesis, Biomaterials 26 (2005) 5474–5491.
[3] S. Ni, J. Chang, L. Chou, A novel bioactive porous $CaSiO_3$ scaffold for bone tissue engineering, J. Biomed. Mater. Res. Part A 76A (2006) 196–205.
[4] M.S. Lord, M. Foss, F. Besenbacher, Influence of nanoscale surface topography on protein adsorption and cellular response, Nano Today 5 (2010) 66–78.
[5] M. Dalby, M. Riehle, H. Johnstone, S. Affrossman, A. Curtis, Investigating the limits of filopodial sensing: a brief report using SEM to image the interaction between 10 nm high nano-topography and fibroblast filopodia, Cell Biol. Int. 28 (3) (2004) 229–236.
[6] A. Martinez, I. Izquierdo-Barba, M. Vallet-Regi, Bioactivity of a CaO-SiO_2 binary glasses system, Chem. Mater. 12 (2000) 3080–3088.
[7] P. Siriphannon, Y. Kameshima, A. Yasumori, K. Okada, S. Hayashi, Formation of hydroxyapatite on $CaSiO_3$ powders in simulated body fluid, J. Eur. Ceram. Soc. 22 (2002) 511–520.
[8] P.N. De Aza, Z. Luklinska, Effect of glass-ceramic microstructure on its in vitro bioactivity, J. Mater. Sci.-Mater. Med. 14 (2003) 891–898.
[9] C. Sarmento, Z. Luklinska, L. Brown, M. Anseau, P.N. De Aza, S. De Aza, F. Hughes, I. McKay, In vitro behavior of osteoblastic cells cultured in the presence of pseudowollastonite ceramic, J. Biomed. Mater. Res. Part A 69A (2004) 351–358.
[10] K. Lin, W. Zhai, S. Ni, J. Chang, Y. Zeng, W. Qian, Study of the mechanical property and in vitro biocompatibility of $CaSiO_3$ ceramics, Ceram. Int. 31 (2) (2005) 323–326.
[11] L. Long, L. Chen, J. Chang, Low temperature fabrication and characterizations of P-$CaSiO_3$ ceramics, Ceram. Int. 32 (4) (2006) 457–460.
[12] P.N. De Aza, F. Guitian, S. De Aza, F.J. Valle, Analytical control of wollastonite for biomedical applications by use of atomic absorption spectrometry and inductively coupled plasma atomic emission spectrometry, Analyst 123 (1998) 681–685.
[13] R.G. Carrodeguas, A.H. De Aza, P.N. De Aza, C. Baudin, S. De Aza, J.J. Arribas, A. Lopez-Bravo, Assessment of natural and synthetic wollastonite as source for bioceramics preparation, J. Biomed. Mater. Res. Part A 83A (2007) 484–495.
[14] J. Fernandez-Pradas, P. Serra, J. Morenza, P.N. De Aza, Pulsed laser deposition of pseudowollastonite coatings, Biomaterials 23 (2002) 2057–2061.
[15] L. Long, L. Chen, S. Bai, J. Chang, K. Lin, Preparation of dense beta-$CaSiO_3$ ceramic with high mechanical strength and HAp formation ability in simulated body fluid, J. Eur. Ceram. Soc. 26 (9) (2006) 1701–1706.
[16] M. Manzano, M. Vallet-Regi, Revisiting bioceramics: bone regenerative and local drug delivery systems, Progress. Solid State Chem. 40 (2012) 17–30.
[17] I.K. Jun, J.-H. Song, W.-Y. Choi, Y.H. Koh, H.E. Kim, Porous hydroxyapatite scaffolds coated with bioactive apatite-wollastonite glass-ceramics, J. Am. Ceram. Soc. 90 (2007) 2703–2708.
[18] T. Kokubo, H. Takadama, How useful is SBF in predicting in vivo bone bioactivity?, Biomaterials 27 (2006) 2907–2915.
[19] Q. Chen, I. Thompson, A. Boccaccini, 45S5 Bioglass (R)-derived glass-ceramic scaffolds for bone tissue engineering, Biomaterials 27 (2006) 2414–2425.

6. ARTÍCULO 3

Article

Revising the Subsystem Nurse's A-Phase-Silicocarnotite within the System $Ca_3(PO_4)_2$–Ca_2SiO_4

Patricia Ros-Tárraga [1], Patricia Mazón [2], Luis Meseguer-Olmo [3] and Piedad N. De Aza [1,*]

1 Instituto de Bioingenieria, Universidad Miguel Hernandez, Avda. Ferrocarril s/n. Elche, Alicante 03202, Spain; p.ros.tarraga@gmail.com
2 Departamento de Materiales, Óptica y Tecnologia Electrónica, Universidad Miguel Hernández, Avda. Universidad s/n, Elche (Alicante) 03202, Spain; pmazon@umh.es
3 Service of Orthopaedic at Arrixaca University Hospital, UCAM-Catholic University of Murcia, Murcia 30120, Spain; lmeseguer.doc@gmail.com
* Correspondence: piedad@umh.es; Tel.: +34-96-6658485; Fax: +34-96-5222033

Academic Editor: Juergen Stampfl
Received: 18 January 2016; Accepted: 25 April 2016; Published: 28 April 2016

Abstract: The subsystem Nurse's A-phase-silicocarnotite within the system $Ca_3(PO_4)_2$–Ca_2SiO_4 was conducted as a preliminary step toward obtaining new biomaterials with controlled microstructures. Phase composition of the resulting ceramics was studied by X-ray diffraction, differential thermal analysis, and scanning electron microscopy with attached wavelength dispersive spectroscopy. The results showed that the sub-system presents an invariant eutectoid point at 1366 ± 4 °C with a composition of 59.5 wt % $Ca_3(PO_4)_2$ and 40.5 wt % Ca_2SiO_4, and typical eutectoid microstructure of lamellae morphology. These results are in disagreement with the previous reported data, which locate the invariant eutectoid point at 1250 ± 20 °C with a composition of 55 wt % $Ca_3(PO_4)_2$ and 45 wt % Ca_2SiO_4. In addition, cell attachment testing showed that the new eutectoid material supported the mesenchymal stem cell adhesion and spreading, and the cells established close contact with the ceramic after 28 days of culture. These findings indicate that the new ceramic material with eutectoid microstructure of lamellae morphology possesses good bioactivity and biocompatibility and might be a promising bone implant material.

Keywords: phase diagram; bioceramic; biocompatibility; calcium phosphate silicate

1. Introduction

Bioceramics have attracted wide attention due to their cost-effectiveness, easy production, and good biocompatibility. The development of bioceramics has provided promising alternatives to replacing or increasing parts of the skeletal system [1,2]. Therefore, it is significant to develop new type of bioceramics. Compositions belonging to the sub-system Nurse's A-phase-silicocarnotite within the system $Ca_3(PO_4)_2$–Ca_2SiO_4 are promising candidates for preparing ceramic bone implants.

Nurse's A-phase is a solid solution with an approximate composition of $7CaO \cdot P_2O_5 \cdot 2SiO_2$, but should not be confused with the mineral of the same composition identified by Nagelshmidt in 1937 [3]. Nurse's A-phase possess the simple hexagonal crystal lattice of a compound of the type $ABXO_4$ where one-eighth of the cations of the hexagonal structure are not occupied [4,5]. Substances with $ABXO_4$ structure, particularly solid solutions, with unoccupied cation positions are not unusual. It has been pointed out previously [6,7], that such a deviation from the ideal composition of the structural type is not surprising in view of the high temperatures at which such $ABXO_4$ substances are prepared. Nurse's A-phase, from now on referred to as A, which has been recently synthesized at temperatures around 1550 °C in our laboratory [8–10], is a good candidate for biomedical applications [11].

On the other hand, silicocarnotite can be defined as calcium silicophosphate with a carnotite structure. Some authors [12,13] determined that the silicocarnotite structure is very close to hydroxyapatite that has the same weight per unit volume and presents a wide range of CaO, P_2O_5, and SiO_2 solid solutions. Others suggested that the loss of all –OH from HA due to SiO_4 substitution results in a silicocarnotite structure. They considered that silicocarnotite as a mixture of silicon substituted dehydrated apatite and oxyapatite. Ruys [14] found that silicocarnotite can be present as an impurity in HA structures at the lowest SiO_2 content accompanied by increasing amounts of α-TCP and β-TCP in the Ca–Si–P–O amorphous phase. Silicocarnotite ($5CaO\cdot P_2O_5\cdot SiO_2$), from now on referred to as S, is also suitable candidate for biomedical applications. It has been found to be biocompatible and bioactive [15].

The binary system dicalcium silicate (Ca_2SiO_4=C_2S)-tricalcium phosphate ($Ca_3(PO_4)_2$=TCP) was first studied about 128 years ago when silicocarnotite was described as a component of slag [16]. The system was first studied with X-ray diffraction using a high-temperature stage by Nurse *et al*. [17] They identified two intermediate compounds: 2 Ca_2SiO_4–$Ca_3(PO_4)_2$, referred to as Nurse's A-phase and silicocarnotite ($Ca_2SiO_4\cdot Ca_3(PO_4)_2$). Below the liquidus there is a continuous high-temperature solid solution at any given ratio of $Ca_2SiO_4/Ca_3(PO_4)_2$ (Rss=α-C_2S-α-TCP).

The C_2S-TCP system was also studied by Fix *et al*. [18], who include important modifications to the extension of various solid solution fields. Recently, other authors revised the binary system, including modifications to the invariant eutectoid points [19,20].

The exact knowledge of the phase relationships in the subsystem Nurse's A-phase-silicocarnotite is essential for designing materials with controlled chemical, mechanical, and biological properties. In the present work, a correction to the phase equilibrium diagram of the system C_2S-TCP [18] in the sub-system Nurse's A-phase-silicocarnotite is proposed in the light of experimental data. Phase composition of the resulting ceramics was studied by X-ray diffraction (XRD), differential thermal analysis (DTA), and scanning electron microscopy (SEM) with attached wavelength dispersive spectroscopy (WDS). In addition, the bioactivity and biocompatibility of the new eutectoid ceramics were studied in adult mesenchymal stem cells of human origin (hMSCs-A) cultured in experimental conditions for up to 28 days.

2. Results and Discussion

Figure 1 shows the X-ray diffraction patterns of the synthesized powders of A_{ss} and S_{ss}. The obvious sharp peaks and low back grounds suggest that the powders were highly crystalline. The obtained A_{ss} phase shows diffraction peaks that can be assigned to the characteristic reflections of $2Ca_2SiO_4\cdot Ca_3(PO_4)_2$ (JCPDS card number 011-0676). On the other hand, S_{ss} can be assigned to the characteristic reflections of $Ca_2SiO_4\cdot Ca_3(PO_4)_2$, as were described by Dickens and Brown [21]. The only crystalline phase detected in the sample was a well-crystallized silicocarnotite (JCPDS card number 40-393). As the phases are solid solutions, the diffraction peaks are slightly displaced with respect to the corresponding JCPDS card. The results of the chemical analysis of the materials obtained are displayed in Table 1.

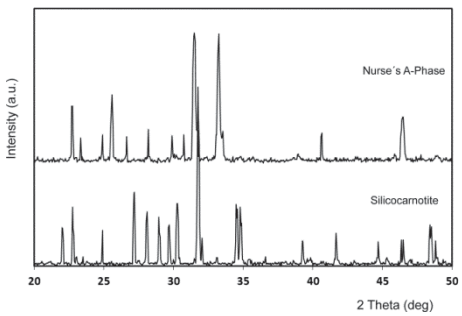

Figure 1. X-ray diffraction patterns of the synthesized materials: Nurse's A-phase and silicocarnotite.

Table 1. Results of the X-ray fluorescence chemical analysis of Nurse's A and silicocarnotite synthetic powders.

Chemical Analysis (wt %)	A_{ss}	S_{ss}
CaO	59.8	57.9
SiO_2	18.3	11.9
P_2O_5	21.5	30
MgO	0.064	0.062
Al_2O_3	0.084	0.066
Na_2O	0.038	0.028
K_2O	0.007	0.005
Fe_2O_3	0.036	0.032
TiO_2	0.024	0.007
MnO	–	–

The results of the differential thermal analysis of A_{ss} and S_{ss} are shown in Figure 2. The A_{ss} phase shows only one endothermic peak during heating at 1392 °C that may be assigned to the polymorphic transformation $A_{ss} \rightarrow R_{ss}$ where R_{ss} phase is a solid solution of α-C_2S-α'TCP. During cooling, an exothermic peak as a results of the $R_{ss} \rightarrow A_{ss}$ transformation was observed at a lower temperature that on heating (1324 °C). S_{ss} showed one endothermic peak during heating at 1422 °C that may be assigned to the polymorphic transformation of $S_{ss} \rightarrow R_{ss}$. During cooling, an exothermic peak as a result of the $R_{ss} \rightarrow S_{ss}$ transformation was observed at a lower temperature than on heating (~1282 °C).

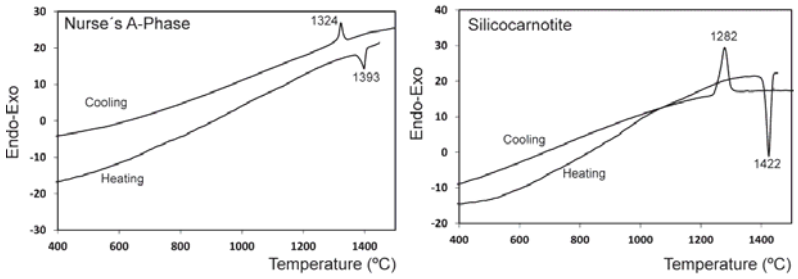

(**a**) (**b**)

Figure 2. DTA of the Nurse's A-phase (**a**) and silicocarnotite materials (**b**).

The experimental results showing the phase coexisting in equilibrium for each composition after the solid state treatment at the selected temperatures and plateau times are summarized in Table 2.

Table 2. Phases identified by XRD for each composition after the heat treatment at the selected temperatures and plateau times. (S_{ss}: silicocarnotite$_{ss}$; A_{ss}: Nurse's A-phase$_{ss}$; R_{ss}: (α-C_2S-α'TCP)$_{ss}$; * Fix *et al*. invariant point.)

Composition No.	Holding Conditions		Observed Phase	General Characteristics
	Temperature (°C)	Time (h)		
1	1300	144	A_{ss}	White solid
	1350	144	A_{ss}	White solid
	1400	144	R_{ss}	White solid
	1500	144	R_{ss}	White solid
2	1225	144	A_{ss}	White solid
	1300	144	A_{ss}	White solid
	1350	144	A_{ss}	White solid
	1375	144	A_{ss}	White solid
3	1225	144	$A_{ss} + S_{ss}$	White solid
	1300	144	$A_{ss} + S_{ss}$	White solid
	1350	144	$A_{ss} + S_{ss}$	White solid
	1375	144	$A_{ss} + R_{ss}$	White solid

Table 2. *Cont.*

Composition No.	Holding Conditions		Observed Phase	General Characteristics
	Temperature (°C)	Time (h)		
4	1225	48	$A_{ss} + S_{ss}$	White solid
	1250	48	$A_{ss} + S_{ss}$	White solid
	1275	48	$A_{ss} + S_{ss}$	White solid
	1300	48	$A_{ss} + S_{ss}$	White solid
	1350	144	$A_{ss} + S_{ss}$	White solid
	1375	144	$A_{ss} + R_{ss}$	White solid
5	1225	48	$A_{ss} + S_{ss}$	White solid
	1250	48	$A_{ss} + S_{ss}$	White solid
	1275	48	$A_{ss} + S_{ss}$	White solid
	1300	48	$A_{ss} + S_{ss}$	White solid
	1350	144	$A_{ss} + S_{ss}$	White solid
	1375	144	$A_{ss} + R_{ss}$	White solid
6 *	1225	48	$A_{ss} + S_{ss}$	White solid
	1250	48	$A_{ss} + S_{ss}$	White solid
	1275	48	$A_{ss} + S_{ss}$	White solid
	1300	48	$A_{ss} + S_{ss}$	White solid
	1350	144	$A_{ss} + S_{ss}$	White solid
	1375	144	$A_{ss} + R_{ss}$	White solid
	1500	144	R_{ss}	White solid
7	1225	48	$A_{ss} + S_{ss}$	White solid
	1250	48	$A_{ss} + S_{ss}$	White solid
	1275	48	$A_{ss} + S_{ss}$	White solid
	1300	48	$A_{ss} + S_{ss}$	White solid
	1350	144	$A_{ss} + S_{ss}$	White solid
	1375	144	$A_{ss} + R_{ss}$	White solid
8	1225	48	$A_{ss} + S_{ss}$	White solid
	1250	48	$A_{ss} + S_{ss}$	White solid
	1275	48	$A_{ss} + S_{ss}$	White solid
	1300	48	$A_{ss} + S_{ss}$	White solid
	1350	144	$A_{ss} + S_{ss}$	White solid
	1375	144	$A_{ss} + R_{ss}$	White solid
9	1362	144	$A_{ss} + S_{ss}$	White solid
	1370	144	$A_{ss} + R_{ss}$	White solid
10	1362	144	$A_{ss} + S_{ss}$	White solid
	1370	144	R_{ss}	White solid
11	1362	144	$A_{ss} + S_{ss}$	White solid
	1370	144	R_{ss}	White solid
	1400	144	R_{ss}	White solid
	1450	144	R_{ss}	White solid
	1500	144	R_{ss}	White solid
12	1362	144	$R_{ss} + S_{ss}$	White solid
	1370	144	$A_{ss} + S_{ss}$	White solid
13	1362	144	$A_{ss} + S_{ss}$	White solid
	1370	144	$A_{ss} + S_{ss}$	White solid
	1400	144	S_{ss}	White solid
14	1225	48	$A_{ss} + S_{ss}$	White solid
	1300	48	$A_{ss} + S_{ss}$	White solid
	1350	144	$A_{ss} + S_{ss}$	White solid
	1375	144	$R_{ss} + S_{ss}$	White solid
15	1225	48	S_{ss}	White solid
	1300	48	S_{ss}	White solid
	1350	144	S_{ss}	White solid
	1375	144	S_{ss}	White solid
16	1300	144	S_{ss}	White solid
	1400	144	S_{ss}	White solid
	1450	144	R_{ss}	White solid
	1500	144	R_{ss}	White solid

The subsystem Nurse's A-phase-silicocarnotite that was plotted from these results is shown in Figure 3. The markings in the diagram near the eutectoid point indicate the compositions tested in this study.

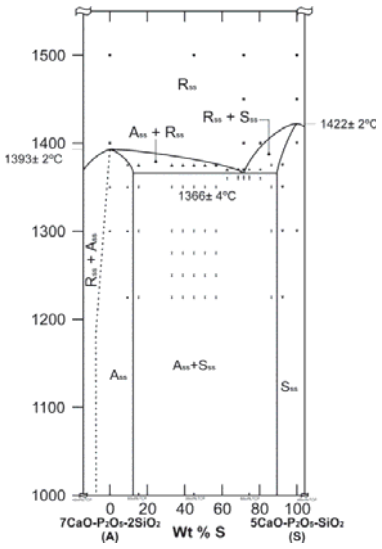

Figure 3. Redrawn of the subsystem Nurse's A-phase-silicocarnotite within the binary system C_2S-TCP. (S_{ss}: silicocarnotite$_{ss}$; Nurse's A: Nurse's A-phase$_{ss}$; R_{ss}: (α-C_2S-α'TCP)$_{ss}$).

In Figure 4, the X-ray patterns of specimens 55 wt % A/45 wt % S and 28.39 wt % A/71.61 wt % S, obtained at various temperatures are shown. In the sample 55 wt % A/45 wt % S (the invariant point of [18]) Nurse's A and silicocarnotite phases was identified in this specimen when quenched after the heat treatment at the Fix *et al*. invariant point (1250 °C for 48 h (Figure 4a)) and above the Fix *et al*. invariant point (1275 °C for 48 h (Figure 4b)). On the other hand, below the new invariant point (Figure 4c) the material presents two phases: Nurse's A and silicocarnotite. Above the new invariant point (Figure 4d) there is only one phase corresponding to the R_{ss} phase, which is a solid solution of α-C_2S-α'TCP.

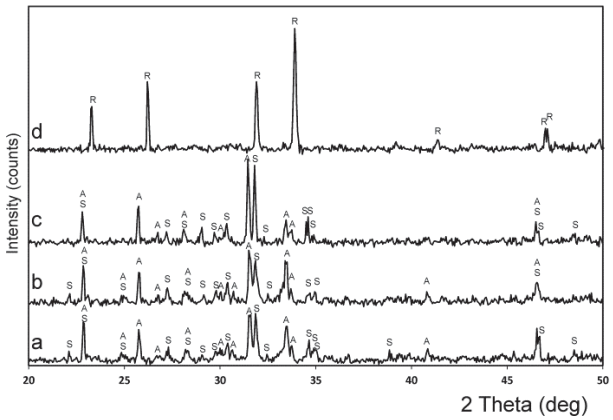

Figure 4. XRD patterns of samples (**a**) 55 wt % A/45 wt % S heated at 1250 °C; (**b**) 55 wt % A/45 wt % S heated at 1275 °C; and (**c**) 28.39 wt % A/71.61 wt % S, heated at 1362 °C; and (**d**) 28.39 wt % A/71.61 wt % S, heated at 1370 °C. (S: silicocarnotite$_{ss}$; A: Nurse's A-phase$_{ss}$; R: (α-C_2S-α'TCP)$_{ss}$).

In Figure 5, the X-ray patterns of several compositions obtained after the heat treatment at 1350 °C are shown. Figure 5a,b present the specimens with 90.48 wt % A/9.52 wt % S, and 84.57 wt % A/15.43 wt % S showing the boundary between the phase field of Nurse's A phase and silicocarnotite + Nurse's A. Figure 5c,d present the specimens with 13.60 wt % A/86.40 wt % S, and 7.69 wt % A/92.31 wt % S showing the boundary between the phase field of silicocarnotite + Nurse's A and silicocarnotite$_{ss}$.

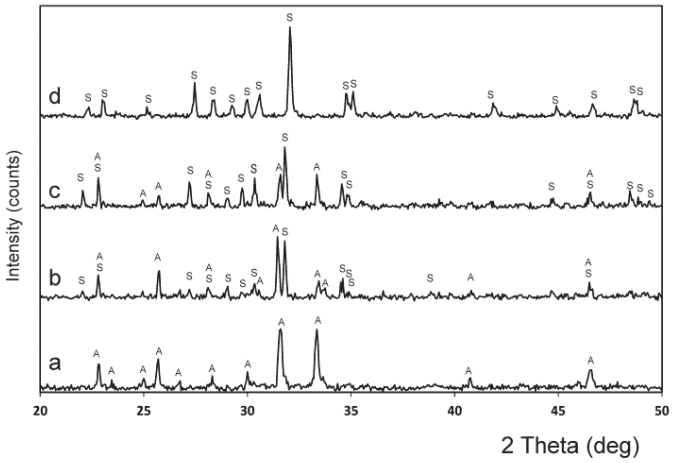

Figure 5. XRD patterns of samples (**a**) 90.48 wt % A/9.52 wt % S; (**b**) 84.57 wt % A/15.43 wt % S; (**c**) 13.60 wt % A/86.40 wt % S; and (**d**) 7.69 wt % A/92.31 wt % S. All of them heated at 1350 °C. (S: silicocarnotite$_{ss}$, A: Nurse's A-phase$_{ss}$; R: (α-C_2S-α'TCP)$_{ss}$).

In the composition range between 100 wt % A and 100 wt % of S, the high-temperature R phase was obtained at room temperature as a metastable phase. The relevant XRD patterns were essentially of the same type as the XRD spectrum that is shown in Figure 4d. They are characterized by two strong diffraction lines whose separation decreases systematically as the solid solution R become richer in C_2S. The *d* values for the six strongest lines of the R phase, recorded from the samples quenched from 1500 °C after 144 h, are given in Table 3 together with the d values of the pure α'-TCP (JCPDS card number 89-8960) and α-C_2S (JCPDS card number 87-1260) for comparison purposes.

Table 3. *d* values for the six strongest lines of the phase R quenched at 1500 °C after 144 h, together with the *d* values of the pure α'-TCP (JCPDS card number 89-8960) and α-C_2S (JCPDS card number 87-1260) for comparison purposes. Compositions are in wt %.

C_2S	TCP	*T* (°C)	Composition No.											
			–		1		6		11		16		–	
			d	I	*d*	I	*d*	I	*d*	I	*d*	I	*d*	I
100	0	1525	–	–	3.99	–	3.99	30	4.00	30	3.98	40	3.98	41
52.61	47.39	1500	3.67	4	–	–	3.77	10	3.80	10	3.81	17	3.85	50
45	55	1500	2.92	61	3.75	74	2.95	80	2.94	100	2.94	100	2.96	100
40.50	59.50	1500	2.77	100	2.75	100	2.72	70	2.72	70	2.70	60	2.68	68
35.70	64.30	1500	2.28	9	2.19	22	2.20	16	2.21	8	2.22	22	2.22	17
0	100	1447	2.01	28	2.00	–	2.00	40	1.99	10	1.95	22	1.99	43

The microstructure corresponding to the sample 55 wt % A/45 wt % S (Fix *et al*. invariant point) [18] is shown in Figure 6. The sample, after homogenization, was heated at 1250 °C, (the Fix *et al*. eutectoid temperature, 1250 ± 20 °C) for 48 h, then cooled at a rate of 6 °C/min to room temperature. The final microstructure was composed of hypoeutectoid Nurse's A grains, plus nucleating on grain

boundaries, the eutectoid phase composed of Nurse's A and silicocarnotite due to the decomposition of the R phase.

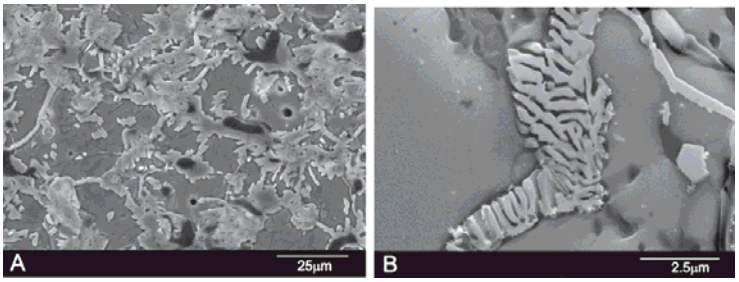

Figure 6. SEM images of sample 55 wt % A/45 wt % S. (**A**) low magnification; (**B**) high magnification.

The microstructure corresponding to the composition 28.39 wt % A/71.61 wt % S, is shown in Figure 7. The sample, after homogenization, was heated at 1350 °C/48 h and slowly cooled to room temperature at a rate of 6 °C/min. Figure 7a,b shows a typical eutectoid composition of lamellae morphology confirming the location of the eutectoid point. The sample was made up of very thin eutectoid platelets constituted of Nurse's A and silicocarnotite phases. The two phases were so intimately mixed and thin that it was impossible to distinguish between Nurse's A and silicocarnotite by WDS.

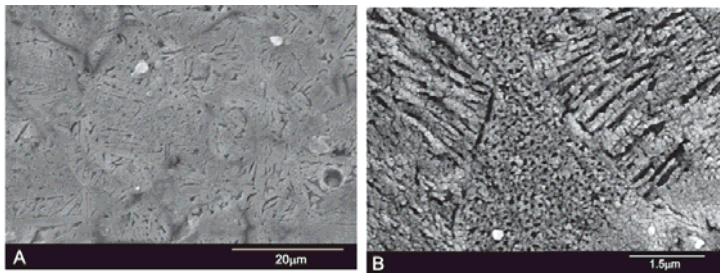

Figure 7. SEM images of sample 28.39 wt % A/71.61 wt % S. (**A**) low magnification; (**B**) high magnification.

These results clearly disagree with those previously published by Fix *et al*. [18], who reported that the system shows an invariant eutectoid point at 1250 ± 20 °C with a composition of 55 wt % Nurse's A and 45 wt % silicocarnotite.

On the other hand, sample 7.69 wt % A/92.31 wt % S at 1350 °C showed a monophasic crystalline microstructure consisting of silicocarnotite$_{ss}$ grains, as shown in Figure 8A. This finding is in good agreement with the XRD results where only the silicocarnotite phase is detected (Figure 5d). Figure 8B shows the polished and etched surface of 90.48 wt % A/9.52 wt % S, at 1350 °C as representative of all compositions in the phase field of Nurse's A. No significant microstructural features were observed except closed elongated pores of ≈25 μm size. This finding is in good agreement with the XRD results where only Nurse's A phase was detected (Figure 5a). WDS confirmed the presence of phosphorous, calcium, and silicon.

The results of the *in vitro* cell tests are shown in Figure 9. The morphology of hMSCs-A adhering and spreading on eutectoid ceramic samples after incubation for 24 h and 28 days is shown in Figure 9A,B. In general, the cells appeared flat and adhered well onto the eutectoid ceramic surfaces in all time intervals. The hMSCs-A undergo their morphological changes to stabilize the cell-material interface of the eutectoid ceramic.

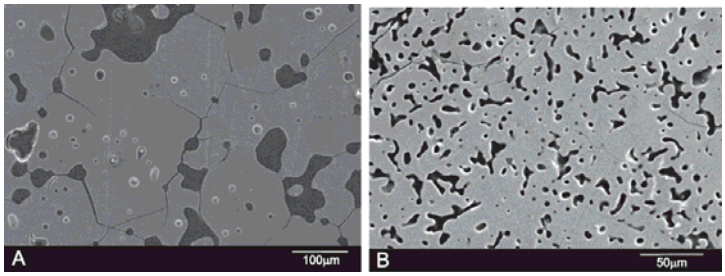

Figure 8. SEM images of sample (**A**) 7.69 wt % A/92.31 wt % S; and (**B**) 90.48 wt % A/9.52 wt % S.

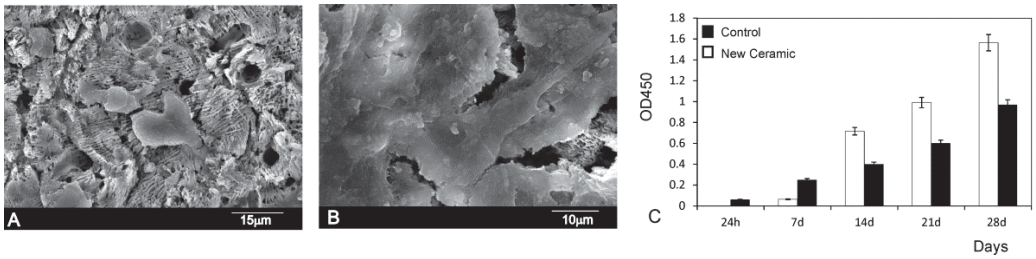

Figure 9. SEM images of the hMSCs-A cultured on eutectoid ceramic surface at (**A**) 24 h; (**B**) 28 days; and (**C**) Proliferation rate of hMSCs-A measured by MTT absorbance at different times of the study.

The adhesion was enhanced by means of multiple cytoplasmic digitations that spread across the surface of the material, increasing the contact area with the surface material. After 24 h of incubation (Figure 9A) the majority of cells cultured on the material exhibited a round morphology. In this period the cells in the eutectoid ceramics studied presented a similar morphology showing some cells adhering either individually or in small groups dispersed across the surface of the material. After 28 days, the density of cultured cells increased in the bioeutectic material with a marked decrease in the intercellular spaces. At this time point, no signs of cytotoxicity (debris, decreased cell size, sloughed cells, *etc*.) were observed. So that the cells spread and presented a close contact with the material, and the philopodia projected progressively (Figure 9B), which indicates that the ceramic supported hMSCs-A adhesion and spreading.

The hMSCs-A viability assay using the MTT assay (Figure 9C) reveals that the cell proliferation gradually increased being that the percentage of cell viability significantly differed from the negative control group ($p < 0.05$). The hMSCs-A viability assay confirmed the SEM observations.

In vitro cell–material interaction is a useful criterion in the evaluation of new biomaterials [22–24]. The present study indicates that ceramic supports hMSCs-A cells proliferation. Cells have been found in close contact with the ceramic. This cell behavior suggests that the surface of the eutectoid material is non-irritant and does not affect the structural integrity of the cell. The cells appeared flat and exhibited an intact, well-defined morphology, with cytoplasmic extensions. The preservation of cytoplasmic extensions is important because they allow a vital three-dimensional network within bone.

3. Materials and Methods

Samples were prepared from Nurse's A and Silicocarnotite ceramics which were used as starting materials. Details of the technique and the characterization of the starting materials can be found in previous publications [8–10,15].

3.1. Chemical Analysis

Chemical analysis of the starting materials was performed in a MagiX Super Q Version 3.0 X-ray fluorescence spectrometer (Philips, Almelo, The Netherlands) provided with an Rh X-ray tube and a power generator of 2.4 kW. Powdered samples weighing 0.3000 g were mixed with 5.5 g of spectral-grade $Li_2B_4O_7$ and melted in a Pt/Au crucible and formed into disks in a special Perl'X3 (Philips) controlled furnace. Calibration curves were prepared from standards of certified compositions of natural and synthetic calcium silicates.

3.2. Phase Diagram Studies

Mixtures with compositions of Table 4 were selected and prepared for studying the subsystem Nurse's A-phase-silicocarnotite. Batches of each composition weighing ~10 g were prepared. Nurse's A and silicocarnotite powders were previously dried at 110 °C overnight. The required amounts of each component were weighed in an analytical balance and homogenized three times in an agate mortar with acetone. The resulting pastes were dried at 60 °C, disaggregated in the agate mortar and isostatically pressed at 200 MPa into bars of ~100 mm in length and ~5 mm in diameter. cylinders, ~6 mm in length, were cut from the bars and loaded into small platinum foil crucibles, and then fired at selected temperatures in a Entech-EEFX/17 (Ängelholm, Sweden) equipped with an electronic programmable temperature controller (JUMO Imago 500, Fulda, Germany). The crucibles were suspended in the hot zone of the electrical furnace by a Pt wire and the hot junction of a calibrated Pt/ 6Rh–Pt/30Rh thermocouple was placed very near the crucibles to guarantee the minimum error in the measurement of the temperature of the specimens ($\pm$2 °C). Specimens were fired at temperatures ranging from 1225 °C to 1500 °C and time varying from 4 to 144 h (six days) to reach equilibrium. After treatment, the samples were liquid-nitrogen quenched. In addition, duplicate sample were heat treated in the same way, but cooled slowly inside the furnace up to the temperatures within 1275–1225 °C range, which is slightly above and below the eutectoid temperature, as reported by Fix *et al*. (1250 $\pm$ 20 °C) [18], and kept at these for 48 h, followed by quenching in liquid nitrogen. The specimens were sometimes reground after quenching and then pressed and fired again to ascertain that the equilibrium had been achieved.

Table 4. Composition of the samples.

Composition No.	Sample wt % TCP	Sample wt % C_2S	Sample wt % S	Sample wt % A
1	47.39	52.61	0.00	100.00
2	49.00	51.00	9.52	90.48
3	50.00	50.00	15.43	84.57
4	53.00	47.00	33.18	66.82
5	54.00	46.00	39.09	60.91
6	55.00	45.00	45.00	55.00
7	56.00	44.00	50.92	49.08
8	57.00	43.00	56.83	43.17
9	58.00	42.00	62.74	37.26
10	59.00	41.00	68.66	31.34
11	59.50	40.50	71.61	28.39
12	60.00	40.00	74.57	25.43
13	61.00	39.00	80.48	19.52
14	62.00	38.00	86.40	13.60
15	63.00	37.00	92.31	7.69
16	64.30	35.70	100.00	0.00

3.3. Thermal Analysis

To evaluate the transition temperatures of the Nurse's A and silicocarnotite, DTA measurements were carried out using a Mettler-Toledo TGA/DTA 851e device (Mettler-Toledo Intl. Inc., Barcelona,

Spain). Measurements were performed on ~25 mg of powder, in a platinum crucible, over the range 25–1550 °C, at a heating rate of 5 °C/min, under nitrogen flux. At 1550 °C, the temperature was held constant for 30 min to equilibrate the samples. DTA results established the temperatures at which the crystalline phases formed and their possible polymorphic transformations.

3.4. XRD

To evaluate the phase's composition, XRD patterns were obtained in a Bruker AXS D8-Advance X-ray Diffractometer (Karksruhe, Germany) using λCuKα1 radiation (0.15418 nm) and a secondary curved graphite monochromator. Diffractograms of samples were compared with the data provided by the Joint Committee on Powder Diffraction Standards (JCPDS) database. JCPDS cards numbered as 011-0676, 40-393, 89-8960, and 87-1260, were used for Nurse's A, silicocarnotite, α′-tricalcium phosphate, and α-dicalcium silicate, respectively.

3.5. Microstructure and Microanalysis

Equilibrated samples were embedded in an epoxy resin under vacuum and progressively polished down to 0.1 μm with diamond paste and etched with acetic acid with a concentration of 0.5% for 2 s. Then, they were gently cleaned in an ultrasonic bath with distilled water, dried, and palladium-coated for scanning electron microscope (SEM-Hitachi S-3500N, Ibaraki, Japan) observations. The chemical composition of crystalline grains was qualitatively determined with a wavelength dispersive spectroscopy (WDS) system coupled to the above-described electron microscope.

3.6. In Vitro Cell Tests

Adult mesenchymal stem cells (hMSCs-A) were isolated from the bone marrow of adult human volunteers obtained through direct aspirations of the iliac crest. The hMSCs-A were seeded in 75 cm^2 flasks at a density of $5 \times 10^3/cm^2$ and were cultured in α-Minimum Essential Medium (α-MEM) supplemented with 10% fetal bovine serum (FBS) and antibiotics penicillin/streptomycin (100 μg/mL and 100 μg/mL, respectively). The cells were cultured at 37 °C in a 5% CO_2 atmosphere and 95% relative humidity, making a change of medium every 3–4 days. When the culture was confluent, the subculture was treated with 0.25% w/v Trypsin-EDTA in sterile phosphate-buffered saline (PBS; pH 7.4) for 5 min. For this study only the hMSCs-A at the third Nurse's A passage were employed. The increment in the number of cells on the materials was evaluated through the reduction of a tetrazolium salts (MTT) assay using the method described previously [25,26] and plastic as a control.

The surface morphology of samples was analyzed by SEM-WDS in order to evaluate the cell growth and adhesion to the ceramics surface. After incubation for 12 h and 7, 15, 21, and 28 days, the samples were removed from the culture well, rinsed with PBS and fixed with 3% glutaraldehyde in 0.1 M cacodylate buffer for 1.5 h at 4 °C. Then, they were rinsed and post-fixed in osmium tetroxide for 1 h, before being dehydrated through increasing concentrations of ethanol (30, 50, 70, and 90 vol %) with final dehydratation in absolute alcohol. After this, they were dried by the critical-point method, palladium-coated, and examined by SEM-WDS.

3.7. Statistical Analysis

Data were analyzed by one-way analysis of variance (ANOVA) followed by Tukey-Kramer multiple comparisons. In both analyses, the minimum acceptable level of significance was $p < 0.05$.

4. Conclusions

The subsystem Nurse's A-phase-silicocarnotite within the C_2S-TCP system presents an invariant eutectoid point at 1366 ± 4 °C for a composition of of 59.50 wt % $Ca_3(PO_4)_2$ and 40.50 wt % Ca_2SiO_4,.

At the temperature of the invariant point the maximum content of solid solution of TCP in Nurse's A is less than ~2.5 wt % and that of C_2S in silicocarnotite is ~5.5 wt %.

In light of the new findings, the composition and processing of ceramic materials belonging to the subsystem Nurse's A-phase-silicocarnotite may be designed with a more exact control of final phase composition, microstructure, and properties. The *in vitro* cell test supports the hypothesis that the eutectoid ceramic obtained displays *in vitro* bioactivity and biocompatibility, which makes it a potential candidate for surgical applications.

Acknowledgments: Part of this work has been supported by Spanish Ministry of Economy and Competitiveness (MINECO) contract grant number: MAT2013-48426-C2-2-R.

Author Contributions: Patricia Ros-Tárraga and Patricia Mazón conducted the phase diagram experiments, Luis Meseguer-Olmo conceived and designed the *in vitro* cells experiments and contributed to the analyses and discussion of the results, Piedad N. De Aza designed and performed the experiments, contributed to the analyses and discussion of the results and prepared the manuscript.

Conflicts of Interest: The authors declare no conflicts of interest.

References

1. Chevalier, J.; Gremillard, L. Ceramics for medical applications: A picture for the next 20 years. *J. Eur. Ceram. Soc.* **2009**, *29*, 1245–1255. [CrossRef]
2. Martinez, I.M.; Velasquez, P.A.; de Aza, P.N. Synthesis and stability of α-tricalcium phosphate doped with dicalcium silicate in the system $Ca_3(PO_4)_2$–Ca_2SiO_4. *Mater. Charact.* **2010**, *61*, 761–767. [CrossRef]
3. Nagelschmidt, G. A new calcium silicophosphate. *J. Chem. Soc.* **1937**, *86*, 5–7.
4. Bredig, M.A. High-temperature crystal chemistry of AmBXn compounds with particular reference to calcium orthosilicate. *J. Phys. Chem.* **1945**, *49*, 537–553. [CrossRef]
5. Bredig, M.A. Isomorphism and allotropy in compounds of the type A_2XO_4. *J. Phys. Chem.* **1942**, *46*, 747–764. [CrossRef]
6. Franck, H.H.; Bredig, M.A.; Franck, R. Untersuchungenüber Kalk-Alkali Phosphate. *Z. Anorg. Allgem. Chem.* **1936**, *230*, 1–27. [CrossRef]
7. Franck, H.H.; Bredig, M.A.; Kanert, E. Untersuchungenüber Kalk-Alkali Phosphate II. *Z. Anorg. Allgem. Chem.* **1938**, *237*, 49–78. [CrossRef]
8. Lugo, G.J.; Mazón, P.; de Aza, P.N. Phase transitions in single phase Si–Ca–P-based ceramic under thermal treatment. *J. Eur. Ceram. Soc.* **2015**, *35*, 3693–3700. [CrossRef]
9. Lugo, G.J.; Mazón, P.; Baudin, C.; de Aza, P.N. Nurse's A phase: Synthesis and characterization in the binary system Ca_2SiO_4–$Ca_3(PO_4)_2$. *J. Am. Ceram. Soc.* **2015**, *98*, 3042–3046. [CrossRef]
10. Lugo, G.J.; Mazón, P.; de Aza, P.N. Material processing of a new calcium silicophosphate ceramic. *Ceram. Int.* **2016**, *42*, 673–680. [CrossRef]
11. De Aza, P.N.; Mate-Sanchez de Val, J.E.; Baudin, C.; Perez Albacete-Martínez, C.; Armijo Salto, A.; Calvo-Guirado, J.L. Bone neoformation of a novel porous resorbable Si–Ca–P base ceramic with osteoconductive properties: Physical and mechanical characterization, histological and histomorphometric study. *Clin. Oral Implant. Res.* **2016**. [CrossRef] [PubMed]
12. Serena, S.; Sainz, M.A.; Caballero, A. Single-phase silicocarnotite synthesis in the subsystem $Ca_3(PO_4)_2$–Ca_2SiO_4. *Ceram. Int.* **2014**, *40*, 8245–8252. [CrossRef]
13. Radev, L.; Hristov, V.; Michailova, I.; Fernandes, M.H.V.; Salvado, I.M.M. Collagen/silicocarnotite composites, cross-linked with chondroitin sulphate: *In vitro* bioactivity. *Process. Appl. Ceram.* **2011**, *5*, 161–170. [CrossRef]
14. Ruys, A.J. Silicon-Doped Hydroxyapatite. *J. Austral. Ceram. Soc.* **1993**, *29*, 71–80.
15. Serena, S.; Caballero, A.; de Aza, P.N.; Sainz, M.A. New evaluation of the *in vitro* response of silicocarnotite monophasic material. *Ceram. Int.* **2015**, *41*, 9411–9419. [CrossRef]
16. Stead, J.E.; Ridsdale, C.H. Crystals in basic converter slag. *J. Chem. Soc.* **1987**, *51*, 601–610. [CrossRef]
17. Nurse, R.W.; Welch, J.H.; Gutt, W. High-Temperature Equilibria in the System Dicalcium Silicate-Tricalcium Phosphate. *J. Chem. Soc.* **1959**, *220*, 1077–1083. [CrossRef]
18. Fix, W.; Heymann, H.; Heinke, R. Subsolidus relations in the system $2CaO{\cdot}SiO_2$–$3CaO{\cdot}P_2O_5$. *J. Am. Ceram. Soc.* **1969**, *52*, 346–347. [CrossRef]

19. Rubio, V.; de la Casa-Lillo, M.A.; de Aza, S.; de Aza, P.N. The system $Ca_3(PO_4)_2$–Ca_2SiO_4: The sub-system Ca_2SiO_4–$7CaOP_2O_5 \cdot 2SiO_2$. *J. Am. Ceram.Soc.* **2011**, *94*, 4459–4462. [CrossRef]
20. Martinez, I.M.; Velasquez, P.A.; de Aza, P.N. The sub-system α-TCPss-Silicocarnotite within the binary system $Ca_3(PO_4)_2$–Ca_2SiO_4. *J. Am. Ceram. Soc.* **2012**, *95*, 1112–1117. [CrossRef]
21. Dickens, B.; Brown, W.E. The Crystal Structure of $Ca_5(PO_4) \cdot 2SiO_4$ (Silicocarnotite). *Tschermaks Min. Petr. Mitt.* **1971**, *16*, 1–27. [CrossRef]
22. Paredes, B.; Santana, A.; Arribas, M.I.; Vicente-Salar, N.; de Aza, P.N.; Roche, E.; Such, J.; Reig, J.A. Phenotypic differences during the osteogenic differentiation of single cell-derived clones isolated from human lipoaspirates. *J. Tissue. Eng. Regen. Med.* **2011**, *5*, 589–599. [CrossRef] [PubMed]
23. Meseguer-Olmo, L.; Aznar-Cervantes, S.; Mazón, P.; de Aza, P.N. *In vitro* behaviour of adult mesenchymal stem cells of human bone marrow origin seeded on a novel bioactive ceramics in the Ca_2SiO_4–$Ca_3(PO_4)_2$ system. *J. Mater. Sci. Mater. Med.* **2012**, *23*, 3003–3014. [CrossRef] [PubMed]
24. Martinez, I.M.; Velasquez, P.A.; Meseguer-Olmo, L.; de Aza, P.N. Production and study of *in vitro* behaviour of monolithic α-Tricalcium Phosphate based ceramics in the system $Ca_3(PO_4)_2$–Ca_2SiO_4. *Ceram. Int.* **2011**, *37*, 2527–2535. [CrossRef]
25. Scudiero, D.A.; Shoemaker, R.H.; Paul, K.D.; Monks, A.; Tiemey, S.; Nofziger, T.H.; Currens, M.J.; Seniff, D.; Boyd, M.R. Evaluation of a soluble tetrazolium/formazan assay for cell growth and drug sensitivity in culture using human and other tumor cell lines. *Cancer Res.* **1988**, *48*, 4827–4833. [PubMed]
26. Martinez, I.M.; Velasquez, P.A.; Meseguer-Olmo, L.; Bernabeu-Esclapez, A.; de Aza, P.N. Preparation and characterization of novel bioactive α-Tricalcium Phosphate doped with Dicalcium Silicate ceramics. *Mater. Sci. Eng. C.* **2012**, *32*, 878–886. [CrossRef]

7. ARTÍCULO 4

Article

Assessment of Effects of Si-Ca-P Biphasic Ceramic on the Osteogenic Differentiation of a Population of Multipotent Adult Human Stem Cells

Patricia Ros-Tárraga [1], Rubén Rabadan-Ros [1], Angel Murciano [2], Luis Meseguer-Olmo [3] and Piedad N. De Aza [4,*]

1 Grupo de Investigación en Regeneración y Reparación de Tejidos, UCAM—Universidad Católica San Antonio de Murcia, Guadalupe, 30107 Murcia, Spain; p.ros.tarraga@gmail.com (P.R.-T.); rubenrabadanros@gmail.com (R.R.-R.)
2 Departamento de Materiales, Óptica y Tecnologia Electrónica, Universidad Miguel Hernández, Avda. Universidad s/n, 03202 Elche (Alicante), Spain; amurciano@umh.es
3 Service of Orthopaedic at Arrixaca University Hospital, UCAM—Catholic University of Murcia, 30120 Murcia, Spain; lmeseguer.doc@gmail.com
4 Instituto de Bioingenieria, Universidad Miguel Hernandez, Avda. Ferrocarril s/n. Elche, 03202 Alicante, Spain
* Correspondence: piedad@umh.es; Tel.: +34-96-6658485

Academic Editor: Enrico Bernardo
Received: 12 October 2016; Accepted: 15 November 2016; Published: 29 November 2016

Abstract: A new type of bioceramic with osteogenic properties, suitable for hard tissue regeneration, was synthesised. The ceramic was designed and obtained in the Nurse's A-phase-silicocarnotite subsystem. The selected composition was that corresponding to the eutectoid 28.39 wt % Nurse's A-phase-71.61 wt % silicocarnotite invariant point. We report the effect of Nurse's A-phase-silicocarnotite ceramic on the capacity of multipotent adult human mesenchymal stem cells (ahMSCs) cultured under experimental conditions, known to adhere, proliferate and differentiate into osteoblast lineage cells. The results at long-term culture (28 days) on the material confirmed that the undifferentiated ahMSCs cultured and in contact with the material surface adhered, spread, proliferated, and produced a mineralised extracellular matrix on the studied ceramic, and finally acquired an osteoblastic phenotype. These findings indicate that it underwent an osteoblast differentiation process. All these findings were more significant than when cells were grown on plastic, in the presence and absence of this osteogenic supplement, and were more evident when this supplement was present in the growth medium (GM). The ceramic evaluated herein was bioactive, cytocompatible and capable of promoting the proliferation and differentiation of undifferentiated ahMSCs into osteoblasts, which may be important for bone integration into the clinical setting.

Keywords: bioceramic; calcium silicophosphate; eutectoid; adult human mesenchymal stem cells; cell culture; osteogenic differentiation

1. Introduction

Despite its extraordinary healing ability, bone response may be unsuccessful for repairing the severe damage caused by injuries, tumours, infections and ageing-related problems. The surgical techniques applied for bone reconstruction are based on bone grafting procedures.

Currently, materials available for bone replacement include autologous bone, allograft, xenograft, demineralised bone matrix (DBM), and various synthetic materials such as ceramics Hydroxyapatite (HA), tricalcium phosphate (TCP), composites, polymers, silk-fibroin, etc., and all with the associated complications and drawbacks. Of them all, an autologous cancellous bone graft, is considered a gold

standard because of its osteoconductive, osteoinductive and osteogenic properties, which are necessary for bone repair.

Current technology enables the regeneration of viable tissue or organs by using cultured cells and suitable scaffolds. We previously reported that ahMSCs derived from bone marrow can be cultured on TCP and Si-TCP ceramics [1,2]. Under osteogenic conditions, cultured ahMSCs further differentiate into cells with the osteoblastic phenotype and are able to fabricate an extracellular bone matrix (osteopontin, osteocalcin, bone sialoprotein).

Previous research suggests that silicon, as an essential element in skeletal development. Carlisle [3–5] first reported in the 1970s that silicon was uniquely localized in the active areas of young bone and involved in the early stage of bone calcification. Similar studies by Schwarz and Milne [6] have shown that silicon deficiency in rats resulted in skull deformation, with the cranial bones appearing flatter than normal.

As Si performs a major function in human bone, Si has been widely incorporated into Ca-P bioceramics to enhance their bioactivity [7–10]. Typically, Si-doped HA and Si-TCP ceramics have been prepared, although both pure Ca-P ceramics and Si-doped Ca-P ceramics still have shortcomings. Previous studies have shown that sintered HA does not significantly degrade, but remains a permanent fixture, susceptible to long-term failure [11–13]. Although α and β-TCP ceramics are degradable at a quicker degradation rate than HA, in vivo osteogenesis of sintered α and β-TCP ceramics is far from optimal. Recently, Martinez et al. found that the in vitro weight loss of α-TCP and Si-α-TCP ceramics was 25% and 10% respectively, after 4 weeks of soaking in Kokubo's simulated body fluid [14]. Mate-Sanchez et al. found that Si-TCP grafts exhibited better dimensional stability and increased bone-to-implant contact with a reabsorption rate ~71.5% of α-TCP and ~42.2% of Si-TCP after being implanted in vivo for 60 days [15–17].

Accordingly, materials that contain silicon, calcium and phosphorus are excellent candidates for preparing biomaterials with improved osteogenic properties [18–20]. The synthesis of Nurse's A-phase ($2Ca_2SiO_4{\cdot}Ca_3(PO_4)_2$) and silicocarnotite ($Ca_2SiO_4{\cdot}Ca_3(PO_4)_2$) as monophasic materials, was addressed by the present authors in a previous work [21–24]. On the basis of the Nurse's A-phase-silcocarnotite in the system $Ca_3(PO_4)_2$-Ca_2SiO_4, an invariant eutectoid point at 1366 °C ± 4 °C for a composition of 28.39 wt % Nurse's A-phase-71.61 wt % silicocarnotite, was also established [25]. The microstructure of an invariant eutectoid point is always lamellar, regardless of the phase diagram studied. The other compositions from the phase diagram have a hypo or hyper eutectoid microstructure formed by grains of a single phase within a much finer eutectoid matrix and therefore is not suitable, a priori, to be colonized by cells. There is only one eutectoid composition with lamellar microstructure, so that composition has been studied in this work.

The main goal of this study was to evaluate the initial response of the influence of Si-Ca-P biphasic ceramic with a eutectoid composition to stimulate the osteogenic process of ahMSCs in the presence or absence of an osteogenic supplement in culture media with a view to using the material for bone tissue engineering.

2. Results

2.1. Biphasic Ceramic Characterisation

Figure 1a shows the X-ray diffraction patterns of the synthesised powders of Nurse's A and silicocarnotite as well as the composition 28.39 wt % of Nurse's A-71.61 wt % silicocarnotite, referred to as AS from this point onwards. The sharp peaks and low backgrounds suggested that powders were highly crystalline. The obtained Nurse's A-phase gave diffraction peaks, which can be assigned to the characteristic reflections of $2Ca_2SiO_4{\cdot}Ca_3(PO_4)_2$ (JCPDS card No. 011-0676). Silicocarnotite could be assigned to the characteristic reflections of $Ca_2SiO_4{\cdot}Ca_3(PO_4)_2$, as described by Dickens and Brown [26]. The crystalline phase detected in the sample was a well-crystallised silicocarnotite (JCPDS card No. 40-393). The eutectoid AS ceramic presented a mixture of Nurse's A and silicocarnotite phases.

As the phases were solid-solution, the diffraction peaks were slightly displaced compared to the corresponding JCPDS card. Figure 1b shows a porous and homogeneous microstructure formed by very thin eutectoid platelets made up of Nurse's A and silicocarnotite phases.

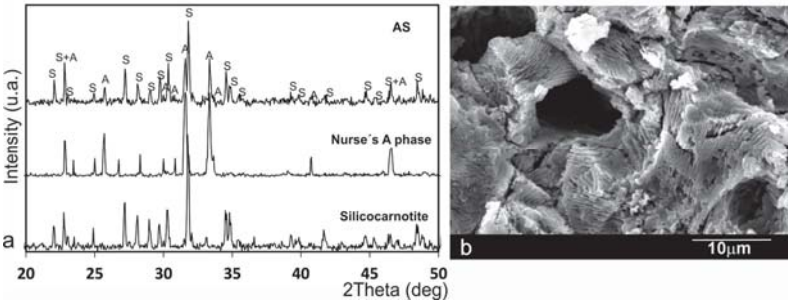

Figure 1. (**a**) X-ray diffraction patterns of the synthesised silicocarnotite and Nurse's A materials and the AS eutectoid ceramic; (**b**) Scanning Electron Microscopy (SEM) image of the biphasic ceramic microstructure with a lamellae morphology.

2.2. Monitoring ahMSCs in Culture

After 3 h of culture in GM, adherent ahMSCs were observed as individual cells larger than non-adherent red blood cells or formed aggregates or colonies, and adopting a rounded or slightly elongated shape (Figure 2a). Residual was unattached around haemopoietic or dead cells that floated in the culture medium on day 7. The cells adopted an elongated and polygonal shape and formed colonies. The number of cells with cytoplasmic vacuoles was not significant, so no cytotoxic effects were observed in morphological terms (Figure 2b).

By 21 days, the culture was more confluent on the cells grown in Osteogenic medium (OM), with a similar morphology to the previous period. On day 28, practically all the adherent ahMSCs displayed a fibroblastic or cuboidal morphology, depending on their confluence (Figure 2c). No significant differences were observed when comparing both culture media. Some birefringent nodules were observed in the cultures with OM.

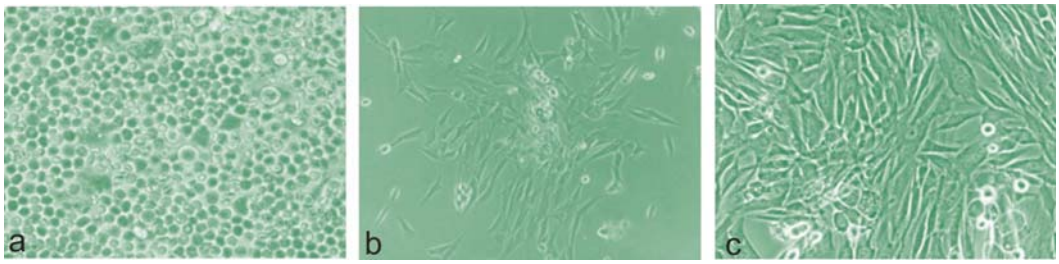

Figure 2. Representative phase contrast micrographs of the evolution of cultured ahMSCs. (**a**) At 3 h; (**b**) 7 days and (**c**) 28 days, adherent ahMSCs practically all displayed a fibroblastic or cuboidal morphology, depending on their confluence (magnification: ×20, ×100 and ×200 respectively).

2.3. Adhesion and Morphology of the ahMSCs Seeded on AS Ceramic Discs

In order to show cell adhesion and morphology on the AS euctectoid ceramic, the ceramic discs cultured with ahMSCs were examined by SEM. Figure 3 representatively shows the most relevant changes observed as a result of the AS-ahMSCs interaction in culture for 24 h, and 7, 14, 21 and 28 days in GM, and for 21 and 28 days in OM.

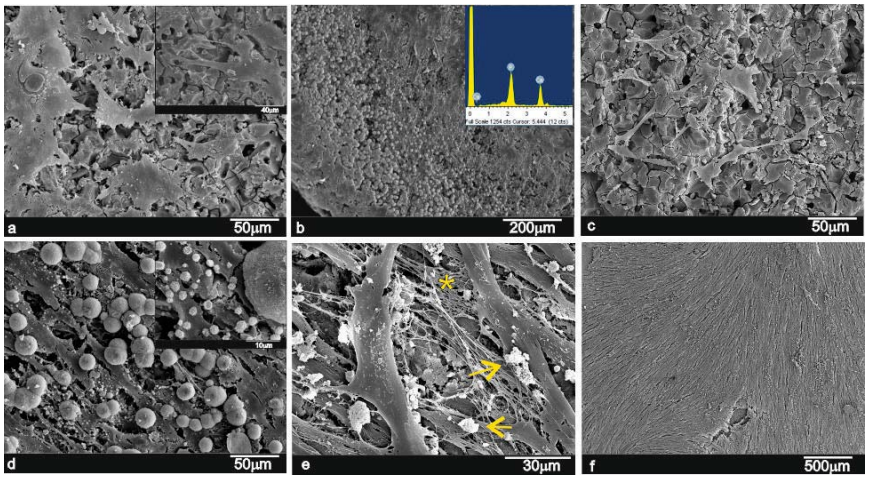

Figure 3. SEM images of the ahMSCs stem cells grown on ceramic surfaces after (**a**,**b**) 24 h; (**c**,**d**) 7 days; (**e**) 21 days and (**f**) 28 days in GM.

During the first 24 h of culture in GM, cells adhered either individually or in small groups across the whole granular surface of the material (Figure 3a). The ceramic exhibited a granular layer that covered some parts of the surface, which is not an obstacle for cell adhesion or proliferation. This layer was composed of a uniform ~1-µm size, and exhibited globular structures with spicules and small nodules, both of which were composed of Ca-P elements according to the Energy Dispersive X-ray elemental microanalysis (Figure 3b and detail).

Later (7 days), the ahMSCs grown on the ceramic surfaces were seen to be polygonal in shape, although some rounded globular cells were still seen (Figure 3c). The cell number grew and was recorded as an increase in cytoplasm prolongations and cell-to-cell interactions. At this time point, the presence of mineralisation nodules suggested cell deposition continuity on AS ceramic surfaces. Granules were seen also above cells, which came into contact with their cellular membrane. This scenario suggests that granules formed simultaneously, and cells proliferated and covered the material surface (Figure 3d and inset). After the 14-day exposure period, the ahMSCs grown on the ceramic surfaces showed the characteristic flat polygonal shape, and no more relevant changes took place compared to the 7-day cultures (figure not shown). After the 21-day exposure period, fast progressive cell growth was observed on surfaces (Figure 3e). Cells formed a monolayer that partially covered the material surfaces (Figure 3e, arrows), and also produced a dense extracellular matrix by way of a fibrillar network that occupied intercellular gaps (Figure 3e, *). After the 28-day period (Figure 3f), the ahMSCs cells began to arrange in a continuous monolayer. The cell monolayer appeared to be almost continuous with the cells that presented a flattened spread morphology, in which it was impossible to recognise single cells, and covered the entire material surface.

Some mineralised nodules were also found on cell surfaces when the culture conditions were in OM. The behaviour of cells at 21 days and 28 days was strikingly similar to that in GM (figures not shown). The material showed good cell development and proliferation.

2.4. Cell Proliferation

The methyl tetrazolium reduction (MTT) cell proliferation assay confirmed the SEM observations, and revealed faster ahMSCs cell proliferation on the AS material from day 14 of the culture study than for the control, which progressed linearly with time from the start of the assay ($p < 0.05$).

Figure 4 shows the cell proliferation on the surfaces of specimens during the culture time in GM and OM. At 24 h, the low absorbance values indicated that a small number of cells initially adhered to the AH ceramic. After 14 days of culture, their proliferation rate overtook that of the control.

From day 14 until the end of the assay, the number of cells that grew on the AS surface was always larger compared to the control. The cell population used as the control progressed linearly with time from the time the assay began. However, the proliferation rate was quite modest, and cell numbers did not duplicate.

Regarding the ahMSCs cultured in OM, and unlike the above-described results, the absorbance values of the cells cultured in OM increased with time, which indicated high cell proliferation in this medium with the assayed ceramics.

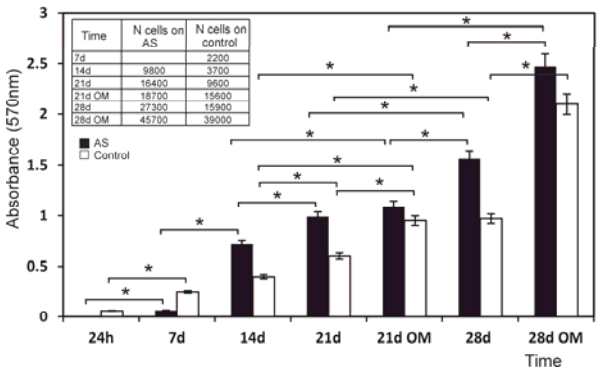

Figure 4. Proliferation of the cells seeded on the AS ceramic compared to plastic, used as the control in the MTT assay. * denotes significance at $p < 0.05$ between these samples.

2.5. Alkaline Phosphatase

Cell differentiation was assessed in terms of the alkaline phosphatase (ALP) activities of ahMSCs on days 14 and 28 of culture in GM and after 28 days of being cultured in OM (Figure 5). At day 14, ALP was expressed at lower levels. No significant differences were detected between the material and the control. After 28 days in GM, the enzyme activity in the control sample was significantly higher than in the AS ceramic. Substitution of GM by OM changed the results. The enzyme activity in the samples incubated with the AS ceramic was greater than that of the cells in the control, and a statistically significant difference was found on day 28.

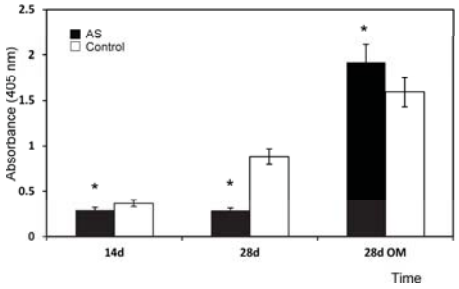

Figure 5. Alkaline Phosphatase quantification of the ahMSCs incubated with the AS biomaterial and for the control (plastic culture) was measured by the p-nitrophenyl phosphate (pNPP) assay after 14 and 28 days in GM and after 28 days in OM. * on the column denotes significance $p < 0.05$, for the ANOVA test.

2.6. Alizarin Red Staining and Activity Analysis

The Alizarin Red expression of the ahMSCs cultured on plastic and AS eutectoid discs in both the growth and osteogenic media was examined. As shown in Figure 6a–d, Alizarin Red staining was more intense for the ahMSCs on the AS eutectoid discs than those on plastic in both GM and OM on

day 28. Modest red staining was identified in GM, which suggests that calcium crystal deposition in the ceramic had commenced. The control monolayers incubated with GM showed no staining (Figure 6b). A strong red stain appeared in OM (Figure 6c), compared with GM (Figure 6d), when ahMSCs were cultured on the AS eutectoid discs. Similarly, the quantitative examination data analysis showed that the Alizarin Red activity of the cells cultured on the AS ceramic discs increased with time throughout the assay period, with a higher value in OM and a statistically significant difference on day 28 (Figure 6d).

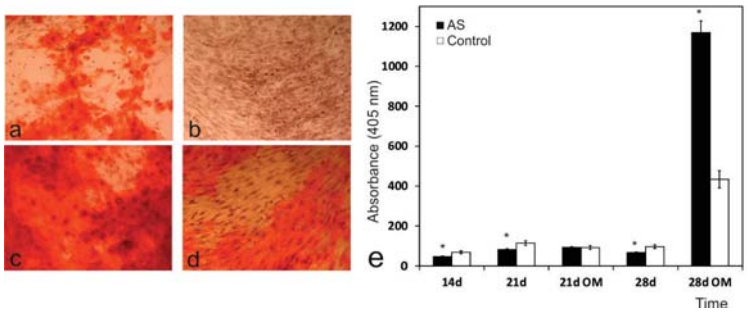

Figure 6. Alizarin Red staining and the activity analysis of the ahMSCs seeded on plastic and the AS ceramic on day 28. The Alizarin Red expression of the ahMSCs seeded on plastic (**a**,**b**) and AS ceramic (**c**,**d**) in either OM (**a**,**c**) or GM (**b**,**d**) (×100). (**e**) The quantitative ALP activity of the ahMSCs seeded on plastic and the AS ceramic was measured on days 14, 21 and 28 in GM and on days 21 and 28 in OM. * indicates significant differences, $p < 0.05$.

2.7. Surface Markers in the Cells Seeded on the AS Ceramic

The ahMSCs of both cultures in the presence of the material and control were negative for all the analysed haematopoietic markers (data not shown). The cluster differentiation (CD) markers, CD105, CD90 and CD73 expressions of the cells seeded on the biomaterial compared to the control are shown in Figure 7. Starting from day 14, the CD105 expression of the cells seeded on the AS ceramic and cultured in GM was always significantly lower than the control, but was comparable during the first 7 days in culture; the CD105 expression lowered with time and was significant at all the time points. When OM was added, the antigen expression became significantly lower than the control. These data demonstrate that the activation of a differentiation programme was accompanied by a lowered expression of the 105 marker characteristic of MSCs.

During the 28-day study, the CD105 marker expression in GM did not significantly change compared to the 21-day period in culture. Possibly, cells retained a minimal level of expression of this marker. The differences between the 21-day period in OM and the 28-day one in OM were not statistically significant. We conclude that CD105 expression did not change after day 21 (Figure 7).

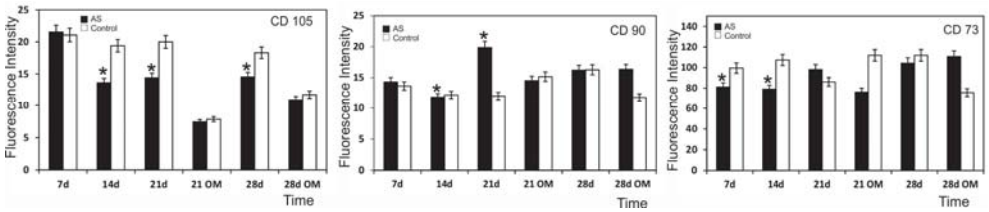

Figure 7. CD105, CD90 and CD73 expressions of the cells seeded on the biomaterial compared to the control. Data represent the fluorescence level. The experiment was performed in triplicate. * denotes a significant difference at $p < 0.05$ between the cells cultivated on the material and the control at the same time.

CD90 expression did not change significantly with either time or addition of OM, although we highlight that its expression was reduced for the material and control samples after 21 days in OM, which was the time point when cells entered the mature phase of the differentiation process (Figure 7). CD73 expression did not significantly change from day 1 to the last day of the study (Figure 7). By 21 days, significant differences were observed between the control and the ceramic material, the control values remained the same, and the values of the samples incubated with the biomaterial increased.

2.8. The Ions Released from the AS Ceramic and Their Effect on ahMSCs

The release of soluble Si, Ca and P elements by dissolution of the ceramics in relation to the immersion time is shown in Figure 8. Initially, the calcium (Ca) concentration significantly increased during the first 12 h of exposure and reached the maximum concentration after 12 days of immersion. After day 12, the Ca concentration dropped to 155 ppm, but the final concentration was still 63.54% higher than the original one. The silicon (Si) concentration increased from the first 3 h and continued to grow until the end of the experiment, which indicated that the AS ceramic was dissolved in the medium. The phosphorus concentration (P) changed slightly for the whole immersion time, which suggests that the consumption rate of P ions due to the Ca-P layer precipitation was similar to the P ion release rate of the ceramics.

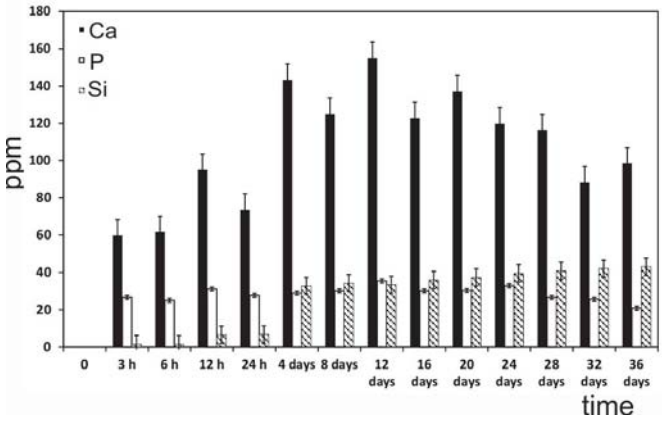

Figure 8. The Si^{4+}, Ca^{++}, $HPO_4^{=}$ concentrations in the ahMSC culture medium after different immersion times.

3. Discussion

For the bone regeneration and bone tissue engineering applications, an ideal biomaterial scaffold designed for bone tissue engineering requires osteoconductive, osteoinductive and osteogenic properties. An optimal biomaterial used as a bone substitute should not only be a temporary scaffold used to support the adhesion, growth, proliferation and differentiation of "seed" cells (such as ahMSCs), but should also be able to degrade over time into non-toxic products, which can be metabolised by physiological mechanisms.

Adding inorganic elements to scaffolds could significantly improve the bioactivity of materials, as previously confirmed in bioglass, glass-ceramic, and bioceramics that contain CaO, SiO_2 and P_2O_5 [27,28]. Given the effect of these silicate-based materials on promoting cell proliferation and osteogenic differentiation, we synthesised in this study a biphasic Si-Ca-P ceramic for the first time. The ceramic obtained herein had a homogeneous porous microstructure with a lamellae morphology of Nurse's A and silicocarnotite phases (Figure 1b).

In the present work, the biological responses to the eutectoid ceramic were studied using ahMSCs, which have been frequently used to elucidate the responses of bone cells to biomaterials [29,30].

The obtained eutectoid had a bioactive surface that displayed the formation of a calcium-phosphate layer after exposure to a human bone marrow culture (Figure 3). This apatite-like layer could play an essential role in the primary chemical bonding of materials for implantations into receptor osseous tissues.

The results obtained for the proliferation and growth of ahMSCs on the eutectoid ceramic proved that after the experiments, cells had homogeneously distributed over the specimens and were well-attached and had uniformly colonised the sample surface. This indicates that the material developed herein is biocompatible, and offers high colonisation and proliferation rates.

The MTT assay demonstrated that the eutectoid ceramic had a limited deleterious effect on cell viability after the first 24 h in culture, possibly because cells had to adapt to the new environment whose ion concentration differed considerably from the normal culture medium. Moreover, cells had to adhere to a new substrate with roughness and stiffness properties, which was different from the culture flask plastic used in previous cultivation steps.

In the proliferation study, the culture control progressed linearly with time, but the proliferation rate was quite modest (the cell number did not double in 1 week). The new eutectoid biomaterial consists of 58.43 wt % of CaO, so a high level of calcium ion is released into the environment until the 12th day (Figure 8). High levels of Ca concentrations (up to 300 mg/L) have proved cytotoxical, but low (2–4 mM) and medium (6–8 mM) Ca concentrations are suitable for proliferation [31]. Low levels of proliferation and spherical cell shape of the first week can be explained due to the increasing release of Ca at the beginning of the experiment. The addition of OM increased this rate by about ~15%–35%, possibly because OM was supplemented with β-glycerophosphate, which is an important source of inorganic phosphate (Pi). In fact, Pi is known as an important signalling molecule for not only cell differentiation, but also for cell proliferation, by regulating the proteins involved in the control of cell cycle and DNA synthesis [32,33].

The MTT results (Figure 4) showed that the biomaterial influenced cell proliferation by stimulating it. In fact, from week 2, the proliferation rate of the cells seeded on the eutectoid ceramic overtook that of the control and remained constant throughout the incubation period. Moreover, this effect increased with the addition of OM, possibly due to the concentration of calcium and phosphate, an ion that the eutectoid ceramic released in the culture medium. They can both stimulate cell proliferation, and this effect was enhanced by the presence of osteogenic medium when an extra Pi source was included. The eutectoid ceramic probably also had a particular surface that favoured cell adhesion, as well as a particular chemical structure that resulted in a combined set of ions released in the culture medium (Figure 8) that induced cell proliferation.

Several studies [34,35] have shown that surface roughness is an important parameter in basic cell biological responses as it improves cell attachment and proliferation. ahMSCs had significantly higher levels of cell attachment on rough sandblasted surfaces and more irregular morphologies than on smooth surfaces. The eutectoid ceramic samples studied herein exhibited a rough surface morphology (see Figure 1b). Thus the material's surface properties can help to promote osteoblast-like cell attachment.

Cell culture does not allow the analysis of possible differences in the response that results from the two distinct phases present in the sample (Nurse's A-phase and silicocarnotite). Under osteogenic conditions, the levels of viable cell adhesion on the crack-free specimen surface were comparable with other apatite surfaces in the osteogenic medium [36,37].

Adhesion and spread of cells on the material surface not only manifest interactions between cells and materials, but also regulate cellular functions, such as proliferation, migration and extracellular matrix production [38,39]. In view of these reasons, ahMSCs were seen to attach to the eutectoid ceramic disc by SEM.

The SEM images of the eutectoid ceramic soaked in GM showed how the ceramic surfaces were covered by small nodules as early as seven post-incubation days, and the SEM-EDX microanalysis confirmed the nodules' nature to be calcium-phosphate precipitates. With this method, we were

able to observe on day 7 that cells continued to adhere to the eutectoid ceramic material surface. Although some cells still looked round and globular, others were polygonal in shape. The cell number grew and an increase in cytoplasmatic prolongations (filopodia) and cell-to-cell interactions was recorded. During this period, presence of mineralisation nodules was also considerable and suggested the continuity of their deposition on the eutectoid ceramic surface. Moreover, granules were seen above the cells that came into contact with their membrane, so granules formed at the same time as cells proliferated and covered the material surface.

Later on day 21, a general increase in the number of cells and interconnections was observed. There were more interconnections between cells; cells began to adopt a fibroblastic-like shape (fusiform) and they covered almost all the material pieces. Intercellular spaces were filled with a fibrillar framework (with no organisation), which corresponded to the extracellular matrix produced by cells. OM also stimulated cell proliferation and not only differentiations as the surface of the pieces in this case were better covered by cells. The SEM data confirmed the data recorded during the MTT, when proliferation was enhanced by addition of OM. Finally on day 28, the eutectoid ceramic pieces were totally covered by cells, and there were no differences between the GM and OM samples. At all the time points, cells adhered to the biomaterials directly and firmly, and also to the neo-formed apatite layer (granules).

At this point, it is important to note that the inductive effect of the eutectoid ceramic on ahMSCs adhesion and proliferation was favoured by the release of Si and Ca ions into the medium (Figure 8), and by the formation of the aforementioned Ca-P layer (Figure 3). The processes of osteoblastic proliferation and differentiation are not only time-dependent, but also regulated by various switches including extracellular matrix (ECM) maturation and hormonal or mechanical stimuli [40]. Extracellular Ca plays an important role in the regulation of osteoblastic proliferation and differentiation by changing the expression of specific Ca channel isoforms on osteoblasts, and has been accepted as a coupling factor between osteoclasts and osteoblasts [41]. In addition, the Ca/P ratio obtained after 14 days in GM medium for the eutectoid material is superior to the ion release of standard materials such as HA and TCP, as well as silicon doped materials as shown in Table 1. This is mainly because the Ca/P ratio of the raw AS material is much higher than those standard ratios, but never reaches the cytotoxic levels after the in vitro assay [31].

Table 1. Ca/P ratio in the AS material as well as some calcium phosphate (CaP) and Si doped CaP materials.

Ca/P Ratios	**Raw Materials**				
	AS	TCP	HA	Si-TCP [2,42]	Si-HA [43]
Ca/P ratio	6.0	1.5	1.67	1.51/1.53	1.69
	Release after 14 Days in GM Medium				
	AS	TCP [2,42]	HA [43]	Si-TCP [2,42]	Si-HA [43]
Ca/P ratio	4.22	1.09	0.32	0.93/0.87	0.47

Mineral crystal deposition was also studied by Alizarin Red staining. During the 14- and 28-day incubations with the biomaterials and the GM medium, only a few small spots spread over the monolayer. Strong mineralisation occurred during the 28-day incubation, when cells were incubated with the eutectoid ceramic and the OM medium, and displayed significant differences compared to the control samples (Figure 6). Mineralisation took place in the samples incubated with the eutectoid ceramic due to the deposition of an enriched extracellular matrix in the mineral-nucleating proteins, which was able to organise and direct calcium phosphate along the collagen fibre precipitates, most of which derived from the biomaterial dissolution products and osteogenic supplements. Quantification was roughly confirmed by the qualitative analysis. ALP activity in the samples incubated with the AS ceramic on day 28 was greater than enzyme activity in the control cells. Recent studies indicate that silicon promotes cell proliferation, ALP expression and mineralization [43,44].

Mineralization begins with hydroxyapatite formation in the matrix vesicles budding from osteoblasts. Hydroxyapatite is formed from Ca incorporated by the annexin calcium channel and from inorganic phosphate Pi [45]. In this chase, the Ca releasing rate is obviously high from AS ceramic. Moreover, the biomaterial is constantly providing phosphorus ions to the medium since day 4 (Figure 8), benefiting the formation of mineralized nodules before alkaline phosphatase is active.

The cell surface markers analysis showed that the cells which had seeded on the eutectoid ceramic present had a reduced expression of CD 105, a marker expressed in ahMSCs whose drop in expression is considered a sign of differentiation programme activation (Figure 7). We highlight that the CD 90 marker expression was reduced for the material and control samples by day 21 in the presence of OM. There could be several factors behind the expression of the osteoblastic markers noted in the control samples. First of all, the chosen population could be constituted by many cells already compromised or contaminated by other cell types. In fact, samples of marrow extruded from bone can include osteoblast precursors eluted from either trabecular bone or the inner surface of the bone itself. Even culture conditions can influence the spontaneous differentiation of ahMSCs. DMEM contains Phenol Red as a pH indicator, which is able to mimic estrogens, potent inducers of osteoblast differentiation. Moreover, the content of Fetal bovine serum (FBS) growth factors preferentially induces ahMSC differentiation towards the osteogenic lineage instead of towards the chondrogenic or adipogenic lineage. These observations highlight the need to better characterise the cells used and to improve the culture conditions in order to verify normal differentiation programme induction when cells remain in culture for a long period and reach confluence.

4. Materials and Methods

4.1. Biphasic Ceramic Preparation and Characterisation

Samples were prepared from Nurse's A and silicocarnotite powders, which were used as starting materials. Details of the technique and characterisation of the starting materials can be found in previous publications [21–24].

A mixture of 28.39 wt % Nurse's A-71.61 wt % silicocarnotite was prepared. Firstly, Nurse's A and silicocarnotite powders were ground to an average particle size of ~20 μm. The desired proportions of each component were weighed on an analytical balance and thoroughly mixed with PSZ (partially stabilized zirconia)-zirconia balls. After drying, samples were isostatically pressed in bars at 200 MPa. The pellets obtained from the bars were placed into small platinum foil crucibles, which were suspended from a platinum wire in the hot zone of an electrical furnace with an electronic temperature controller (±1 °C). Pellets were heated to 1550 °C for a total time period of 144 h (6 days), with quenching in liquid-nitrogen, milling, pressing and reheating every 24 h. The ceramic was heated to 1500 °C/24 h and slow-cooled to room temperature at a rate of 6 °C/min. This combined heat treatment procedure was required to ensure that equilibrium conditions were achieved. The heat treatment temperatures were carefully selected by considering the information provided by the Nurse's A-phase-silcocarnotite [25] subsystem that existed in the binary system of $Ca_3(PO_4)_2$-Ca_2SiO_4.

The material was characterised by X-ray diffraction patterns (XRD, AXS D8 Advance, Bruker, Karksruhe, Germany) and compared with the database provided by the Joint Committee on Powder Diffraction Standards (JCPDS). The ceramic's microstructure was studied by Scanning Electron Microscopy (SEM, S-3500N, Hitachi, Ibaraki, Japan) in an Energy Dispersive X-ray Spectrometer. The final samples were cut from the obtained bars, which had a diameter of 7 mm and a thickness of 3 mm.

4.2. Bone Marrow-Derived ahMSCs Isolation, Culture and Subculture

Undifferentiated multipotent ahMSCs were isolated from the heparinised bone marrow collected from three healthy male human volunteers (50 mL/patient), who underwent elective surgical procedures by percutaneous direct aspiration from the iliac crest. All the procedures were approved

by the Institutional Ethical and Clinical Trials Committee (V. Arrixaca University Hospital of Murcia). Informed consent was obtained from all the volunteers. Details of the method and technique used to obtain, subculture and characterise cells prior to seeding on the biomaterials can be found in previous publications [46]. Cells from the third pass (P3) were used in all assays.

4.3. Phase Contrast Optical Microscopic Observations

To control the evolution of ahMSCs cultures, the cells isolated and attached to plastic were observed under an inverted phase-contrast light microscope (Nikkon Elipse TS, Tokyo, Japan), and their morphological changes, adhesion properties on plastic (control) and growth under the indirect effect of the tested materials were recorded. For this purpose, cells were seeded at a density of 1.0×10^4 cells/well in 24-well culture plates, and were cultured in GM and OM under the same controlled culture conditions (37 °C, 95% humidified atmosphere and 5% CO_2). Then, the sterile biomaterial samples were placed in the upper chambers of 8-μm pore-size cell culture inserts (BD Bioscience, San José, CA, USA), and were incubated in wells in the presence of ahMSCs for 48 h, and for 7, 15 and 21 days. GM was renewed three times a week. Another seeded culture plate with no material was used as the control.

4.4. Seeding ahMSCs on Biphasic Material

To study the biocompatibility and behaviour of the isolated ahMSCs on Nurse's A-phase-silicocarnotite ceramics, two kinds of cell culture media were used: (i) basal GM, used for cell isolation and expansion, which consists in αMEM supplemented with 10% of heat-inactivated FBS and penicillin/streptomycin (100 $U \cdot mL^{-1}$ and 100 $\mu g \cdot mL^{-1}$, respectively); (ii) osteogenic-inducing medium (OM), which consists in GM with an osteogenic supplement (OS) composed of L-ascorbic acid-2-phosphate (0.2 mM; Sigma, St. Louis, MO, USA) dexamethasone (10 nM; Sigma) and β-glycerolphosphate (10 mM; Merck, Darmstadt, Germany).

Initially, ceramic discs were cleaned with pressured air, rinsed several times with PBS (pH 7.4), dried at 37 °C and sterilised at low temperature by gas plasma (Sterrad-100S™, ASP Irvine, Irvine, CA, USA). Discs were pre-wetted in GM for 2 h prior to seeding, and were placed inside the wells of a 96-well culture plate (one disc per well). Then 5.0×10^3 $cell \cdot cm^{-2}$ were gently and statically seeded by pipetting a droplet of 10 μL of the cell suspension on top of each sterilised disc and incubated at 37 °C for 1 h to allow cells to attach to the material's surface. New GM was then carefully added (until 0.2 mL) for further incubations. The control cultures included the cells grown on plastic in the absence of the material. Incubation was carried out under the aforementioned standard conditions (37 °C, 5% CO_2 and 95% humidity). Discs were exposed to GM for 24 h and for 7, 14, 21 and 28 days. Starting on day 21, when cells were calculated to reach confluence, half the samples were changed from GM to OM, and cell behaviour was analysed on days 21 and 28 by a proliferation assay, SEM and osteoblastic phenotype expression, according to the following set-up (Figure 9). All the quantitative assays were carried out in triplicate.

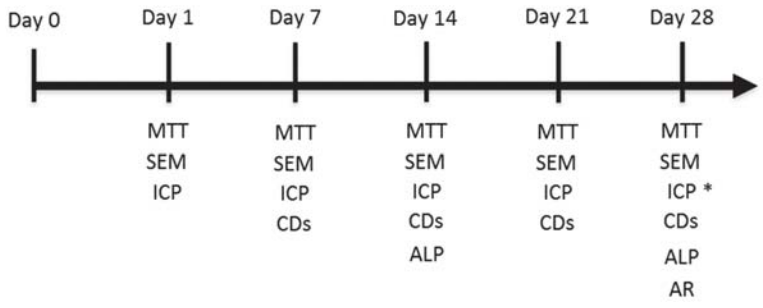

Figure 9. Experimental set-up (* only in GM).

4.5. Morphological Evaluation: Scanning Electron Microscopy

In order to assess cell-material interactions and their continuing effect on the behaviour of ahMSCs, in both cell adherence and growth terms, and from an ultrastructural viewpoint, study periods that lasted 24 h, and 7, 14, 21 and 28 days in GM, and 21 and 28 days in OM, were established for the SEM examinations. Before the cell culture studies, and in order to recognise the seeded ceramic surface, one of the sample faces was carefully impressed with an electrical marker. Specimens were prepared according to previously reported SEM protocols [2,39].

4.6. Proliferation Assay

The increment in cell number on the material's surfaces using both media (GM and OM) was quantified spectrophotometrically by a tetrazolium salt MTT assay. Details on the method and technique can be found in previous publications [46].

4.7. Osteogenic Differentiation Assay

The effect of eutectoid discs on the early osteogenic differentiation of ahMSCs was assessed by ALP specific activity. Next, 5.0×10^3 cell·cm^{-2} were cultured on the discs using GM for 14 and 28 days or OM for 28 days. At the end of this time, cell discs were washed twice with PBS. Alkaline phosphatase (ALP) activity was determined at 405 nm using p-nitrophenylphosphate (pNPP) (Sigma) as the substrate, and total protein contents were measured by the bicinchoninic acid (BCA) protein assay (Pierce, Rockford, IL, USA) using bovine serum albumin (BSA) (Pierce Bovine Serum Albumin) as the standard.

4.8. Calcium Deposition (Mineralisation)

The ability of cells to produce a mineralised matrix and nodules is important for the development of materials for bone regeneration.

Presence of calcium deposition or nodules of mineralisation in cultures was evaluated qualitatively and quantitatively by the selective binding of Alizarin Red S (Osteogenesis kit assay, Millipore, Bredford, MA, USA) to calcium salts on day 28 in both cell media and following the manufacturer's protocol. Briefly, AS ceramic scaffolds were placed in transwell inserts in 24-well plates and ahMSCs were seeded at the bottom of the wells at a density of 5×10^3 cells cm^{-2} and incubated at 37 °C in a humidified atmosphere consisting of 95% air and 7.5% CO_2.

After culturing, scaffolds and inserts were removed and the cells were rinsed three times in phosphate-buffered saline (DPBS), fixed with 8% paraformaldehyde at RT for 15 min, and stained with Alizarin Red Stain solution for 20 min. Stained areas were visualised under an optical microscope and images were acquired. The differentiated cells that contained mineral deposits were stained bright red by Alizarin Red solution.

The quantitative Alizarin Red staining analysis was carried out by determining the absorbance at 405 nm of a set of known Alizarin Red concentrations and comparing these values to those obtained from unknown samples. Briefly, 400 µL of 10% acetic acid were added, after acquiring images, to each 24-well plate well and samples were incubated for 30 min with shaking. The monolayer was gently detached and transferred with acetic acid solution to a 1.5 mL microcentrifuge tube and vigorously mixed (Vortex) for 30 s. Samples were sealed with parafilm to avoid evaporation and were heated to 85 °C for 10 min by placing them in a heat bath. Tubes were then transferred to ice for 5 min. Centrifugation at 20,000× g for 15 min allowed calcium deposit recovery. While centrifuging, Alizarin Red standards were prepared following the manufacturer's protocol. After one centrifugation step, 400 µL of the supernatant of each sample was withdrawn and transferred to a new 1.5 mL microcentrifuge tube. pH was neutralised with 150 µL of 10% ammonium hydroxide. Samples were transferred to a transparent-bottomed 96-well plate and absorbance was red at 405 nm in a plate reader (Multiscan MCC 340, Lab Systems, Vantaa, Finland). The set of Alizarin Red known concentrations was

plotted against their values of absorbance to obtain a standard curve. To determine the concentration of the unknown sample, its absorbance value was plotted to the standard curve.

4.9. Monitoring Surface Markers in the Cells Seeded on the Biphasic Ceramic

A flow cytometry analysis was performed to analyse the expression of representative surface markers CD105, CD90 and CD73 for the ahMSCs seeded on the eutectoid ceramic to be compared with the control after 7, 14, 21 and 28 days of growth in basal GM, and after 21 and 28 days in OM.

Next, 5000 cells·cm^{-2} were seeded on the biomaterials. At the end of every week, cells were trypsinised and processed, then transferred to a 50 mL tube and centrifuged at 1000 rpm for 10 min at 4 °C, and kept on ice during manipulation. Finally, cells were resuspended in a volume of 1% FBS in DPBS to obtain a concentration of 2800 cell·μL^{-1}.

Then, 45 μL of the cell suspension was aliquoted into as many tubes as required. Antibodies were diluted at the recommended (and pre-standardised by our laboratory) dilution in DPBS. Blank: 45 μL of cell suspension and 5 μL of DPBS. Sample: 45 μL of cell suspension and 5 μL of each antibody: 5 μL of CD90-APC (1/100), 5 μL of CD105-FITC (1/10) and 5 μL of CD 73-PE (1/10) (typical MSC markers). Negative control: 45 μL of cell suspension and 5 μL of each antibody: 5 μL of CD45-FITC (1/10) and 5 μL of CD34-PE (1/10) (typical haematopoietic markers). Isotype control: 45 μL of cell suspension and 5 μL of each isotype control: 5 μL of APC-Mouse IgG1k (1/10), 5 μL of PE-Mouse IgG1k (1/10) and 5 μL of FITC-Mouse IgG2ak (1/10). After passing the cleaning solution (Coulter Clenz™, Fisher, IL, USA) in the cytometer, the samples that contained the cells marked with antibodies and blanks were passed in sequence. Data were retrieved with a Beckman Coulter Navios flow cytometer and analysed with the Navios flow cytometry software. All the antibodies were purchased from Becton, Dickinson Co., Franklin Lakes, NJ, USA.

4.10. The Ions Released from the Eutectoid Ceramic

In order to measure the silicon (Si), calcium (Ca) and phosphorous (P) released from the eutectoid ceramics, four discs were added in 1 mL of GM at 37 °C under static conditions to mimic the cell culture conditions. Then, the medium was collected on days 0.5, 1, 4, 7, 14, 21, 28 and 36. The Si, Ca and P concentrations in GM were measured by Inductively Plasma Optical Emission Spectroscopy (ICP-OES, PerkinElmer Optima 2000, Waltham, MA, USA). An analysis of the complete GM was taken as a reference. The instrument's limits of detection (LoD) for the elements of interest were 0.05 for Si, 0.10 for Ca and 0.20 for P/ppm.

4.11. Statistical Analysis

A repeated measures analysis of variance (ANOVA) was run at a level of statistical significance of $p < 0.05$. This was possible because, after applying natural logarithm transformation to the data, they fulfilled the conditions of homoscedasticity and sphericity required for the analysis.

5. Conclusions

By means of the subsystem Nurse's A-phase-silicocarnotite, we designed and processed a material with a chemical composition of the invariant eutectoid point and lamellae morphology.

The results obtained for the proliferation, growth and osteoblastic differentiation of adult human mesenchymal stem cells on the material proved that the biphasic ceramic developed herein is not cytotoxic, cells strongly adhere to the substrate and quickly proliferate on it, and it is capable of initiating the osteogenic differentiation process with both GM and OM.

The essential role of a co-treatment with silicon and calcium as important elements which enhance ahMSCs activity and phosphorous-based biomaterials was highlighted. Additionally, surface roughness is an important parameter in the basic biological responses as it improves cell attachment, proliferation and differentiation of undifferentiated cells.

The biphasic Nurse's A-phase-silicocarnotite ceramic that we produced could serve as a promising platform for hard tissue regeneration through tissue engineering, although in vivo animal implantation could help to determine the final clinical applications.

Acknowledgments: Part of this work has been supported by Spanish Ministry of Economy and Competitiveness (MINECO) contract grant number: MAT2013-48426-C2-2-R.

Author Contributions: Patricia Ros-Tárraga and Ruben Rabadan-Ros performed the ceramic's in vitro cells experiments; Angel Murciano performed the preparation of the ceramics, Luis Meseguer-Olmo together with Piedad N. De Aza, conceived and designed the experiments and prepared the manuscript. All of the authors contributed to the analyses and discussion of the results.

Conflicts of Interest: The authors declare no conflicts of interest.

References

1. Martinez, I.M.; Velasquez, P.A.; Meseguer-Olmo, L.; Bernabeu-Esclapez, A.; De Aza, P.N. Preparation and characterization of novel bioactive α-Tricalcium Phosphate doped with Dicalcium Silicate ceramics. *Mater. Sci. Eng. C* **2012**, *32*, 878–886. [CrossRef]
2. Meseguer-Olmo, L.; Aznar-Cervantes, S.; Mazón, P.; De Aza, P.N. In vitro behaviour of adult mesenchymal stem cells of human bone marrow origin seeded on a novel bioactive ceramics in the Ca_2SiO_4-$Ca_3(PO4)_2$ system. *J. Mater. Sci. Mater. Med.* **2012**, *23*, 3003–3014. [CrossRef] [PubMed]
3. Carlisle, E.M. Silicon: A possible factor in bone calcification. *Science* **1970**, *167*, 279–280. [CrossRef] [PubMed]
4. Carlisle, E.M. Silicon: An essential element for chick. *Science* **1972**, *178*, 619–621. [CrossRef] [PubMed]
5. Carlisle, E.M. A silicon requirement for normal skull formation in chicks. *J. Nutr.* **1980**, *110*, 352–359. [PubMed]
6. Schwarz, K.; Milne, D.B. Growth-promoting effects of silicon in rats. *Nature* **1972**, *239*, 333–334. [CrossRef] [PubMed]
7. Bohner, M. Silicon-substituted calcium phosphates—A critical view. *Biomaterials* **2009**, *30*, 6403–6406. [CrossRef] [PubMed]
8. Reid, J.W.; Tuc, L.K.; Sayer, M.; Fargo, K.; Hendry, J.A. Synthesis and characterization of single-phase silicon-substituted α-tricalcium phosphate. *Biomaterials* **2006**, *27*, 2916–2925. [CrossRef] [PubMed]
9. Sayer, M.; Stratilatov, A.D.; Reid, J.; Calderin, L.; Stott, M.J.; Yin, X.; MacKenzie, M.; Smith, T.J.N.; Hendry, J.A.; Langstaff, S.D. Structure and composition of silicon-stabilized tricalcium phosphate. *Biomaterials* **2003**, *24*, 369–382. [CrossRef]
10. Ning, C.Q.; Mehta, J.; El-Ghannam, A. Effects of silica on the bioactivity of calcium phosphate composites in vitro. *J. Mater. Sci. Mater. Med.* **2005**, *16*, 335–360. [CrossRef] [PubMed]
11. Beltrame, F.; Cancedda, R.; Canesi, B.; Crovace, A.; Mastrogiacomo, M.; Quarto, R.; Scaglione, S.; Valastro, C.; Viti, F. A simple non invasive computerized method for the assessment of bone repair within osteoconductive porous bioceramic grafts. *Biotechnol. Bioeng.* **2005**, *92*, 189–198. [CrossRef] [PubMed]
12. Maté Sánchez de Val, J.E.; Calvo-Guirado, J.L.; Gomez-Moreno, G.; Perez Albacete-Martinez, C.; Mazón, P.; de Aza, P.N. Influence of hydroxyapatite granule size, porosity and crystallinity on tissue reaction in vivo. Part A: Synthesis, characterization of the materials and SEM analysis. *Clin. Oral Implants Res.* **2016**, *27*, 1331–1338. [CrossRef] [PubMed]
13. MatéSánchez de Val, J.E.; Calvo-Guirado, J.L.; Gomez-Moreno, G.; Gherke, S.; Mazón, P.; De Aza, P.N. Influence of hydroxyapatite granule size, porosity and crystallinity on tissue reaction in vivo. Part B: A comparative study with biphasic synthetic biomaterials. *Clin. Oral Implants Res.* **2017**. [CrossRef]
14. Martinez, I.M.; Velasquez, P.A.; Meseguer-Olmo, L.; De Aza, P.N. Production and study of in vitro behaviour of monolithic α-Tricalcium Phosphate based ceramics in the system $Ca_3(PO_4)_2$-Ca_2SiO_4. *Ceram. Int.* **2011**, *37*, 2527–2535. [CrossRef]
15. Mate-Sanchez de Val, J.E.; Calvo-Guirado, J.L.; Delgado-Ruiz, R.A.; Ramirez-Fernandez, M.P.; Negri, B.; Abboud, M.; Martinez, I.M.; De Aza, P.N. Physical properties, mechanical behavior, and electron microscopy study of a new α-tcp block graft with silicon in an animal model. *J. Biomed. Mater. Res. A* **2012**, *100*, 3446–3454. [CrossRef] [PubMed]

16. Mate-Sanchez de Val, J.E.; Calvo-Guirado, J.L.; Delgado-Ruiz, R.A.; Ramirez-Fernandez, M.P.; Martinez, I.M.; Granero-Marin, J.M.; Negri, B.; Chiva-Garcia, F.; Martinez-Gonzalez, J.M.; de Aza, P.N. New block graft of α-TCP with silicon in critical size defects in rabbits: Chemical characterization, histological, histomorphometric and micro-CT study. *Ceram. Int.* **2012**, *38*, 1563–1570. [CrossRef]
17. De Aza, P.N.; Luklinska, Z.B.; Mate-Sanchez de Val, J.E.; Calvo-Guirado, J.L. Biodegradation process of α-tricalcium phosphate and α-tricalcium phosphate solid solution bioceramics in vivo: A comparative study. *Microsc. Microanal.* **2013**, *19*, 1350–1357. [CrossRef] [PubMed]
18. Rabadan-Ros, R.; Velásquez, P.; Meseguer-Olmo, L.; De Aza, P.N. Morphological and structural study of a novel porous Nurse's A ceramic with osteoconductive properties for tissue engineering. *Materials* **2016**, *9*, 474. [CrossRef]
19. Ros-Tarraga, P.; Mazon, P.; Rodriguez, M.A.; Meseguer-Olmo, L.; De Aza, P.N. Novel resorbable and osteoconductive calcium silicophosphate scaffold induced bone formation. *Materials* **2016**, *9*, 785. [CrossRef]
20. De Aza, P.N.; Mate-Sanchez de Val, J.E.; Baudin, C.; Perez Albacete-Martínez, C.; Armijo Salto, A.; Calvo-Guirado, J.L. Bone neoformation of a novel porous resorbable Si-Ca-P base ceramic with osteoconductive properties: Physical and mechanical characterization, histological and histomorphometric study. *Clin. Oral Implants Res.* **2017**, *27*, 1368–1375. [CrossRef] [PubMed]
21. Lugo, G.J.; Mazón, P.; De Aza, P.N. Phase transitions in single phase Si-Ca-P-based ceramic under thermal treatment. *J. Eur. Ceram. Soc.* **2015**, *35*, 3693–3700. [CrossRef]
22. Lugo, G.J.; Mazón, P.; Baudin, C.; De Aza, P.N. Nurse's A phase: Synthesis and characterization in the binary system Ca_2SiO_4-$Ca_3(PO_4)_2$. *J. Am. Ceram. Soc.* **2015**, *98*, 3042–3046. [CrossRef]
23. Lugo, G.J.; Mazón, P.; De Aza, P.N. Material processing of a new calcium silicophosphate ceramic. *Ceram. Int.* **2016**, *42*, 673–680. [CrossRef]
24. Serena, S.; Caballero, A.; De Aza, P.N.; Sainz, M.A. New evaluation of the in vitro response of silicocarnotite monophasic material. *Ceram. Int.* **2015**, *41*, 9411–9419. [CrossRef]
25. Ros-Tarraga, P.; Mazón, P.; Meseguer-Olmo, L.; De Aza, P.N. Revising the subsystem Nurse's A-phase-silicocarnotite within the system $Ca_3(PO_4)_2$-Ca_2SiO_4. *Materials* **2016**, *9*, 322. [CrossRef]
26. Dickens, B.; Brown, W.E. The Crystal Structure of $Ca_5(PO_4)2SiO_4$ (Silicocarnotite). *Tsch. Min. Petr. Mitt.* **1971**, *16*, 1–27. [CrossRef]
27. Taherkhani, S.; Moztarzadeh, F. Influence of strontium on the structure and biological properties of sol-gel-derived mesoporous bioactive glass (MBG) powder. *J. Sol-Gel Sci. Technol.* **2016**, *78*, 539–549. [CrossRef]
28. García-Paez, I.H.; Garcıa Carrodeguas, R.; de Aza, A.H.; Baudin, C.; Pena, P. Effect of Mg and Si co-substitution on microstructure and strength of tricalcium phosphate ceramics. *J. Mech. Behav. Biomed. Mater.* **2014**, *30*, 1–15. [CrossRef] [PubMed]
29. Carrodeguas, R.G.; de Aza, A.H.; Jimenez, J.; de Aza, P.N.; Pena, P.; López-Bravo, A.; de Aza, S. Preparation and in vitro characterization of wollastonite doped tricalcium phosphate bioceramics. *Key Eng. Mater.* **2008**, *361–363*, 237–240. [CrossRef]
30. Paredes, B.; Santana, A.; Arribas, M.I.; Vicente-Salar, N.; de Aza, P.N.; Roche, E.; Such, J.; Reig, J.A. Phenotypic differences during the osteogenic differentiation of single cell-derived clones isolated from human lipoaspirates. *J. Tissue. Eng. Regen. Med.* **2011**, *5*, 589–599. [CrossRef] [PubMed]
31. Valerio, P.; Pereira, M.M.; Goes, A.M.; Leite, M.F. The effect of ionic products from bioactive glass dissolution on osteoblast proliferation and collagen production. *Biomaterials* **2004**, *25*, 2941–2948. [CrossRef] [PubMed]
32. Kanatani, M.; Sugimoto, T.; Kano, J.; Chihara, K. IGF-I mediates the stimulatory effect of high phosphate concentration on osteoblastic cell proliferation. *J. Cell. Physi.* **2002**, *190*, 306–312. [CrossRef] [PubMed]
33. Temenoff, J.S.; Mikos, A.G. *Biomaterials: The Intersection of Biology and Materials Science*; Pearson International Edition: London, UK, 2008; p. 471.
34. Fernandez-Pradas, J.M.; Serra, P.; Morenza, P.J.M.; de Aza, P.N. Pulser laser deposition on pseudowollastonite coatings. *Biomaterials* **2002**, *23*, 2057–2061. [CrossRef]
35. Mazón, P.; García-Bernal, D.; Meseguer-Olmo, L.; Cragnolini, F.; de Aza, P.N. Human mesenchymal stem cell proliferation, differentiation and apoptosis in response to ceramic chemistry and surface roughness. *Ceram. Int.* **2015**, *41*, 6631–6644.

36. Bungo, O.; Mitsuru, T.; Shunsuke, F.; Masashi, N.; Tadashi, K.; Takashi, N. Pore throat size and connectivity determine bone and tissue ingrowth into porous implants: Tree-dimensional micro-CT based structural analyses of porous bioactive titanium implants. *Biomaterials* **2006**, *27*, 5892–5900.
37. Velasquez, P.; Luklinska, Z.B.; Meseguer-Olmo, L.; Mate-Sanchez de Val, J.E.; Delgado-Ruiz, R.A.; Calvo-Guirado, J.L.; Ramirez-Fernandez, M.P.; de Aza, P.N. αTCP ceramic doped with Dicalcium Silicate for bone regeneration applications prepared by powder metallurgy method. In vitro and in vivo studies. *J. Biomed. Mater. Res. A* **2013**, *101*, 1943–1954. [CrossRef] [PubMed]
38. Vassilis, K.; David, K. Porosity of 3D biomaterial scaffolds and osteogenesis. *Biomaterials* **2005**, *26*, 5474–5491.
39. Jarcho, M.; Kay, J.F.; Gumaer, K.I.; Doremus, R.H.; Drobeck, H.P. Tissue, cellular and subcellular events at a bone-ceramic hydroxyapatite interface. *J. Bioeng.* **1977**, *1*, 79–92. [PubMed]
40. Stein, G.S.; Lian, J.B. Molecular mechanisms mediating proliferation/differentiation interrelationships during progressive develop-ment of the osteoblastic phenotype. *Endocr. Rev.* **1993**, *14*, 424–442. [CrossRef] [PubMed]
41. Duncan, R.L.; Akanbi, K.A.; Farach-Carsib, M.C. Calcium signals and calcium channels in osteoblastic cells. *Semin. Nephrol.* **1998**, *18*, 178–190. [PubMed]
42. Martinez, I.M.; Meseguer-Olmo, L.; Bernabeu-Esclapez, A.; Velasquez, P.A.; de Aza, P.N. In vitro behavior of α-Tricalcium Phosphate doped with Dicalcium Silicate in the system Ca_2SiO_4-$Ca_3(PO_4)_2$. *Mater. Charact.* **2012**, *63*, 47–55. [CrossRef]
43. Shie, M.Y.; Ding, S.J.; Chang, H.C. The role of silicon in osteoblast-like cell proliferation and apoptosis. *Acta Biomater.* **2011**, *7*, 2604–2614. [CrossRef] [PubMed]
44. Dong, M.; Jiao, G.; Liu, H.; Wu, W.; Li, S.; Wang, Q.; Xu, D.; Li, X.; Liu, H.; Chen, Y. Biological silicon stimulates collagen type 1 and osteocalcin synthesis in human osteoblast-like cells through the BMP-2/Smad/RUNX2 signaling pathway. *Biol. Trace Elem. Res.* **2016**, *7*, 1–10. [CrossRef] [PubMed]
45. Orimo, H. The mechanism of mineralization and the role of alkaline phosphatase in health and disease. *J. Nippon Med. School* **2010**, *77*, 4–12. [CrossRef]
46. De Aza, P.N.; García-Bernal, D.; Cragnolini, F.; Velasquez, P.; Meseguer-Olmo, L. The effects of Ca_2SiO_4-$Ca_3(PO_4)_2$ ceramics on adult human mesenchymal stem cell viability, adhesion, proliferation, differentiation and function. *Mater. Sci. Eng. C* **2013**, *33*, 4009–4020. [CrossRef] [PubMed]

8. ARTÍCULO 5

Article

Novel Resorbable and Osteoconductive Calcium Silicophosphate Scaffold Induced Bone Formation

Patricia Ros-Tárraga [1], Patricia Mazón [2], Miguel A. Rodríguez [3], Luis Meseguer-Olmo [4] and Piedad N. De Aza [5,*]

1 Grupo de Investigación en Regeneración y Reparación de Tejidos, UCAM—Universidad Católica San Antonio de Murcia, Guadalupe, Murcia 30107, Spain; p.ros.tarraga@gmail.com
2 Departamento de Materiales, Óptica y Tecnologia Electrónica, Universidad Miguel Hernández, Avda. Universidad s/n, Elche, Alicante 03202, Spain; pmazon@umh.es
3 Instituto de Cerámica y Vidrio, ICV-CSIC, C/Kelsen 5, Madrid 28049, Spain; mar@icv.csic.es
4 Service of Orthopaedic at Arrixaca University Hospital, UCAM-Catholic University of Murcia, Murcia 30120, Spain; lmeseguer.doc@gmail.com
5 Instituto de Bioingenieria, Universidad Miguel Hernandez, Avda. Ferrocarril s/n, Elche, Alicante 03202, Spain
* Correspondence: piedad@umh.es; Tel.: +34-96-6658485; Fax: +34-96-5222033

Academic Editor: Jie Zheng
Received: 25 July 2016; Accepted: 12 September 2016; Published: 20 September 2016

Abstract: This aim of this research was to develop a novel ceramic scaffold to evaluate the response of bone after ceramic implantation in New Zealand (NZ) rabbits. Ceramics were prepared by the polymer replication method and inserted into NZ rabbits. Macroporous scaffolds with interconnected round-shaped pores (0.5–1.5 mm = were prepared). The scaffold acted as a physical support where cells with osteoblastic capability were found to migrate, develop processes, and newly immature and mature bone tissue colonized on the surface (initially) and in the material's interior. The new ceramic induced about 62.18% ± 2.28% of new bone and almost complete degradation after six healing months. An elemental analysis showed that the gradual diffusion of Ca and Si ions from scaffolds into newly formed bone formed part of the biomaterial's resorption process. Histological and radiological studies demonstrated that this porous ceramic scaffold showed biocompatibility and excellent osteointegration and osteoinductive capacity, with no interposition of fibrous tissue between the implanted material and the hematopoietic bone marrow interphase, nor any immune response after six months of implantation. No histological changes were observed in the various organs studied (para-aortic lymph nodes, liver, kidney and lung) as a result of degradation products being released.

Keywords: porous bioceramic; calcium silicophosphate; in vivo response; biocompatibility; histology; scanning electron microscopy

1. Introduction

The growing number of bone reconstructive surgery types, along with progressively prolonged life expectancy in developed countries, make research and the development of alternatives to natural bone grafts increasingly important. Bioactive scaffolds play an important role in tissue engineering [1,2].

A bone substitute material should display 'bimodal' behavior, which, in early differentiation stages, allows osteoblasts to build bridges between different sizes of grain and to integrate with other osteoblasts to support both proliferation and differentiation. New bone formation has been stimulated by the activation of mesenchymal stem cells and their absorption onto surfaces with nanoscale topographic features [3]. The ultimate goal is to unite fully differentiated osteoblasts that

support bone matrix production. This requires a porous structure with nanopores, micropores and macropores, all of which are involved in different stages of absorption, adhesion and bone material deposition on and within the bone substitute material [4].

How to effectively improve the attachment of cells in the interior of large-sized scaffolds is still a significant bone tissue engineering challenge. Some studies have suggested that macropores with a pore diameter that falls within the 50–300 μm range are beneficial for cell attachment, proliferation and vascularization, while the micropores within the 0.5–10 μm range are desired to provide the effective delivery of nutrients and physical cues to enhance cell response. It now seems acceptable that a minimum interconnect size of ~100 μm is needed for mineralized tissue ingrowth [1,3,4]. These results underline the need for developing new technologies to produce strong scaffolds with controlled porosity [5,6]. Part of this work focuses on the sintering of porous calcium silicophosphate scaffolds with macro- and microporosity by the polymer replication method.

Regarding silicon that contains calcium phosphate materials, the effect of Si on healthy bone and connective tissues is well-known. Silicon modifies the material properties and improves the biological activity of silicon that contains CaP materials. Thus, they have been widely studied as biomaterial for osseous repair [7,8].

The interest in rich-silico phosphate biomaterial is currently increasing because of its good bioactivity response and low cytotoxicity [9,10].

In this context, the compositions that belong to subsystem Nurse's A-phase- silcocarnotite within system $Ca_3(PO_4)_2$–Ca_2SiO_4 are promising candidates for preparing new ceramic bone implants [11]. Nurse's A-phase is a solid solution with an approximate composition of $7CaOP_2O_52SiO_2$ [12,13], which should not be confused with the mineral of the same composition identified by Nagelshmidt in 1937 [14]. Silicocarnotite ($5CaOP_2O_5SiO_2$) can be defined as calcium silicophosphate with a carnotite structure [7,15].

The main purpose of the present study was to investigate the effect of pore morphology on its in vivo osteoconductivity and resorption process of new calcium silicophosphate ceramic scaffolds obtained by the polymer replication method.

2. Results

2.1. Scaffold Characterization

By the polymer replication method, it was possible to produce highly porous calcium silicophosphate scaffolds with a striking similarity to human cancellous bone tissue (see Figure 1A,D). The SEM observations revealed pore diameters that ranged from 200 μm to 1.0 mm, and a pore wall thickness of ~50 μm (Figure 1B). Micropores from 1 μm to 10 μm were also viewed on pore walls and struts (Figure 1C). The scaffold composition, determined by a quantitative analysis by EDS at different sample points, was around 15.1 wt % SiO_2, 58.2 wt % CaO and 26.6 wt % P_2O_5.

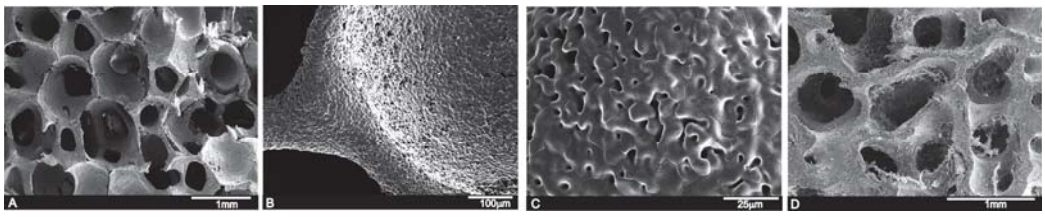

Figure 1. (**A**) SEM view of the calcium silicophosphate scaffolds obtained by the polymer replication method at low magnification, which reveals high porosity and interconnectivity; (**B**,**C**) the high magnification view of the scaffold indicates largely distributed microporosity; and (**D**) human cancellous bone tissue for comparison purposes.

Apparent density was 75 gr·cm^{-3}, which meant total porosity was 76%. Hg porosimetry (Poremaster-60GT, Quantachrome, Boyton Beach, FL, USA) was carried out. It indicated that 15% of pores were bigger than 1 mm, 20% ranged between 1000 and 100 μm, the rest were below 100 μm, and this distribution was centered around 10 μm. The material's mechanical strength was sufficient for handling and placing it inside the surgical site.

2.2. Radiological Study

Radiological density varied for each implantation time. X-ray plains revealed that the scaffold (Figure 2A) gave a rectangular image of great radiopacity with an irregular mottled look and a smooth outline at three months post-implantation. This aspect facilitated the identification of the trabecular bone implant in it. The scaffold showed correct integration and partial resorption.

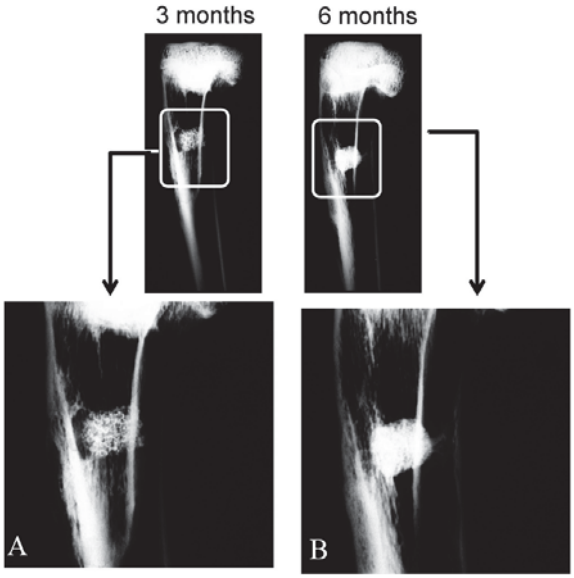

Figure 2. Antero-posterior X-rays of the bone section that contained the implants after three (**A**) and six months (**B**) post-implantation.

Six months after the implantation period (Figure 2B), the material exhibited an irregular rectangular morphology and uneven outlines. It was denser at the material-bone marrow zones interface than the adjacent cancellous bone as a result of new mature bone formation in pores, which correlated with the histological findings. No alterations, loss of their normal distribution pattern in the adjacent bone trabeculae or ectopic bone formation was/observed.

2.3. Histological Evaluation

The histological sections of the materials were analyzed at three months (Figure 3A–G) and six months post-implantation (Figure 3H–N). An analysis of the samples stained with Masson's Trichome and hematoxylin-eosin confirmed the observations made by radiography. All the animals survived the three- and six-month study periods and presented no evidence for inflammation or infection at the implantation sites. Figure 3A shows a panoramic image of the cylinders implanted across the rabbit proximal in the tibia metaphysis at three months post-implantation as being representative of the histological study at three and six months. Rectangles were traced manually to create an individual region of interest (ROI) in the periphery and center of the material. The descriptive histological observations of bone tissue responses are summarized in Table 1.

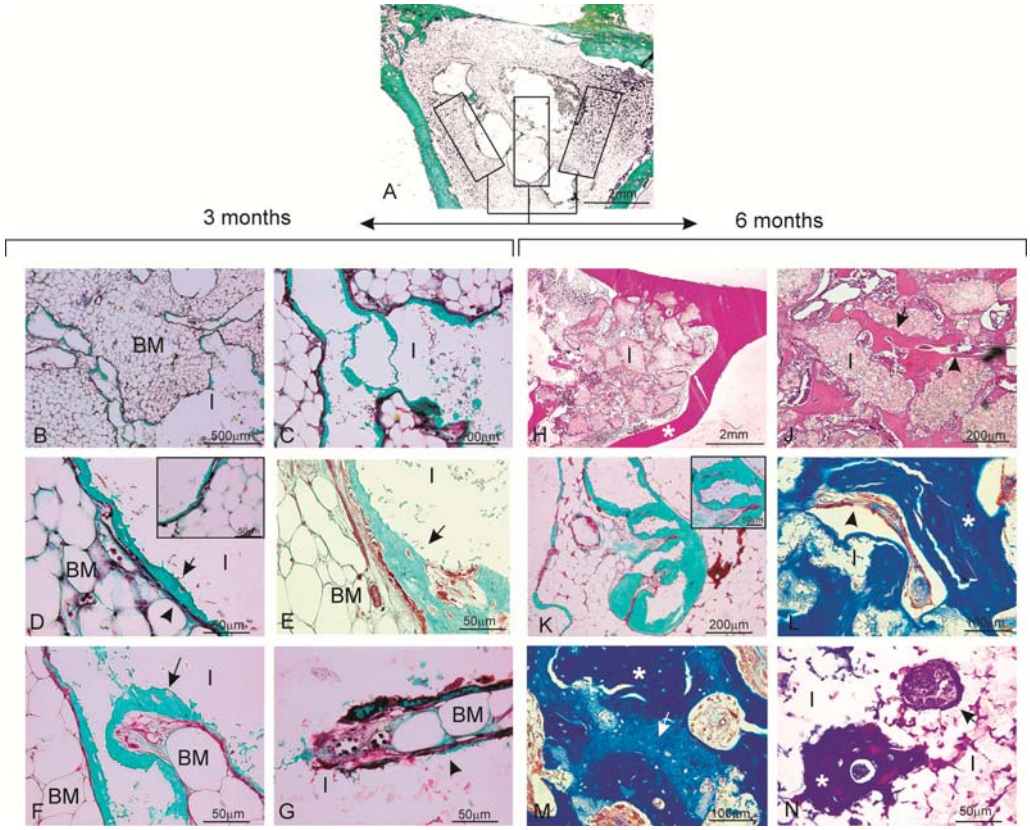

Figure 3. Histological analysis of the material samples stained with Masson's Trichome (**A**–**G**,**K**–**N**) and hematoxylin-eosin (**H**,**J**) three months (**A**–**G**) and six months (**H**–**N**) after implantation. (**A**) panoramic image of the implant section together with the different areas drawn for the descriptive histological study as being representative of the histological study at three and six months. The ceramic implant, which was removed during histological processing, is seen as a blank/empty space; (**B**,**C**) the whole material is observed in close relation with the hematopoietic bone marrow-interior of the pores colonized by hematopoietic bone marrow elements (BM: bone marrow; I: implant); (**D**) blood capillaries located between a thin osteoid tissue layer and surrounding bone marrow material. The insert of the figure shows some areas of the new osteoid tissue with osteocytic lacunae (osteoblast) and with osteocytes inside (BM: bone marrow; I: implant, arrow head: capillary blood; arrow: osteoid); (**E**) image corresponding to the central area of the material with newly formed bone tissue with the trabecular bone characteristic (arrow); (**F,G**) new bone colonization of the implanted material's interior (arrow); (**H**) after six months of implantation, the implanted material is completely enveloped by new bone tissue and penetrates large areas (* cortical bone); (**J**) Presence of bone tissue in both the periphery and interior of the implanted material; (**K**) bone tissue deposition occurred mainly in the form of layers. The insert shows a pore filled with new bone formation; (**L**) bone with normal mature characteristics and in-growth inside one of the implanted material's pores; (**M**) differences in the **blue** staining shade reveals the presence of scattered areas of older bone tissue (**light blue**) (arrow) and newly formed bone (**dark blue**) (*); and (**N**) presence of two nodular structures within the material. Cuboidal osteoblastic cells are seen to line the surface of the developing osteoid tissue (arrow) (BM: bone marrow; I: implant).

Table 1. Relevant histological findings observed by light microscopy at three and six months.

Presence, Location and Quality New Bone Formed		Fibrous Connective Tissue Formation		Inflammatory Cells Infiltration		Foci of Necrosis		Presence of Material Debris and Granulomas		Bone Marrow Changes	
3 m	6 m	3 m	6 m	3 m	6 m	3 m	6 m	3 m	6 m	3 m	6 m
- Periphery - Close contact - Osteoid	- Periphery - Inside - Osteoid - Mature	NO	NO	NO	NO	NO	NO	NO	NO	NO	NO

2.3.1. Three Months

Details of the implant haematopoietic bone marrow interface can be seen at the implant site in Figure 3B. While processing samples, the material was occasionally dragged and left some empty spaces in the histological sections. At a higher magnification (Figure 3C), the colonization process of the scaffold started in the periphery and then penetrated throughout implant porosity.

It is important to highlight the absence of either inflammatory cells or fibrous connective tissue formation in the vicinity of the implanted material and around the newly formed woven bone, which would otherwise imply bone tissue intolerance to the implant (Figure 3D). This fact allowed the arrival of the blood capillaries (arrow head) located between a thin layer of osteoid tissue (arrow) and bone marrow to the surrounding material. Osteoid tissue was formed and detected as a thin layer located directly on the material surface at the implantation site (arrow head). In some osteoid tissue areas, osteocytes lacunae (osteoplast), with osteocytes inside, were viewed (Figure 3D—inset). Presence of poorly inflammatory cells (macrophages and lymphocytes) was observed on the material's edges. No multinucleated giant cells were observed during this period. In other areas, newly formed bone tissue took the trabecular bone characteristic (arrow) in connection with the blood capillaries that delimited bone marrow. These findings can be observed in both the peripheral portions and the material's interior at this time point (Figure 3E).

The presence of thin layers of osteoid with osteoblasts were observed in the implanted material, along with elements of the bone marrow and vascular capillary that invaded the scaffold (Figure 3F). Practically none of the macrophages were observed in the evaluated sections. The fast colonization of the implanted material's interior was also noteworthy. At a higher magnification, Figure 3G shows how a vascular axis penetrated the material, and also the beginning of the bone formation process (arrow head). In the ungrafted specimens (controls), the cortical defect was repaired by newly formed trabecular bone tissue with normal histological characteristics (Figure 4). The increased presence of osseous trabecula was located on the surface that came in contact next to the periosteum layer. No alterations in the bone marrow that occupied the intertrabecular spaces were observed.

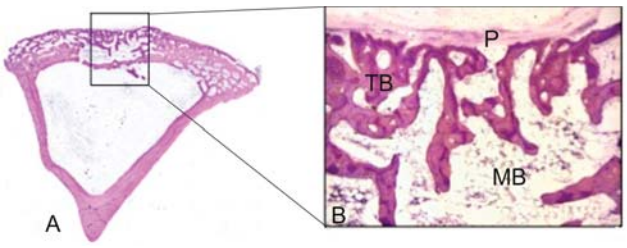

Figure 4. (**A**) Panoramic image of the control sample after three months of healing (31.2×); (**B**) representative histological microphotograph showing the bone defect partially filled with the newly formed trabecular bone (TB), hematopoietic bone marrow (BM) and periosteum layer (P) on the surface (125×).

2.3.2. Six Months

The most relevant finding during this study period was that the implanted material was completely enveloped by the new bone tissue, which penetrated large areas and mainly replaced the implanted material. Likewise, the continuity of the newly formed bone tissue came into close contact with the overlying cortical bone (*) (Figure 3H). The material's pores increased in size as a result of degradation, which led to a more irregular surface and favored bone in-growth.

At a higher magnification, Figure 3J highlights the presence of bone tissue on the periphery and in the implanted material's interior. Neither the immune response nor the formation of interposed fibrous structures at the material-bone tissue bone interface was observed (arrow). In the central implant area (Figure 3K), the new bone tissue deposition occurred mainly in the form of layers with a cortical architecture, and numerous osteocytes lacunae were noted. Figure 3L shows the vast quantity of mature bone tissue (*), and also new bone growing trabecularly adjacent to the material and inside the pores that come into close contact with the partially reabsorbed material (creeping substitution).

Newly formed bone tissue was observed at various maturation levels (Figure 3M). Mature bone with an osteon regular structure was surrounded by the areas where the new bony tissue was still in its early maturity stages (osteoid). Differences in the blue staining shade revealed scattered areas of older bone tissue (dark blue, *) and newly formed bone (light blue, arrow). During this period, the bone in all the scaffolds predominately comprised highly cellular disorganized woven and mature bone. Bone surfaces were populated by highly active cuboidal osteoblastic cells, which is consistent with mesenchymal (membranous) type bone ossification. Furthermore, presence of cement lines and filled osteocytic lacunae demonstrated healthy new mature bone apposition.

Finally, Figure 3N corresponds to the scaffold's interior. Presence of two nodular structures was evidenced, and one was composed of cells of a macrophage aspect and bone tissue that partially coated it. The other node dominated the presence of islets with osteoid and osteoblastic borders, and acquired the appearance of trabecular bone and newly formed trabecular bone. However, it was noteworthy that there was no inflammatory response and that fibrous tissue surrounded the material.

During the same period, the control samples showed how the bone defect was completely occupied by newly formed lamellar bone (Figure 5A). The new trabecular bone was thicker and composed of irregular lamellae with active osteocytes (Figure 5B,C). These histological findings formed part of the bone remodeling process in the endochondral ossification context.

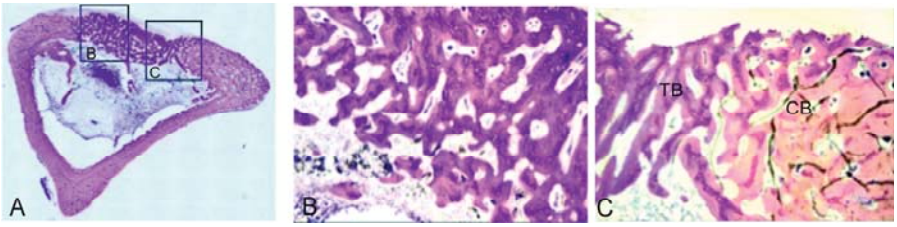

Figure 5. Representative histological microphotographs of the control samples after six months. (**A**) panoramic image (31.2×); (**B**) detail of the new trabecular bone (TB) (125×); and (**C**) detail of the boundary between compact bone (CB) and the newly formed trabecular bone (200×).

2.4. Histomorphometric Analysis

Histomorphometric analyses were carried out to establish the BIC values for the material, and gave high BIC values (67.30% ± 1.41 *) (with close contact observed). New bone ingrowth, defect closure and residual biomaterial were recorded and analyzed (Table 2). In the control samples, the newly formed bone in the cortical defect increased, and even in a smaller amount than in the grafted defects.

Table 2. Histomorphometric analysis to evaluate the BIC for the scaffold. Non parametric Friedman test. Significant differences (* $p < 0.05$). Control samples $n = 4$. Mean ± SD (Median).

	Implant Scaffold			Control	
%	**3 Months**	**6 Moths**	***p* Values ***	**3 Months**	**6 Moths**
BIC	58.34 ± 0.12 (58.34)	67.30 ± 1.41 (67.30) *	0.040	0.00 ± 0.0	0.00 ± 0.0
New Bone	51.66 ± 0.75 (51.66)	62.18 ± 2.28 (62.18) *	0.012	0.00 ± 0.0	0.00 ± 0.0
Residual	30.05 ± 1.13 (30.05) *	24.95 ± 0.99 (24.95)	0.013	0.00 ± 0.0	0.00 ± 0.0
Defect Closure	68.53 ± 1.62 (68.53)	80.08 ± 1.96 (80.08) *	0.025	24.84 ± 1.69 (24.85)	67.63 ± 1.70 (67.64)
Connective Tissue	18.29 ± 1.28 (18.29)	12.87 ± 1.45 (12.87)	0.041	0.00 ± 0.0	0.00 ± 0.0

2.5. Scanning Electron Microscopy Findings

A strong correlation was found between the SEM implantation results and the relevant histological findings. A low magnification cross-section at the implantation level revealed the tibia that contained the implant (Figure 6A).

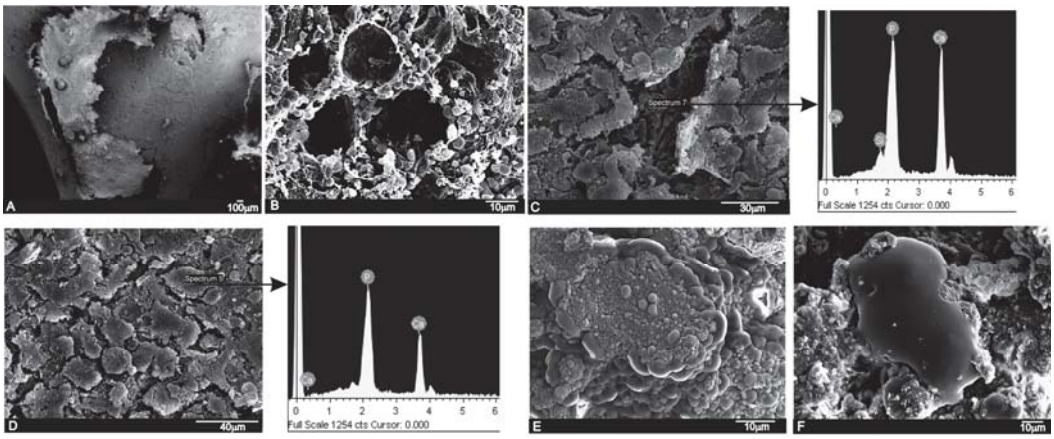

Figure 6. SEM images and EDS analyses of the scaffold implant after three months (**A**–**C**) and six months (**D**–**F**) of implantation. (**A**) general panoramic section of the tibia that contained the implant; (**B**) an abundant blood-fibrin structure partially lined the material's pores; (**C**) implant surface partially covered by an immature bone tissue and the EDS analysis; (**D**) the implant surface covered by newly formed bone tissue and the EDS analysis; (**E**) detail of the immature bone tissue's globular aspect; and (**F**) a macrophagic cell in close contact with the granular deposit from the implanted material.

In the SEM images, particles of implants were seen to be white-gray due to a low organic content and a relatively high Ca/P/Si ratio, whereas the newly formed bone was darker gray given the presence of collagen, bone marrow and fat. After three months of implantation, the scaffold material's general architecture was still visible. There were various elements from the hematopoietic bone marrow (erythrocytes, lymphocytes, platelets, macrophages) embedded in a fibrillar network, which surrounded the surface and were inside the material's pores (Figure 6B). The formation of a thin immature bone tissue layer, which partially covered the implant, was observed directly on the implant surface (Figure 6C). The EDS analysis of the underlayer was composed of a Ca-P-Si compound.

After six months of implantation, the whole ceramic implant surface was covered by a newly formed bone tissue (Figure 6D). The new bone layer was composed of Ca-P, mainly with traces of Si due to the gradual diffusion of Si ions from the scaffolds into the newly forming bone, which formed part of the biomaterial's resorption process. Details of the new bone layer show the characteristic globular pattern of a carbonate hydroxyapatite (Figure 6E). In some areas, another distinguishing characteristic was found: presence of irregularly shaped voluminous cells with cytoplasmatic extensions, which appeared macrophagic and were in close contact with small accumulations of the implanted particle which they surrounded, and different resorption process stages were seen.

Figure 7 shows the SEM image of the polished cross-section of the implant at three and six months. The cross-sectional SEM evaluation confirmed that the residual scaffold particles were surrounded by the newly formed bone, which presented mature bone characteristics with well-organized lamellae and numerous small osteocytic lacunae (Figure 7A,B,D). The bone-to-biomaterial interface was characterized by small numbers of newly formed bone projections, which reached scaffold particles (Figure 7C,E). The new bone that filled pores and particles was partially embedded in the new bone tissue (Figure 7A,B,D). Bony integration was well advanced in all the samples, and bone penetration was complete throughout deep and central zones.

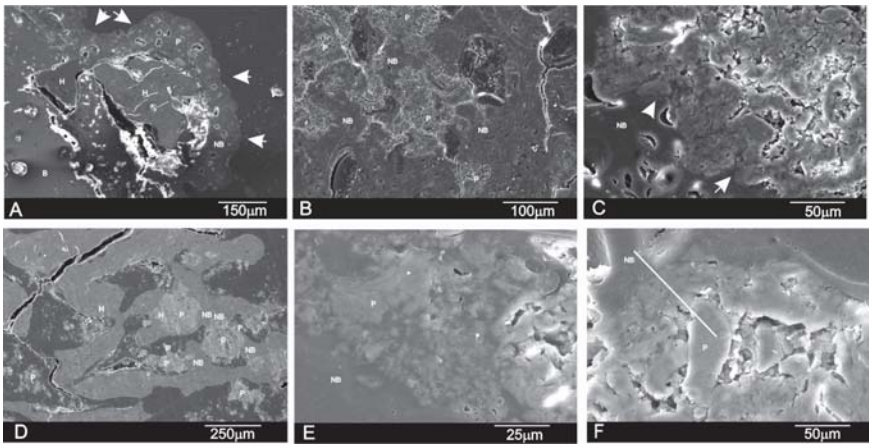

Figure 7. SEM images of the cross-section of the scaffold after (**A**–**C**) three months and (**D**–**F**) six months of implantation. (H indicates a pore filled with new bone, P refers to implant particles as a result of the degradation process, while NB refers to new bone tissue. Arrows indicate an irregular new bone boundary with partially degraded implant particles inside).

Figure 7F shows a representative SEM cross-section where the EDS analysis was done. An analysis was carried out at various points, following the recommendations of Lindgren et al. 2010 to take different points of interest from the middle and periphery of samples to detect changes in the Si/Ca/P ratios. Table 3 provides the descriptive statistics for our database. We found that active biomaterials resorption was underway. The EDS analysis of the residual scaffold particles in the retrieved tissue revealed a Ca/P ratio of varying relative proportions. An elemental analysis of the residual scaffold at different points revealed some categories of particles with different mean Ca/P ratios according to degradation status. For the statistical data, an elemental analysis indicated a relatively high Ca/P ratio in the residual scaffolds ($2.62 < Ca/P < 2.68$) and at the bone interface ($2.20 < Ca/P < 2.36$) compared to the new bone ($1.89 < Ca/P < 1.97$). The specific Si ion concentration in the scaffold lowered from 10.77 ± 0.03 wt % in the material before being implanted to $6.89 < Si < 7.46$ after implantation and at the bone interface ($0.26 < Si < 0.12$) compared to the new bone ($0.07 < Si < 0.04$). This finding suggests that the gradual diffusion of the Ca and Si ions from the biomaterial to the newly forming bone at the interface forms part of the biomaterial's resorption process.

Table 3. EDS analysis with the Si (wt %) and Ca/P molar in the new bone region; the interface and the residual biomaterial after three and six months of implantation. Mean ± SD (Median).

	3 Months		6 Months	
	Si (wt %)	**Ca/P**	**Si (wt %)**	**Ca/P**
Residual Scaffold	7.46 ± 1.06 (7.46)	2.62	6.89 ± 1.04 (6.89)	2.68
Interphase	0.26 ± 0.24 (0.26)	2.20	0.12 ± 0.46 (0.12)	2.36
New bone	0.07 ± 1.03 (0.07)	1.97	0.04 ± 1.11 (0.04)	1.89

3. Discussion

Interconnected Si-Ca-P porous scaffolds, where a porous polymer sponge was used as a template, were processed to be used as novel material with osteoconductive properties for bone reconstruction, with similar properties to autologous bone grafts. The main findings showed that the porous scaffold degraded over the experimental set points and allowed new bone tissue formation.

The porous bioactive scaffold also induced new bone tissue formation inside the material in three ways: (i) invasion of newly formed bone tissue on the material's surface using the network of interconnected pores, with the material starting from the periphery toward its center; (ii) macrophage activity that precedes invasion or penetration of bone marrow, which provides a capillary axis accompanied with vascular cells, and an osteoblastic line; and (iii) the material per se is able to create the microenvironment required around it to locally carry out the osteogenic differentiation of the osteogenic precursor cells contained in the hematopoietic bone marrow.

Porous bioactive scaffolds are most interesting to be used as bone substitutes in the bone tissue engineering field [16]. High bioactivity and adequate scaffold porosity are essential characteristics to stimulate osteoprogenitor cells and to support bone in-growth. Furthermore, resorption of the material with the same bone formation rate is required [17]. Several in vivo studies have demonstrated that Si influences bone mineralization [9,10], metabolism [18,19], collagen synthesis [20,21] and crosslinking [22]. These findings fall in line with the results of the current study, which revealed continuous newly bone tissue in-growth in the defect area, inside pores and in the spaces left by the degraded scaffold. After implantation, the dissolution of Si and Ca ions from the scaffold to bone tissue stimulates the formation of a carbonate-hydroxyapatite layer, which acts as a template for osteoblast growth and can affect osteogenesis [3,4,23,24]. High porosity and adequate pore sizes are essential factors for effective bone substitute material. Scaffolds with an optimal pore size allow bone in-growth and support neovascularization. Both the pore size and porosity of the bioactive scaffold used herein indicate its morphological characteristics, which make it suitable for being used as a bone graft. Moreover, the histological findings demonstrated that the scaffold degraded over time and that degradation happened according to the tissue in-growth rate. Besides adequate porosity, proper scaffold degradation is also essential for the process to happen since new bone tissue formation needs space to grow in [3,4,23,24].

Several techniques have been used to assess the biomaterial-to-bone tissue interface. Many evaluations of the interface using LM, SEM, and TEM have shown how the same structure is represented differently depending on the examination method selected [25,26]. The traditional method used during bone regeneration, histological staining followed by examination under a light microscope, provides substantial information. However, its low spatial resolution does not provide ultrastructural information. The precision and reliability of a histomorphometric study of newly formed bone depends on the correct identification and ultrastructural characterization of all the cellular components that could play a role in the osseointegration process. LM lacks the resolving power required for detailed structural analyses. Electron microscopy techniques can help characterize the morphological changes that occur during osseointegration. Despite certain limitations [27], transmission electron microscopy has been successfully used to describe the cellular components of newly formed bone.

SEM, used to examine bone-to-biomaterial interfaces, was first reported by Jasty et al. [28]. This method has been employed mainly for descriptive studies performed with calcified tissue [29,30]. SEM images can be used to highlight contrasts between areas of different chemical compositions, and this technique is especially effective whenever average atomic numbers of the components of each region vary. Since SEM signal intensity depends on the sample's mean atomic number, the SEM technique not only serves to distinguish inorganic features, but also offers the interesting possibility of identifying ultrastructural cell components and their micromorphological details.

In the present study, the LM, SEM and EDS analyses revealed a close relation between the newly formed bone matrix and the scaffold particle surface. The elemental analysis of bone tissue demonstrated the presence of calcium and phosphorus, which indicated the presence of mineralized bone tissue on the particle surface (Tables 2 and 3). This observation suggests that the scaffold surface could provide an optimal stratum for bone tissue in-growth. The SEM analysis also showed that the new bone matrix had grown over the scaffold surface, and had completely penetrated the deep central zones through its porous structure. After six months of implantation, the scaffold implant had well integrated into the host tissue, and had formed an irregular surface boundary caused by the material's gradual degradation (Figures 6 and 7). The interface developed between the implant and the surrounded tissue was characterized by the intermittent presence of the calcium phosphate phase, which corresponded to new bone tissue in structure and morphology terms.

The new bone ingrowths in the implant were more evident at six months and advanced into the spaces between the exposed scaffold particles in the implant to form a characteristic interlocking pattern at the interface as the process moved further into the implant. SEM (Figure 7) showed a massive bone colonization of the implant through the original scaffold pores, caused by the structure's gradual dissolution. Due to these advanced processes, the scaffold material's free particles were found in many areas across the restructuring implant. Densities at the bone-ceramic interface and inside the material gradually and significantly reduced. This indicates that the resortive process went from the periphery to the center, and it initiated in an early material implantation stage by a cellular mechanism (macrophage cells). At the end of the study (six months), the central part of the implanted material remained partially degraded as it was in the histological and radiological images (Figures 2 and 3). However, a lot of new bone was observed in bone defects treated with the scaffold, in which 62.18% $\pm$ 2.28% of the bone defect was filled by the newly formed bone after six months of implantation (Table 2).

We conclude that the results of this initial research confirmed our hypothesis that the high resorbable porous bioactive calcium silicophosphate scaffold has an adequate porosity structure and is able to support bone tissue in-growth by new bone, while gradually being resorbed by the cell-mediated process at the same time. Thus, it constitutes a promising alternative to be used as bone grafts for tissue engineering. Future research should be conducted using other scaffolds made from standard biomaterials, such as Si-HA or Si-TCP. The ceramic's biological performance should be investigated in different bone defect models and animals, and probably with long-term assays, as proposed in International Standard ISO-10993-5.

4. Materials and Methods

4.1. Biomaterial

In this study porous scaffolds, which corresponded to the 28.39 wt % Nurse'A—71.61 wt % Silicocarnotite composition, were produced by the polymer replication method.

Nurse's A (7CaOP2O52SiO2) and Silicocarnotite (5CaOP2O5SiO2) ceramic powders synthesized previously in our laboratory were used as starting materials. Details of the technique and the characterization of the starting materials can be found in previous publications [7,8,13]. First, the desired proportions of each component were weighed on an analytical balance and powder was thoroughly attrition-milled in alcoholic media (isopropilic alcohol) using ZrO_2-Y_2O_3 balls (1 mm

diameter) for 4 h. The resulting particle size was 2.1 μm measured with laser scattering particle size equipment (Mastersizer, Malvern, UK). Ceramic slurry was prepared with 60% solid contents in water media. Dolapix CE-64 (Zschimmer Schwartz, Lahnstein, Germany) was added as a defloculant (1 wt %) and Optapix PAF-35 (Zschimmer Schwartz, Lahnstein, Germany) as a binder (3 wt %). The powder:water ratio was 60:40.

Scaffolds were prepared using polyurethane sponges with open cells (60 ppi) as a template. Sponges were impregnated with ceramic slurry and sintered at 1450 °C for 2 h with 5 °C/min as the heating and cooling rates. Then, powder was turned off and samples were allowed to cool inside the furnace for 24 h. Next cylindrical scaffolds (5 ± 1 mm diameter and 6 ± 0.3 mm long) were cleaned and washed several times in sterile PBS solution, dried at 37 °C, and finally sterilized by gas plasma (Sterrad-100S, Irvine, CA, USA) and kept in individual packages under sterile conditions until implantation.

The microstructure of the scaffolds was characterized by scanning electron microscopy (SEM-Hitachi S-3500N, Ibaraki, Japan). The chemical composition was qualitatively determined by an Energy Dispersive X-ray Spectroscopy system (EDS-INCA system, by Oxford Instruments Analytical, High Wycombe, UK).

4.2. Animals and Surgical Procedure

Mature male New Zealand (NZ) rabbits (n = 8, 4.0 ± 0.3 kg) were used. Animals were divided and randomly assigned (simple randomization) into two time groups of four animals ($n1$ = 4, $n2$ = 4) according to the previously set 3- and 6-month periods. Animals were not placed on a special diet, but received feed and water ad libitum. Animals were housed in individual standard steel cages and maintained in a 12:12 h light dark cycle under controlled environmental conditions. All the animals were allowed 1 week from their arrival to facilitate acclimation.

The study protocol was examined and approved by the Institutional Ethic and Animal Experimentation Committee of the Miguel Hernandez University according to Spanish Government Guidelines and European Community Guidelines for animal care (authorized no. 2014/VSC/PEA/00056 tipo2).

Animals were pre-medicated and anesthetized by an intramuscular (im) injection of Atropine sulfate, 0.3 mg·kg^{-1} and hydrochloride of clorpromazine, 10 mg·kg^{-1}, and then hydrochlorate of ketamine, 50 mg·kg^{-1} and xylazine 5 mg·kg^{-1}. As an antibiotic prophylaxis, a single dose of Enrofloxacin 2.5 mg·kg^{-1} im (Virbac, Barcelona, Spain) was provided. Both legs were shaved and washed with Chlorhexidine® (Bohm SA, Madrid, Spain). Then Betadine® (Meda Manufacturing, Bourdeaux, France) was applied and the surgical area was covered with a sterile drape. Afterward, a longitudinal incision (1.2–1.5 cm long) was made along the medial aspect in the proximal metaphysial area of each tibia. Subcutaneous tissue, fascia and periostium were dissected to expose the medial surface of the tibia. An end-cutting bur (5 mm diameter) was connected to a micromotor at low revolutions with continuous saline irrigation/suction to avoid overheating and thermal damage to bone, and was used to create an unicortical bone defect (5 mm diameter) to avoid invading the medullary cavity. Sufficient hemostasis was achieved. Then, the defect was thoroughly washed several times with physiological saline before performing implantation and removing bone debris to avoid it entering the defect. Porous cylindrical implants were press-fit placed into the defects to ensure initial stability. Identical osseous defect at the contralateral tibia remained empty (ungrafted) as a control.

Afterward, wounds were carefully and closed sutured by a meticulous technique (anatomical layers) with continuous absorbable sutures (Vicryl™ 3/0 (Agatho AB, Lidingo, Sweden) for deep planes and Vicryl Rapid™ 3/0 for skin). Then, a single local anesthetic (0.2 mL·kg^{-1}, chlorhydrate lidocaine 2%, subcutaneously) was provided routinely at the surgery site to avoid immediate postoperative pain. On the first three post-surgery days, animals were given a subcutaneous injection of 0.1 mL·kg^{-1} of Tolphenamic acide twice a day (every 12 h) as an analgesic control. They were allowed to freely move (limb loading) immediately after restoring from anesthesia. They all survived the 3- and 6-month study

periods, and surgical wounds healed with no complications or infection. Therefore, all the animals were included in the study. Total limb loading was allowed after restoring from anesthesia.

At the end of the 3- and 6-month periods, animals were euthanized under sedation (hydrochlorate of ketamine, 50 $mg \cdot kg^{-1}$ im), with an overdose (0.5 mL) of pentobarbital sodium (Dolethal™, Lab. Vetoquinal, Cedex, France) intracardiacally. To remove the implanted area, the same surgical procedure as that described above was followed.

4.3. Radiographic Imaging

Two X-ray images (standard antero-posterior and lateral projection angles) were obtained of the area of the bone-containing implants, which was cleaned of adherent soft tissue by the Kodak RVG 6100 Digital Radiography System (Kodak DS, Rochester, NY, USA) with an X-ray taken at 32 kV, 40 mA by automatic light metering. Radiographs of all the specimens were taken. Images were used to observe changes in the morphology and radiological density (radiopacity) descriptive levels of the material in the medullar and cortical areas where defects were created.

4.4. Histological and Histomorphometric Analysis

After 3 and 6 months, the implants together with the surrounding tissues were removed and fixed in 10% neutral buffered formalin and decalcified. The decalcification method utilized Osteomoll Merck KbaA (Darmstadt, Germany) that contained HCl (10%) and CH_2O (4%), immersing samples for 17 days, and the solution was renewed every 24 h. Subsequently, all the samples were paraffin embedded, sectioned at 5 μm, and stained using hematoxylin-eosin (H-E, red stain) and Masson's trichrome (MT) stain. The entire circumference of each section (containing bone, scaffold particles, and connective tissue) was traced manually to create an individual region of interest (ROI).

Histomorphometric evaluations consisted of taking measurements of the area of material in relation to the total measurement area. These were carried out using Image J software (developed by the National Institute of Health (NIH), Bethesda, MD, USA). Examinations were performed under a Nikon Elipse 80i microscope (Teknooptik AB, Huddinge, Sweden), equipped with an Easy Image 2000 system (Teknooptik AB, Huddinge, Sweden). Images were generated using a Leica Z6 APO microscope connected to a Leica DC 500 (Barcelona, Spain) digital camera. After calibrating the system and digitalizing images, interactive measurements of the areas of interest were obtained with the Leica QWin V3 image analysis software (Barcelona, Spain). The histomorphometric analysis produced one BIC measurement, measured as the percentage of the circumference, and length of the cylinder that came into contact with new bone. In the same way, the cortical bone defect in the control group was also evaluated.

4.5. Scanning Electron Microscopy Study

To assess the continuing effect of the implant in the medullary cavity surrounded by hematopoietic bone marrow from an ultrastructural point of view, cross-sections of the non-decalcified tissues were also examined for the ultrastructural study in SEM-EDS. Therefore, some sections (1–2 mm) in the implantation area were fixed by immersion in 3% glutaraldehyde after being soaked in buffer solution for 4 h, postfixed in 1% osmium tetroxide for 1 h at 4 °C, and washed in 0.1 M cacodilate solution and dehydrated in graded ethanol solutions series, and embedded in hydroxyethyl methacrylate resin. They were then polished with 1-μm diamond pastes for the SEM-EDS analyses. Back-scattered SEM imaging was employed to highlight the contrasts among the resin, bone and the biomaterial.

4.6. Statistical Analysis

A statistical analysis was performed with the PASW Statistics v.20.0.0 software (SPSS Inc., Armonk, NY, USA). Sample size was pre-calculated using the statistical method provided by the software. Values were recorded as means ± standard deviation and medians. The pre-statistical analysis of sample distribution was performed to evaluate normality. Kolmogorov and Smirnov's test values were normal.

A non-parametric Friedman Test for the related samples was applied to the comparison of the medians and to quantify any relationships between differences ($p < 0.05$).

5. Conclusions

The biocompatibility of this novel porous calcium silicophosphate, developed by the polymer replication method, was high and caused no local or systemic immune inflammatory response, and no fibrosis was developed between the ceramic and bone after its intramedullary implantation into a rabbit tibia.

The results indicate that this material provides an optimal microenvironment for the osteogenic differentiation of the undifferentiated osteoblastic precursor cells contained in hematopoietic bone marrow. Their suitable interconnected network porous structure facilitates colonization by new bone tissue and bone marrow. Presence of the vascular capillaries that surround the material promotes this process by providing all the necessary nutrients.

This confirms that the porous calcium silicophosphate obtained in this work favors and supports the integration of bone by combining osteoconductive behavior with the enhanced bone tissue in-growth of the open-pore structure. The dynamic biodegradation of the ceramic with time was also documented. Densities were reduced throughout the study as a result of the simultaneous phagocytic activity of macrophages.

Finally, we therefore conclude that this novel porous calcium silicophosphate ceramic scaffold implanted into the medullary cavity is biocompatible, bioresorbable, osteoconductive and has osteogenic potential. Hence, it can be considered a potential substitute of bone tissue, and is suitable for clinical applications in filling bone defects and being used as a scaffold or matrix for bone tissue engineering.

Acknowledgments: Part of this work has been supported by the Spanish Ministry of Economy and Competitiveness (MINECO) contract grant number: MAT2013-48426-C2-1-R and MAT2013-48426-C2-2-R.

Author Contributions: Patricia Ros-Tárraga and Patricia Mazón performed the implant characterization; Miguel A. Rodríguez performed the preparation of the implants by the polymer replication method, Luis Meseguer-Olmo conducted surgery, and, together with Piedad N. De Aza, designed and performed the experiments and prepared the manuscript. All of the authors contributed to the analyses and discussion of the results.

Conflicts of Interest: The authors declare no conflicts of interest.

References

1. Hutmacher, D.W.; Schantz, J.T.; Lam, C.X.F.; Tan, K.C.; Lim, T.C. State of the art and future directions of scaffold-based bone engineering from a biomaterials perspective. *J. Tissue Eng. Regen. Med.* **2007**, *1*, 245–260. [CrossRef] [PubMed]
2. Baino, F.; Caddeo, S.; Novajra, G.; Vitale-Brovarone, C. Using porous bioceramic scaffolds to model healthy and osteoporotic bone. *J. Eur. Ceram. Soc.* **2016**, *26*, 2175–2182. [CrossRef]
3. Jones, J.R. New trends in bioactive scaffolds: The importance of nanostructure. *J. Eur. Ceram. Soc.* **2009**, *29*, 1275–1281. [CrossRef]
4. Hench, L.L.; Polak, J.M. Third-generation biomedical materials. *Science* **2002**, *295*, 1014–1017. [CrossRef] [PubMed]
5. Vitale-Brovarone, C.; Ciapetti, G.; Leonardi, E.; Baldini, N.; Bretcanu, O.; Verné, E.; Baino, F. Resorbable Glass-Ceramic Phosphate-Based Scaffolds for Bone Tissue Engineering: Synthesis, Properties and in Vitro Effects on Human Marrow Stromal Cells. *J. Biomater. Appl.* **2011**, *26*, 465–489. [CrossRef] [PubMed]
6. Renghini, C.; Giuliani, A.; Mazzoni, S.; Brun, F.; Larsson, E.; Baino, F.; Vitale-Brovarone, C. Microstructural characterization and in vitro bioactivity of porous glass-ceramic scaffolds for bone regeneration by synchrotron radiation X-ray microtomography. *J. Eur. Ceram. Soc.* **2013**, *33*, 1553–1565. [CrossRef]
7. Serena, S.; Caballero, A.; de Aza, P.N.; Sainz, M.A. New evaluation of the in vitro response of silicocarnotite monophasic material. *Ceram. Int.* **2015**, *41*, 9411–9419. [CrossRef]

8. Lugo, G.J.; Mazón, P.; de Aza, P.N. Phase transitions in single phase Si-Ca-P-based ceramic under thermal treatment. *J. Eur. Ceram. Soc.* **2015**, *35*, 3693–3700. [CrossRef]
9. Velasquez, P.; Luklinska, Z.B.; Meseguer-Olmo, L.; Mate-Sanchez de Val, J.E.; Delgado-Ruiz, R.A.; Calvo-Guirado, J.L.; Ramirez-Fernandez, M.P.; de Aza, P.N. αTCP ceramic doped with Dicalcium Silicate for bone regeneration applications prepared by powder metallurgy method. In vitro and in vivo studies. *J. Biomed. Mater. Res. A* **2013**, *101*, 1943–1954. [CrossRef] [PubMed]
10. De Aza, P.N.; Peña, J.I.; Luklinska, Z.B.; Meseguer-Olmo, L. Bioeutectic® ceramics for biomedical application obtained by Laser Floating Zone Method: In vivo evaluation. *Materials* **2014**, *7*, 2395–2410. [CrossRef]
11. Ros-Tarraga, P.; Mazón, P.; Meseguer-Olmo, L.; de Aza, P.N. Revising the subsystem nurse's A–phase-silicocarnotite within the system $Ca_3(PO_4)_2$–Ca_2SiO_4. *Materials* **2016**, *9*, 322. [CrossRef]
12. Lugo, G.J.; Mazón, P.; Baudin, C.; de Aza, P.N. Nurse's A phase: Synthesis and characterization in the binary system Ca_2SiO_4-$Ca_3(PO_4)_2$. *J. Am. Ceram. Soc.* **2015**, *98*, 3042–3046. [CrossRef]
13. Lugo, G.J.; Mazón, P.; de Aza, P.N. Material processing of a new calcium silicophosphate ceramic. *Ceram. Int.* **2016**, *42*, 673–680. [CrossRef]
14. Nagelschmidt, G. A new calcium silicophosphate. *J. Chem. Soc.* **1937**, 865–867. [CrossRef]
15. Serena, S.; Sainz, M.A.; Caballero, A. Single-phase silicocarnotite synthesis in the subsystem $Ca_3(PO_4)_2$–Ca_2SiO_4. *Ceram. Int.* **2014**, *40*, 8245–8252. [CrossRef]
16. Rabadan-Ros, R.; Velasquez, P.; Meseguer-Olmo, L.; de Aza, P.N. Morphological and structural study of a novel porous Nurse's A ceramic with osteoconductive properties for tissue engineering. *Materials* **2016**, *9*, 474. [CrossRef]
17. De Aza, P.N.; Mate-Sanchez de Val, J.E.; Baudin, C.; Perez Albacete-Martínez, C.; Armijo Salto, A.; Calvo-Guirado, J.L. Bone neoformation of a novel porous resorbable Si-Ca-P base ceramic with osteoconductive properties: Physical and mechanical characterization, histological and histomorphometric study. *Clin. Oral Implant. Res.* **2016**. [CrossRef] [PubMed]
18. Najda, J.; Gminski, J.; Drozdz, M.; Danch, A. The action of excessive, inorganic silicon (Si) on the mineral metabolism of calcium (Ca) and magnesium (Mg). *Biol. Trace Elem. Res.* **1993**, *37*, 107–114. [CrossRef] [PubMed]
19. Seaborn, C.D.; Nielsen, F.H. Dietary silicon and arginine affect mineral element composition of rat femur and vertebra. *Biol. Trace Elem. Res.* **2002**, *89*, 239–250. [CrossRef]
20. Mate-Sanchez de Val, J.E.; Mazon, P.; Calvo-Guirado, J.L.; Delgado-Ruiz, R.A.; Ramirez-Fernandez, M.P.; Negri, B.; Abboud, M.; de Aza, P.N. Comparison of three novel β-tricalcium phosphate/collagen ceramic scaffolds. An in vivo study. *J. Biomed. Mater. Res. A* **2014**, *102*, 1037–1046. [CrossRef] [PubMed]
21. Leu, A.; Leach, J.K. Proangiogenic potential of a collagen/bioactive glass substrate. *Pharm. Res.* **2008**, *25*, 1222–1229. [CrossRef] [PubMed]
22. Lu, H.H.; El-Amin, S.F.; Scott, K.D.; Laurencin, C.T. Three-dimensional, bioactive, biodegradable, polymer-bioactive glass composite scaffolds with improved mechanical properties support collagen synthesis and mineralization of human osteoblast-like cells in vitro. *J. Biomed. Mater. Res. A* **2003**, *64*, 465–474. [CrossRef] [PubMed]
23. Mate-Sanchez de Val, J.E.; Calvo-Guirado, J.L.; Delgado-Ruiz, R.A.; Ramirez-Fernandez, M.P.; Martinez, I.M.; Granero-Marin, J.M.; Negri, B.; Chiva-Garcia, F.; Martinez-Gonzalez, J.M.; de Aza, P.N. New block graft of α-TCP with silicon in critical size defects in rabbits: Chemical characterization, histological, histomorphometric and micro-CT study. *Ceram. Int.* **2012**, *38*, 1563–1570. [CrossRef]
24. Mate-Sanchez de Val, J.E.; Calvo-Guirado, J.L.; Delgado-Ruiz, R.A.; Ramirez-Fernandez, M.P.; Negri, B.; Abboud, M.; Martinez, I.M.; de Aza, P.N. Physical properties, mechanical behavior, and electron microscopy study of a new α-tcp block graft with silicon in an animal model. *J. Biomed. Mater. Res. A* **2012**, *100*, 3446–3454. [CrossRef] [PubMed]
25. De Aza, P.N.; Luklinska, Z.B.; Mate-Sanchez de Val, J.E.; Calvo-Guirado, J.L. Biodegradation process of α-tricalcium phosphate and α-tricalcium phosphate solid solution bioceramics in vivo: A comparative study. *Microsc. Microanal.* **2013**, *19*, 1350–1357. [CrossRef] [PubMed]
26. Orsini, G.; Traini, T.; Scarano, A.; Degidi, M.; Perrotti, V.; Piccirilli, M.; Piattelli, A. Maxillary sinus augmentation with BioOss particles: A light, scanning, and transmission electron microscopy study in man. *J. Biomed. Mater. Res. B* **2005**, *7*, 448–457. [CrossRef] [PubMed]

27. Wierzchos, J.; Falcioni, T.; Kiciak, A.; Wolinski, J.; Koczorowski, R.; Chomicki, P.; Porembska, M.; Ascaso, C. Advances in the ultrastructural study of the implant-bone interface by backscattered electron imaging. *Micron. Int. Res. Rev. J. Microsc.* **2008**, *39*, 1363–1370. [CrossRef] [PubMed]
28. Jasty, M.; Bragdon, C.R.; Schutzer, S.; Rubash, H.; Haire, T.; Harris, W.H. Bone ingrowth into porous coated canine total hip replacements. Quantification by backscattered scanning electron microscopy and image analysis. *Scanning Microsc.* **1989**, *3*, 1051–1057. [PubMed]
29. Skedros, J.G.; Bloebaum, R.D.; Bachus, K.N.; Boyce, T.M. The meaning of gray levels in backscattered electron images of bone. *J. Biomed. Mater. Res.* **1993**, *27*, 47–56. [CrossRef] [PubMed]
30. Skedros, J.G.; Bloebaum, R.D.; Bachus, K.N.; Boyce, T.M.; Constantz, B. Influence of mineral content and composition on gray levels in backscattered electron images of bone. *J. Biomed. Mater. Res.* **1993**, *27*, 57–64. [CrossRef] [PubMed]

9. RESULTADOS Y DISCUSIÓN

4. RESULTADOS Y DISCUSIÓN

Los resultados obtenidos en la presente Tesis Doctoral confirman la hipótesis de trabajo establecida inicialmente, puesto que se han obtenido materiales con un prometedor comportamiento para su uso en el campo de la regeneración del tejido óseo. Con objeto de dotar de mayor claridad a la Tesis Doctoral, los resultados obtenidos se van a exponer según la composición y el método de obtención de las biocerámicas utilizadas en los diferentes ensayos:

Por una parte se incluirán los resultados de las publicaciones ***"New 3D stratified Si-Ca-P porous scaffolds obtained by sol-gel and polymer replica method: Microstructural, mineralogical and chemical characterization"*** e ***"In vitro behaviour of sol-gel interconnected porous scaffolds of doped wollastonite"***. En ambos trabajos, las biocerámicas fueron obtenidas mediante los métodos sol-gel y replicación polimérica, siguiendo los diagramas de fases ternario SiO_2 – CaO – P_2O_5, y cuaternarios MgO – K_2O – CaO – SiO_2 y Na_2O – K_2O – CaO – SiO_2.

Por otra parte, se expondrán los resultados de las publicaciones "***Revising the Subsystem Nurse's A - Phase-Silicocarnotite within the System $Ca_3(PO_4)_2$ - Ca_2SiO_4"***, ***"Assessment of Effects of Si-Ca-P Biphasic Ceramic on the Osteogenic Differentiation of a Population of Multipotent Adult Human Stem Cells"*** **y** ***"Novel Resorbable and Osteoconductive Calcium Silicophosphate Scaffold Induced Bone Formation"*****.** En estos casos, las biocerámicas fueron obtenidas mediante dos técnicas diferentes: reacción en estado sólido y replicación polimérica utilizando una barbotina. En ambas técnicas se obtuvieron biocerámicas con composición perteneciente al diagrama de fases binario C_2S – TCP.

En primer lugar, en la publicación ***"New 3D stratified Si-Ca-P porous scaffolds obtained by sol-gel and polymer replica method: Microstructural, mineralogical and chemical characterization"*** se muestra una nueva metodología para obtener biocerámicas porosas estratificadas, donde la composición de cada una de las capas puede ser modificada según las necesidades, convirtiendo a esta metodología en una de las formas de obtención de cerámicas porosas más versátiles existentes hoy día. El sistema desarrollado consiste en introducir una esponja de poliuretano dentro de un fluido, obtenido a través del proceso sol-gel, para que absorba la mayor cantidad de líquido posible. A continuación, se procede a eliminar el exceso de fluido, dejando la cantidad necesaria que permita recubrir el cuerpo de la esponja sin tapar los poros. En este punto, la esponja se seca a una

temperatura próxima a 140ºC y, una vez seca, se repite el proceso tantas veces como se considere oportuno.

La composición empleada para el desarrollo de las biocerámicas del presente trabajo fue 29,32% en peso de SiO_2 - 67,80% en peso de CaO - 2,88% en peso de P_2O_5.

Utilizando la metodología antes descrita, se obtuvieron diferentes materiales cerámicos porosos estratificados, donde se modificó el número de capas, siendo 8 el número mínimo y 12 el máximo. Para eliminar la esponja de poliuretano y proporcionar la máxima resistencia a las cerámicas, las muestras fueron sinterizadas a 950ºC y 1400ºC. A partir de estos tratamientos térmicos, se observó que al aumentar tanto el número de capas, como la temperatura de sinterización, se producía un aumento de la densidad de las muestras, reducción del tamaño de poro y aumento del número de poros tapados.

Los valores de resistencia a compresión diametral, son coincidentes con los valores más altos mostrados por otro tipo de materiales (49, 50), siendo las muestras obtenidas a 1400ºC las que presentaron la mayor resistencia, soportando presiones de 0,04 MPa.

La caracterización mineralógica de las cerámicas, se realizó mediante Difracción de Rayos X (DRX), utilizando muestras con 8 capas, sinterizadas a 950ºC (a partir de ahora 3D-950/8) y muestras con 8 capas sinterizadas a 1400ºC (a partir de ahora 3D-1400/8). Los resultados obtenidos indican que las muestras 3D-950/8 están compuestas, principalmente, por una fase amorfa de silicato cálcico con pequeñas trazas de sílice en forma de cristobalita y tridimita, mientras que las muestras 3D-1400/8 están constituidas por una fase amorfa de silicato cálcico con pequeñas trazas de sílice en forma de cristobalita y tridimita, además de presentar pequeñas trazas de fosfato tricálcico (TCP). La presencia de las fases polimorfas de SiO_2 (cristobalita y tridimita) en ambas muestras es debido al proceso de obtención de las biocerámicas, ya que durante la formación de la disolución sol-gel, se establecen enlaces Si–O–Si que permiten estabilizar la red tridimensional. Sin embargo, la cristobalita no debería de aparecer a temperaturas inferiores a 1470ºC, pero está demostrado que la presencia de trazas de fósforo contribuyen a estabilizar fases de SiO_2 a temperaturas menores (51), motivo por el que la cristobalita aparece incluso en las muestras obtenidas a 950ºC.

Por otra parte, el aumento de la temperatura de sinterización desde 950ºC hasta 1400ºC, permite observar dos grandes cambios en las fases mineralógicas que

conforman las biocerámicas porosas obtenidas: el primero es el aumento de la cristalinidad en las fases formadas por SiO_2, y el segundo es que aparece una fase de β-TCP, que corresponde con la forma del TCP de menor temperatura (52-54).

El punto fuerte de esta metodología de obtención de matrices porosas estratificadas, utilizando el método sol-gel y la replicación polimérica, es la capacidad de modificar las propiedades de los biomateriales introduciendo capas con diferente composición. Por este motivo, se decidió estudiar el comportamiento de cerámicas dopadas con nuevos iones: por un lado, biocerámicas con composición 1,40% en peso de MgO - 1,62% en peso de K_2O - 45,33% en peso de CaO - 51,66% en peso de SiO_2 y biocerámicas con 2,12% en peso de Na_2O - 1,60% en peso de K_2O - 45,00% en peso de CaO - 51,28% en peso de SiO_2, nombradas a partir de ahora como biocerámicas con magnesio (Mg) y con sodio (Na), respectivamente, para diferenciarlas entre sí. Los resultados obtenidos tras llevar a cabo su caracterización están expuestos en la publicación "***In vitro behaviour of sol-gel interconnected porous scaffolds of doped wollastonite***".

Los patrones obtenidos mediante DRX de ambas composiciones, mostraron que las biocerámicas de Na estaban formadas por 3 fases: cristobalita, pseudowollastonita (psW) y wollastonita-2M (W-2M); y las biocerámicas de Mg estaban formadas por 2 fases: psW y W-2M. La psW y la W-2M están formadas por cadenas lineales simples con 2 oxígenos por tetraedro de SiO_4, unidas entre sí mediante cationes (55). Sin embargo, la cristobalita está formada por tetraedros de SiO_4 formando capas con anillos hexagonales, por lo que tiene menos oxígenos no unidos que las fases psW y W-2M (56). La disposición de los tetraedros de SiO_4 influye en el número de grupos Si–OH presentes en las muestras y estos grupos, a su vez, influyen en la bioactividad de los biomateriales (57). Por este motivo, aquellas muestras formadas por Mg tienden a formar más grupos Si-OH por átomo de oxígeno no-unido que las muestras formadas por Na, por lo que cabría esperar una mayor bioactividad.

Por otra parte, se observaron las características geométricas de los poros de las matrices porosas utilizando Microscopía Electrónica de Barrido (MEB). Se pudo ver que presentaban una porosidad interconectada, al igual que las muestras obtenidas en el trabajo anterior, con un diámetro de poro de 200 – 400 μm, lo que permitirá una excelente permeación de células, nutrientes y desechos.

Los resultados de resistencia a compresión obtenidos fueron 0,03 MPa para las muestras con Na y 0,02 MPa para las muestras con Mg. Son valores

relativamente bajos pero, como se ha mecionado anteriormente, concuerdan con los obtenidos en materiales con elevada porosidad (49).

Una vez observada la osteoconducción de las muestras, y haber obtenido una resistencia a compresión suficiente como para que las biocerámicas fuesen fácilmente manipulables, se estudió su comportamiento *in vitro*, sumergiendo las piezas porosas en suero fisiológico artificial (SFA) durante 6 horas, 3, 7 y 14 días. Las muestras con Mg mostraron pequeñas partículas lisas y esféricas de 1 μm de diámetro sobre su superficie tras 6 horas sumergidas en SFA, mientras que las de Na necesitaron 3 días para observar los primeros precipitados esféricos, presentando una morfología totalmente diferente. En este caso, las esferas tenían una apariencia rugosa, compuestas por nanocilindros de 200 – 400 nm. Esta diferencia en los tiempos necesarios para observar precipitados sobre la superficie de las biocerámicas (bioactividad) coincide con los esperados a partir de las fases obtenidas por DRX. A pesar de que el precipitado que muestran las piezas con Mg no es extenso, el hecho de estar presente después de tan solo 6 horas de inmersión en SFA indica la alta bioactividad del material, similar a la de los materiales más bioactivos que se muestran en la literatura (58-60). Tras 3 días de inmersión de las muestras con Mg en SFA, comenzaron a fusionarse las partículas, formando una capa de apatito (fosfato cálcico, CaP) y tras 7 y 14 días, la superficie de las matrices estaba prácticamente cubierta por una capa mucho más gruesa de precipitado. Cuando se observó una imagen magnificada de las partículas que constituían esta capa de CaP, se pudo ver una superficie rugosa compuesta por otras partículas con morfología de nanobarra de 50 – 100 nm. Del mismo modo, las muestras con Na también mostraron una capa gruesa de apatito sobre su superficie tras 7 y 14 días de inmersión en SFA.

En cuanto a su liberación iónica, las dos composiciones mostraron un mismo comportamiento: a medida que se aumentaba el tiempo de inmersión en SFA, la concentración de silicio disminuía, mientras que las concentraciones de calcio y fósforo aumentaban. Sin embargo, cabe destacar la mayor rapidez de liberación y precipitación iónica en el caso de las muestras con Mg.

Estos resultados indican que la modificación superficial de las muestras con Na es más lenta que la de las muestras con Mg, por lo que la pendiente de cambio es mayor en estas últimas. Por lo tanto, la presencia de Na en la composición de las biocerámicas retrasa el proceso de precipitado de la capa de CaP sobre su superficie y, más importante, cambia la microestructura y nanoestructura del precipitado,

modificando las propiedades superficiales de las matrices y alterando la interacción del material con los sistemas biológicos.

Como ya se ha indicado anteriormente, una característica común de todas las biocerámicas porosas es la baja resistencia mecánica, consecuencia de una elevada porosidad. Las cerámicas obtenidas en la presente Tesis Doctoral mediante el proceso sol-gel no están exentas de esta limitación, acentuándose el debilitamiento estructural al someter las cerámicas a los ensayos con cultivos celulares, razón por la que no se pudieron llevar a cabo ensayos *in vitro* utilizando ah-MSCs.

Un objetivo a desarrollar en el futuro con esta metodología es dotar de mayor resistencia a los materiales, modificando aspectos como la composición del sol-gel y grado de porosidad, pudiendo de esta manera realizar los correspondientes ensayos *in vitro* e *in vivo*.

En el transcurso de la presente Tesis Doctoral, además de obtener biocerámicas a través del proceso sol-gel, también se han obtenido biocerámicas mediante la técnica de reacción en estado sólido y el método de replicación polimérica utilizando una barbotina. A continuación, se expondrán los resultados más relevantes obtenidos tras utilizar cada una de estas técnicas.

En la publicación "***Revising the Subsystem Nurse's A - Phase-Silicocarnotite within the System $Ca_3(PO_4)_2$ - Ca_2SiO_4***" se revisó el subsistema fase A – Silicocarnotita (fase A – fase S) dentro del sistema de fases C_2S – TCP propuesto por Fix y cols. (41), para confirmar las temperaturas y concentraciones de reactivos necesarias para obtener cada una de las fases y microestructuras indicadas en el diagrama.

A partir del análisis térmico diferencial de las fases A y S, ambas de alta cristalinidad, obtenidas mediante reacción en estado sólido, se consiguieron las temperaturas de transformación de ambas fases a la fase R_{ss}. En base a estas temperaturas, se elaboraron 16 materiales con diferentes proporciones de las fases A y S, sometidos a temperaturas y tiempos de sinterización diferentes. Cada uno de ellos fue analizado mediante DRX para conocer las fases obtenidas en cada caso.

En la tabla 1 se muestran las composiciones más significativas, mostrándose el porcentaje en peso de cada uno de los reactivos, la temperatura de sinterización, las fases de los productors finales y su microesctructura observada mediante SEM.

Nº composición	% en peso de A	% en peso de S	Temperatura sinterización (ºC)	Fases observadas (DRX)	Microestructura (SEM)
6	55,00	45,00	1250	$A_{ss} + S_{ss}$	A hipoeutectoide y A+S eutectoide
11	28,39	71,61	1366	$A_{ss} + S_{ss}$	A+S eutectoide

Tabla 1. Resumen de los materiales con composición 6 y 11, mostrando el porcentaje en peso de los reactivos cerámicos, la temperatura de sinterización, las fases obtenidas por DRX y la microestructura observada mediante SEM.

La composición número 6 (55,00% en peso de fase A y 45,00% en peso de fase S) se corresponde con la composición del punto eutéctico establecido por Fix y cols., cuya temperatura crítica se encuentra a 1250ºC. Si la composición anteriormente mencionada es realmente la eutéctica, se debería obtener fase R únicamente a temperaturas superiores a 1250ºC. Sin embargo, en las muestras obtenidas a 1275ºC se observaron las fases A y R, indicando que realmente esta composición es una composición hipoeutectoide. Este resultado se confirma con los datos obtenidos mediante SEM, donde se observaron granos de fase A hipoeutectoide, en cuyos límites de grano se contempló fase eutectoide compuesta por las fases A y S, como consecuencia de la descomposición de R.

La composición número 11 (28,39% en peso de fase A y 71,61% en peso de fase S) describe la composición del nuevo punto eutectoide propuesto en la presente publicación, siendo la temperatura crítica para este eutectoide 1366 ± 4ºC. Este extremo se verificó analizando las muestras sinterizadas a 1370ºC, temperatura superior a la del punto eutectoide, donde se aprecia la presencia de fase R solamente. Además, el nuevo punto propuesto muestra una morfología lamelar a lo largo de toda la superficie del material, formada por las fases A y S.

Una vez revisado el sub-sistema fase A – Silicocarnotita y caracterizada la cerámica eutectoide obtenida (composición 11), se decidió estudiar su biocompatibilidad y citotoxicidad, en términos de adhesión y proliferación celular, además de su capacidad osteoinductora utilizando cultivos de ah-MSCs. Los resultados obtenidos tras realizar estos ensayos se publicaron en ***"Assessment of Effects of Si-Ca-P Biphasic Ceramic on the Osteogenic Differentiation of a Population of Multipotent Adult Human Stem Cells"***.

Con objeto de realizar el estudio de biocompatibilidad, se sembraron ah-MSCs sobre la superficie de cerámicas con microestructura eutectoide, con composición 28,39% en peso de fase A y 71,61% en peso de fase S, observando la evolución de las células mediante SEM después de 1, 7, 14, 21 y 28 días desde la siembra celular, utilizando un medio de crecimiento básico. Además, se realizó el estudio de la evolución celular tras 21 y 28 días incluyendo suplementos osteogénicos en el medio de crecimiento básico, consistentes en dexametasona, β-glicerofosfato y ácido ascórbico.

Durante los primeros 14 días, se observó un aumento de la cantidad de ah-MSCs, que mostraron numerosas interacciones célula-célula gracias a la emisión de prolongaciones citoplasmáticas (filopodios). A partir de los 21 días, las células formaron una monocapa que cubrió parcialmente la superficie de la biocerámica, generando una matriz extracelular densa, formada por una red fibrilar que ocupaba los espacios intercelulares. Finalmente, a los 28 días las células formaron una monocapa continua, imposibilitando reconocer células de forma individualizada.

Mediante un ensayo MTT, que consiste en la reducción de una sal de tetrazolio amarillo en formazán púrpura, permitiendo cuantificar la actividad respiratoria de células vivas, se analizó la posible citotoxicidad del biomaterial en términos de actividad metabólica y proliferación celular. A partir de los 14 días, la actividad metabólica de las células adheridas a la superficie de la biocerámica fue mayor que las que crecieron sobre el plástico (que actúa como control) en todos los periodos de estudio, siguiendo ambos una progresión lineal, destacando un mayor aumento en aquellos periodos de estudio correspondientes con la suplementación osteogénica.

Una vez confirmada la biocompatibilidad y baja citotoxicidad del material, se cuantificó la liberación iónica de las biocerámicas como consecuencia de su disolución, asociando el efecto de esta liberación sobre la evolución del crecimiento y diferenciación celular. El comportamiento más destacable lo presentó el calcio, cuya concentración en el medio aumentó significativamente durante las primeras 12 horas, alcanzando su máxima concentración tras 12 días de incubación de las biocerámicas y, posteriormente, disminuyendo hasta valores de 155 ppm. A pesar de esta disminución, la concentración final continúa siendo un 63,54% superior con respecto a la concentración del medio de crecimiento celular.

Esta evolución del calcio podría explicar la dificultad de adaptación que presentaron las células a bajos tiempos de estudio, reflejado en su lenta proliferación inicial y su forma más o menos esférica, llegando al caso extremo de que concentraciones elevadas de Ca pueden resultar citotóxicas (> 300 ppm) (61).

El siguiente objetivo de esta publicación fue analizar la capacidad osteoinductora de la biocerámica eutéctica sobre las ah-MSCs. Para ello se cuantificó la actividad Fosfatasa Alcalina (FA), se analizó cualitativa y cuantitativamente la formación de nódulos de mineralización mediante tinción con disolución de Alizarín Red (Alizarín Red solution, AR-s) y se determinó la presencia o ausencia de determinados marcadores de superficie específicos (CDs) de ah-MSCs.

Los resultados de la cuantificación de la actividad FA mostraron que tras 28 días en medio osteogénico, la actividad se incrementaba notablemente en las células sembradas sobre las biocerámicas respecto a las células control.

Por otra parte, la tinción con AR-s fue más intensa para las células sembradas bajo la influencia de las biocerámicas tanto en medio de crecimiento como en medio osteogénico. Cuando se cuantificó la cantidad de AR-s presente en las diferentes muestras, se observó un incremento muy notable en las células sembradas bajo la influencia de las biocerámicas a 28 días con medio osteogénico, con respecto a las células sembradas sobre plástico (células control). La formación de los depósitos de calcio o biomineralización es el proceso por el cual se depositan cristales de hidroxiapatita mineral en la matriz extracelular de células de estirpe osteoblástica. Este hidroxiapatito se forma por la incorporación de iones calcio y fosfato inorgánico, que puede ser proporcionado tanto por el β-glicerofosfato contenido en el medio osteogénico (62) como por la liberación iónica al medio de cultivo por la biocerámica. Además, la biomineralización consta de dos fases: una fase inicial que es dependiente de la actividad FA y una fase de progresión que es independiente de la actividad FA (63). Por este motivo, las células que se encuentran en medio osteogénico, y bajo la influencia de la liberación iónica de las cerámicas eutécticas, tienen a su disposición una mayor cantidad de iones calcio y grupos fosfato, además de una elevada actividad FA, lo que facilita que las células sean capaces de iniciar el proceso de mineralización.

Finalmente, tras observar la influencia de la liberación iónica de la biocerámica eutéctica sobre la diferenciación osteoblástica de las ah-MSCs, se sinterizó una nueva biocerámica porosa formada por las fases A y S, mediante el

método de replicación polimérica utilizando una barbotina. Estas nuevas matrices porosas se utilizaron para llevar a cabo ensayos de comportamiento *in vivo* implantándolas en tibias de conejos macho de Nueva Zelanda, cuyos resultados fueron publicados bajo el título de ***"Novel Resorbable and Osteoconductive Calcium Silicophosphate Scaffold Induced Bone Formation"***.

En primer lugar se llevó a cabo la caracterización de la biocerámica porosa de composición 28,39% en peso de fase A y 71,61% en peso de fase S, establecida anteriormente como eutéctica, pero modificando la temperatura y tiempo de sinterización, por lo que la microestructura era diferente. Mediante SEM se observó una porosidad interconectada formada por meso y macroporos, con diámetros comprendidos entre 1 μm – 10 μm y 200 μm – 1 mm, respectivamente, con puentes de aproximadamente 50 μm de grosor. Estas características la hacen idónea para utilizarla como potencial sustituto del injerto óseo (23, 64), ya que son capaces de posibilitar el crecimiento de tejido óseo nuevo en su interior (colonización) y permitir la invasión vascular por medio de capilares sanguíneos. Por otra parte, el análisis cuantitativo por EDX mostró los porcentajes en peso de SiO_2, CaO y P_2O_5 (15,10%, 58,20% y 26,60%, respectivamente).

Tras caracterizar la biocerámica, varias piezas se implantaron en tibias de conejos adultos machos de la raza Nueva Zelanda siguiendo el protocolo aprobado por la Comisión de Ética en la Investigación Experimental de la Universidad Miguel Hernández. Todos los animales sobrevivieron al procedimiento quirúrgico, no presentando evidencia de inflamación o infección local a lo largo de todo el estudio. Transcurridos 3 y 6 meses desde la intervención, los conejos fueron sacrificados para extraerles las tibias y estudiar la respuesta biológica del hueso a las biocerámicas mediante rayos X, histomorfometría y SEM.

Tras 3 meses desde la cirugía, se obtuvieron imágenes de rayos X en las que se podía observar un perfil rectangular de gran radiopacidad con apariencia moteada irregular y contorno liso, además de observar una correcta integración y resorción parcial del material. Después de 6 meses, la morfología del biomaterial mantenía su forma rectangular con contornos irregulares, observándose una zona más densa como consecuencia de la presencia de hueso trabecular neoformado. Cabe destacar que no se observaron alteraciones locales próximas al implante, tales como pérdida de tejido óseo trabecular adyacente o formación de hueso ectópico.

Posteriormente, se llevó a cabo una evaluación histológica y un análisis histomorfométrico de secciones transversales de 4 μm de grosor, de las tibias con

los implantes. A los 3 meses desde la colocación del implante, se pudo observar cómo el proceso de colonización de la matriz tridimensional comenzaba en la periferia, para continuar hacia el interior a través de los poros del implante, observándose tejido óseo neoformado con características de hueso trabecular. Es importante destacar la ausencia de células inflamatorias (macrófagos y linfocitos) y tejido conectivo fibroso en las proximidades del material implantado, que se interpretaría como un signo de intolerancia hacia el implante. Además, se observó la presencia de finas capas de tejido osteoide y abundantes osteoblastos en la periferia del material, así como elementos de la médula ósea y capilares sanguíneos.

En la cerámica implantada durante 6 meses se observó, en primer lugar, que el material estaba completamente envuelto por el nuevo tejido óseo formado, penetrando sobre áreas grandes y, en ocasiones, reemplazando al material implantado; y en segundo lugar, que los poros del material aumentaron su tamaño como consecuencia de su degradación, formando una superficie más irregular y favoreciendo el crecimiento del tejido óseo desde la superficie hacia el interior del mismo (crecimiento centrípeto). La zona central del implante presentaba pequeños y aislados depósitos de nuevo tejido óseo con estructura cortical, en los que eran visibles lagunas osteocíticas. El tejido óseo neoformado mostraba varios niveles de maduración, observándose tejido óseo inmaduro no mineralizado (osteoide), rodeado por tejido óseo maduro con osteonas de estructura regular. Las superficies óseas estaban ocupadas por una gran cantidad de osteoblastos dispuestos en fila y, además, la presencia de líneas de cemento y lagunas osteocíticas ocupadas por osteocitos, demostraron una aposición de hueso maduro de características normales.

Tras analizar las imágenes histológicas, se establecieron los valores BIC (Bone-to-Implant Contact, hueso en contacto con un implante) para el material mediante análisis histomorfométrico, medidos como el porcentaje de la circunferencia y longitud del cilindro que se encuentra en contacto con el tejido óseo neoformado. A los 6 meses de la intervención quirúrgica, se alcanzó un valor BIC de 67,30% ± 1,41, observando un contacto directo implante - hueso neoformado. Además, se determinó: la cantidad de tejido óseo en el interior del biomaterial, observándose hasta un 62,18% ± 2,28; el cierre del defecto, alcanzando hasta un 80,08% ± 1,96; y el porcentaje de biomaterial residual, que disminuyó hasta un 24,95% ± 0,99. En las muestras control también se observó un aumento en el

hueso neoformado sobre el defecto cortical, aunque fue menor que en el caso del implante en ambos periodos de estudio.

Esta invasión del biomaterial por nuevo tejido óseo y su progresiva degradación como consecuencia de su ratio de resorción y de la actividad fagocítica de los macrófagos, demuestran el gran potencial de estas matrices porosas para usarse como sustitutos óseos en el campo de la ingeniería de tejidos (65, 66).

10. CONCLUSIONES

10. CONCLUSIONES

1. Se ha desarrollado una nueva metodología para obtener materiales cerámicos porosos tridimensionales estratificados.

2. El estudio mineralógico mostró dos biocerámicas compuestas por una fase amorfa mayoritaria de silicato cálcico principalmente, con pequeñas trazas de silicio, en el caso de las cerámicas sinterizadas a 950ºC, y pequeñas trazas de silicio y de fosfato tricálcico, en el caso de las sinterizadas a 1400ºC.

3. La resistencia diametral de las biocerámicas desarrolladas depende directamente del número de capas de la cerámica y de la temperatura de sinterización.

4. La metodología establecida permite crear nuevos materiales de acuerdo con las necesidades de cada situación, pudiendo obtener materiales con un núcleo muy resistente y una elevada bioactividad en su parte exterior, o viceversa, dependiendo del lugar en el que se vaya a colocar el implante óseo.

5. Se han desarrollado matrices tridimensionales con porosidad interconectada con composición $MgO – K_2O – CaO – SiO_2$, mostrando una elevada bioactividad al presentar precipitados similares al hidroxiapatito a las pocas horas de inmersión en SFA, formando una microestructura compuesta por partículas con morfología de nanocilindros tras 3 días de inmersión.

6. Se han desarrollado matrices tridimensionales con porosidad interconectada con composición $Na_2O – K_2O – CaO – SiO_2$, mostrando una buena bioactividad, presentando los primeros precipitados apareciesen a los 3 días de inmersión en SFA. Las micropartículas también estaban formadas por nanocilindros.

7. El subsistema fase A – Silicocarnotita, dentro del diagrama de fases C_2S-TCP presenta un punto invariante con composición 59,50% en peso de TCP y 40,50% en peso de C_2S (ó 28,39% en peso de fase A y 71,61% en peso de Silicocarnotita), a una temperatura de 1366 ± 4ºC.

8. Se ha demostrado, a través de la proliferación, crecimiento y diferenciación osteoblástica de ah-MSCs expuestas a las biocerámicas eutécticas, que el material bifásico desarrollado en el presente trabajo no es citotóxico, permitiendo una adecuada adhesión y proliferación celular sobre la superficie de la biocerámica, además de iniciar la diferenciación osteogénica tanto en medio de crecimiento como en medio osteogénico. Por lo tanto, estas biocerámicas constituyen una plataforma prometedora para la regeneración del tejido óseo.

9. La cerámica porosa de silicofosfato cálcico, obtenida utilizando el método de replicación polimérica con barbotina, presentó una elevada biocompatibilidad al no causar ningún tipo de reacción local o respuesta inflamatoria, además de no provocar el desarrollo de una cápsula fibrosa rodeando el material cerámico tras su implantación intramedular en la tibia de conejos de raza Nueva Zelanda.

10. Se ha demostrado que la cerámica porosa proporciona un microambiente óptimo para la diferenciación osteogénica de células precursoras indiferenciadas, contenidas en la médula ósea hematopoyética. Así mismo, su estructura porosa interconectada facilita la colonización por nuevo tejido óseo, médula ósea y capilares sanguíneos, que promueven la regeneración del tejido, y proporcionan todos los nutrientes necesarios.

11. Se ha confirmado que la cerámica porosa de silicofosfato cálcico obtenida en el presente trabajo, favorece y apoya la integración del hueso, gracias a su osteoconductividad y continua degradación, como consecuencia de su reabsorción y de la actividad fagocítica de los macrófagos.

12. La cerámica porosa de silicofosfato cálcico desarrollada podría ser considerada como un potente sustituto óseo para aplicaciones clínicas, como relleno óseo o utilizándola como matriz tridimensional en la ingeniería del tejido óseo.

11. BIBLIOGRAFÍA

11. BIBLIOGRAFÍA

1. Roseti L, Parisi V, Petretta M, Cavallo C, Desando G, Bartolotti I, et al. Scaffolds for Bone Tissue Engineering: State of the art and new perspectives. Materials Science and Engineering: C. 2017;78:1246-62.
2. Agarwal R, García AJ. Biomaterial strategies for engineering implants for enhanced osseointegration and bone repair. Advanced drug delivery reviews. 2015;94:53-62.
3. Wang W, Yeung KW. Bone grafts and biomaterials substitutes for bone defect repair: A review. Bioactive Materials. 2017;2(4);224-247.
4. Bilezikian JP, Raisz LG, Martin TJ. Principles of bone biology: Academic Press; 2008.
5. Florencio-Silva R, Sasso GRdS, Sasso-Cerri E, Simões MJ, Cerri PS. Biology of bone tissue: structure, function, and factors that influence bone cells. BioMed research international. 2015;17.
6. Kini U, Nandeesh B. Physiology of bone formation, remodeling, and metabolism. Radionuclide and hybrid bone imaging: Springer; 2012. p. 29-57.
7. Marks SC, Odgren PR. Structure and development of the skeleton. Principles of Bone Biology (Second Edition): Elsevier; 2002. p. 3-15.
8. Perez Castañeda J. Osteopetrosis: La Enfermedad de los Huesos de Mármol http://diariosradiologia.blogspot.com.es/2014/12/el-situs-inversus.html2014.
9. Tejidos animales - Tejido óseo http://mmegias.webs.uvigo.es/guiada_a_oseo.php: Atlas de histología vegetal y animal 2018. Universidad de Vigo
10. Bartl R, Frisch B. Biology of bone. Osteoporosis: Springer; 2009. p. 7-28.
11. Rahman MS, Akhtar N, Jamil HM, Banik RS, Asaduzzaman SM. TGF-β/BMP signaling and other molecular events: regulation of osteoblastogenesis and bone formation. Bone research. 2015;3:15005.
12. Warden SJ, Davis IS, Fredericson M. Management and prevention of bone stress injuries in long-distance runners. journal of orthopaedic & sports physical therapy. 2014;44(10):749-65.
13. Gartner LP, Hiatt JL, Strum JM. Cell Biology and Histology (Board Reveiw Series)1998.
14. Mijangos C, Moya JS. Nuevos materiales en la sociedad del siglo XXI: CSIC; 2007.
15. Vallet Regí M. Biomateriales, piezas de repuesto para reparar el cuerpo humano: CSIC; 2013.

16. Carlos A, Ramírez B. ¿II Guerra Mundial y los implantes? http://biomateriales.org/blog/2014/04/ii-guerra-mundial-y-los-implantes/: Centro de Investigación en Biomateriales, Universidad de Guadalajara; 2014.
17. Chevalier J, Gremillard L. Ceramics for medical applications: A picture for the next 20 years. J Eur Ceram Soc. 2009;29((7)):1245-55.
18. Jones JR. Reprint of: Review of bioactive glass: From Hench to hybrids. Acta biomaterialia. 2015;23:S53-S82.
19. Turnbull G, Clarke J, Picard F, Riches P, Jia L, Han F, et al. 3D bioactive composite scaffolds for bone tissue engineering. Bioactive Materials. 2017;278-314
20. Alonso-Goulart V, Ferreira LB, Duarte CA, de Lima IL, Ferreira ER, de Oliveira BC, et al. Mesenchymal stem cells from human adipose tissue and bone repair: a literature review. Biotechnology Research and Innovation. 2017.
21. Griffin KS, Davis KM, McKinley TO, Anglen JO, Chu T-MG, Boerckel JD, et al. Evolution of bone grafting: bone grafts and tissue engineering strategies for vascularized bone regeneration. Clinical Reviews in Bone and Mineral Metabolism. 2015;13(4):232-44.
22. PromoCell. Some Human Mesenchymal Stem Cells are More Equal than Others – Origins and Differences https://www.promocell.com/blog/mesenchymal-stem-cell-research-some-mscs-are-more-equal-than-others/2018.
23. Hench LL, Polak JM. Third-generation biomedical materials. Science. 2002;295(5557):1014-7.
24. Navarro M, Michiardi A, Castano O, Planell J. Biomaterials in orthopaedics. Journal of the Royal Society Interface. 2008;5(27):1137-58.
25. Tanner K. Bioactive ceramic-reinforced composites for bone augmentation. Journal of The Royal Society Interface. 2010;7: S541-S57.
26. Tonino AJ, van der Wal BC, Heyligers IC, Grimm B. Bone remodeling and hydroxyapatite resorption in coated primary hip prostheses. Clinical orthopaedics and related research. 2009;467(2):478-84.
27. Sastre R, de Aza S, San Román J. Biomateriales: Faenza editrice iberica; 2004.
28. De Aza P, Luklinska Z, Anseau M, Hector M, Guitian F, De Aza S. Reactivity of a wollastonite–tricalcium phosphate Bioeutectic® ceramic in human parotid saliva. Biomaterials. 2000;21(17):1735-41.
29. Magallanes-Perdomo M, Pena P, De Aza P, Carrodeguas R, Rodríguez M, Turrillas X, et al. Devitrification studies of wollastonite–tricalcium phosphate eutectic glass. Acta biomaterialia. 2009;5(8):3057-66.
30. Azeena S, Subhapradha N, Selvamurugan N, Narayan S, Srinivasan N, Murugesan R, et al. Antibacterial activity of agricultural waste derived wollastonite doped with copper for bone tissue engineering. Materials Science and Engineering: C. 2017;71:1156-65.

31. Gandolfi MG, Shah SN, Feng R, Prati C, Akintoye SO. Biomimetic calcium-silicate cements support differentiation of human orofacial mesenchymal stem cells. Journal of endodontics. 2011;37(8):1102-8.
32. Arcos D, Vallet-Regí M. Sol–gel silica-based biomaterials and bone tissue regeneration. Acta Biomaterialia. 2010;6(8):2874-88.
33. Kim E-J, Bu S-Y, Sung M-K, Choi M-K. Effects of silicon on osteoblast activity and bone mineralization of MC3T3-E1 cells. Biological trace element research. 2013;152(1):105-12.
34. Brauer DS. Bioactive glasses—structure and properties. Angewandte Chemie International Edition. 2015;54(14):4160-81.
35. Hench LL. Bioceramics: from concept to clinic. Journal of the american ceramic society. 1991;74(7):1487-510.
36. Kokubo T. Apatite formation on surfaces of ceramics, metals and polymers in body environment. Acta Materialia. 1998;46(7):2519-27.
37. Ros-Tárraga P, De Aza PN, Murciano A. Caracterización de matrices porosas del sistema SiO_2-CaO-P_2O_5 para medicina regenerativa, UMH, 2015.
38. Hulbert S, Hench L, Forbers D, Bowman L. History of bioceramics. Ceramics international. 1982;8(4):131-40.
39. Mellor J. Some chemical and physical changes in the firing of pottery. J Soc Chem Ind. 1907;26(8):375-7.
40. Nurse R, Welch J, Gutt W. 220. High-temperature phase equilibria in the system dicalcium silicate–tricalcium phosphate. Journal of the Chemical Society (Resumed). 1959:1077-83.
41. Fix W, Heymann H, Heinke R. Subsolidus Relations in the System 2CaO· SiO2-3CaO· P2O5. Journal of the American Ceramic Society. 1969;52(6):346-7.
42. Manzano M, Vallet-Regí M. Revisiting bioceramics: bone regenerative and local drug delivery systems. Progress in Solid State Chemistry. 2012;40(3):17-30.
43. Smart LE, Moore EA. Solid state chemistry: an introduction: CRC press; 2012.
44. Labate GFDU, Catapano G, Vitale-Brovarone C, Baino F. Quantifying the micro-architectural similarity of bioceramic scaffolds to bone. Ceramics International. 2017;43(12):9443-50.
45. Park Y-S, Kim K-N, Kim K-M, Choi S-H, Kim C-K, Legeros RZ, et al. Feasibility of three-dimensional macroporous scaffold using calcium phosphate glass and polyurethane sponge. Journal of materials science. 2006;41(13):4357-64.
46. Boccardi E, Philippart A, Melli V, Altomare L, De Nardo L, Novajra G, et al. Bioactivity and mechanical stability of 45s5 bioactive glass scaffolds based on natural marine sponges. Annals of biomedical engineering. 2016;44(6):1881-93.

47. Denry I, Kuhn LT. Design and characterization of calcium phosphate ceramic scaffolds for bone tissue engineering. Dental Materials. 2016;32(1):43-53.
48. Hench LL, West JK. The sol-gel process. Chemical reviews. 1990;90(1):33-72.
49. Chen QZ, Thompson ID, Boccaccini AR. 45S5 Bioglass®-derived glass–ceramic scaffolds for bone tissue engineering. Biomaterials. 2006;27(11):2414-25.
50. Teixeira S, Rodriguez M, Pena P, De Aza A, De Aza S, Ferraz M, et al. Physical characterization of hydroxyapatite porous scaffolds for tissue engineering. Materials Science and Engineering: C. 2009;29(5):1510-4.
51. Padilla S, Roman J, Carenas A, Vallet-Regı M. The influence of the phosphorus content on the bioactivity of sol–gel glass ceramics. Biomaterials. 2005;26(5):475-83.
52. Jinlong N, Zhenxi Z, Dazong J. Investigation of phase evolution during the thermochemical synthesis of tricalcium phosphate. Journal of Materials synthesis and Processing. 2001;9(5):235-40.
53. Carrodeguas RG, De Aza AH, Turrillas X, Pena P, De Aza S. New Approach to the $\beta \rightarrow \alpha$ Polymorphic Transformation in Magnesium-Substituted Tricalcium Phosphate and its Practical Implications. Journal of the American Ceramic Society. 2008;91(4):1281-6.
54. Carrodeguas RG, De Aza S. α-Tricalcium phosphate: Synthesis, properties and biomedical applications. Acta biomaterialia. 2011;7(10):3536-46.
55. Sahai N, Anseau M. Cyclic silicate active site and stereochemical match for apatite nucleation on pseudowollastonite bioceramic–bone interfaces. Biomaterials. 2005;26(29):5763-70.
56. Marians CS, Hobbs LW. Network properties of crystalline polymorphs of silica. Journal of non-crystalline solids. 1990;124(2-3):242-53.
57. Catauro M, Dell'Era A, Ciprioti SV. Synthesis, structural, spectroscopic and thermoanalytical study of sol–gel derived SiO2–CaO–P2O5 gel and ceramic materials. Thermochimica Acta. 2016;625:20-7.
58. Mouriño V, Boccaccini AR. Bone tissue engineering therapeutics: controlled drug delivery in three-dimensional scaffolds. Journal of the Royal Society Interface. 2009:rsif20090379.
59. Polak DJ. Regenerative medicine. Opportunities and challenges: a brief overview. Journal of the Royal Society Interface. 2010;7(Suppl 6):S777-S81.
60. Correia SI, Pereira H, Silva-Correia J, Van Dijk C, Espregueira-Mendes J, Oliveira JM, et al. Current concepts: tissue engineering and regenerative medicine applications in the ankle joint. Journal of The Royal Society Interface. 2014;11(92):20130784.

61. Valerio P, Pereira MM, Goes AM, Leite MF. The effect of ionic products from bioactive glass dissolution on osteoblast proliferation and collagen production. Biomaterials. 2004;25(15):2941-8.
62. Orimo H. The mechanism of mineralization and the role of alkaline phosphatase in health and disease. Journal of Nippon Medical School. 2010;77(1):4-12.
63. Bellows C, Heersche J, Aubin J. Inorganic phosphate added exogenously or released from β-glycerophosphate initiates mineralization of osteoid nodules in vitro. Bone and mineral. 1992;17(1):15-29.
64. Jones JR. New trends in bioactive scaffolds: the importance of nanostructure. Journal of the European Ceramic Society. 2009;29(7):1275-81.
65. Rabadan-Ros R, Velásquez PA, Meseguer-Olmo L, De Aza PN. Morphological and structural study of a novel porous Nurse's A ceramic with osteoconductive properties for tissue engineering. Materials. 2016;9(6):474.
66. De Aza PN, Mate-Sanchez de Val JE, Baudin C, Perez Albacete-Martínez C, Armijo Salto A, Calvo-Guirado JL. Bone neoformation of a novel porous resorbable Si-Ca-P-based ceramic with osteoconductive properties: physical and mechanical characterization, histological and histomorphometric study. Clinical Oral Implants Research. 2016;27(11):1368-75.

12. ANEXOS

12. ANEXOS

12.1. COMUNICACIONES A CONGRESOS

- II Jornadas Científicas del IMIB-Arrixaca, 27 de Noviembre de 2017, Murcia, España.
  "Efecto de los elementos iónicos liberados por una nueva cerámica bifásica formada por wollastonita y fosfato tricálcico sobre una población de células madre mesenquimales adultas"
  Patricia Ros-Tárraga, Patricia Mazón, Rubén Rabadán-Ros, Ángel Murciano, Piedad N. de Aza, Luis Meseguer-Olmo.
  Tipo de comunicación: Póster

- Real Academia de Medicina y Cirugía de la Región de Murcia, 5 de Octubre de 2017, Murcia, España.
  "Desarrollo de materiales cerámicos de silicofosfato cálcico, como alternativa al uso de injertos óseos en regeneración óseas"
  Patricia Ros-Tárraga
  Tipo de comunicación: Oral.

- 11th International Conference on Advanced Materials and Processing, 7-8 de Septiembre de 2017, Edinburgo, Escocia.
  "Microstructural, mineralogical and chemical characterization of a new 3D stratified Si-Ca-P porous scaffolds obtained by sol-gel and polymer replica method"
  Patricia Ros-Tárraga, Ángel Murciano, Patricia Mazón, Sergio A. Gehrke, Piedad N. de Aza.
  Tipo de comunicación: e-Póster

- 3rd International Conference and Expo on Ceramics and Composite Materials, 26-27 de Junio de 2017, Madrid, España.
  "Biphasic Si-Ca-P ceramic for regenerative medicine: Scaffolds processing and biocompatibility"

Piedad N. de Aza, Patricia Ros-Tárraga, Patricia Mazón, Miguel A. Rodríguez, Luis Meseguer-Olmo.
Tipo de comunicación: Oral

- III Jornadas de Investigación y Doctorado: Reconocimiento de los Doctores en el Mercado Laboral, 16 de Junio de 2017, Murcia, España.
  "Silicofosfatos cálcicos para ingeniería de tejidos"
  Patricia Ros-Tárraga.
  Tipo de comunicación: Oral

- 2nd Annual Conference and Expo on Biomaterials, 27-28 de Marzo de 2017, Madrid, España.
  "Biological properties of a new Si-Ca-P porous scaffold for tissue engineering"
  Patricia Ros-Tárraga, Miguel A. Rodríguez, Rubén Rabadán-Ros, Piedad N. de Aza, Luis Meseguer-Olmo.
  Tipo de comunicación: e-Póster

- 2nd Annual Conference and Expo on Biomaterials, 27-28 de Marzo de 2017, Madrid, España.
  "Nurse's A-phase material enhance adhesion, growth and differentiation of human bone marrow-derived stromal mesenchymal stem cells"
  Rubén Rabadán-Ros, Salvador Aznar-Cervantes, Patricia Mazón, Patricia Ros-Tárraga, Piedad N. de Aza, Luis Meseguer-Olmo.
  Tipo de comunicación: e-Póster

- II Jornadas de Investigación y Doctorado: Doctorado Industrial, 24 de Junio de 2016, Murcia, España.
  "Silicofosfatos cálcicos porosos para ingeniería de tejidos"
  Patricia Ros-Tárraga.
  Tipo de comunicación: Oral

- 32 Jornadas Nacionales de Enfermería en Cirugía Ortopédica y Traumatología, 13 de Mayo de 2016, Murcia, España.

"Medicina regenerativa en la especialidad de C. O. T."
Patricia Ros-Tárraga, Rubén Rabadán-Ros, Luis Meseguer-Olmo.
Tipo de comunicación: Oral

- XI Congreso Nacional INVESCOT, 5 de Febrero de 2016, Madrid, España.
  "Estudio *in vivo* del comportamiento de una nueva matriz tridimensional de silicofosfato cálcico"
  Patricia Ros-Tárraga, Rubén Rabadán-Ros, Miguel A. Rodríguez, Patricia Mazón, Piedad N. De Aza, Luis Meseguer-Olmo.

12.2. PATENTES

- Presentación de solicitud de Patente en Oficina Española de Patentes y Marcas, Ministerio de Industria, Energía y Turismo, "Procedimiento de obtención de un material para regeneración ósea y material así obtenido", 24 de Julio de 2017.